POLITECNICO DI MILANO

Dipartimento di Ingegneria Aerospaziale
Doctoral Programme in Rotary Wing Aircrafts

RETREATING BLADE DYNAMIC STALL

Doctoral Dissertation of:
Alex Zanotti

Supervisor:
Prof. Giuseppe Gibertini
Tutor:
Prof. Luigi Vigevano
The Chair of the Doctoral Programme:
Prof. Carlo Luigi Bottasso

Year 2012/XXIV cycle

Aknowledgements

The first person I want to thank is my Supervisor Prof. Giuseppe Gibertini, who gave me the possibility to get in these years a constant professional and human growth under his guide. His scientific knowledge, advices and thinking forward make me always find out the right way to follow in order to obtain improvements in my work and new interesting research topics to investigate.
Then, great thanks to Donato Grassi, both as wind tunnel technician and very good friend. His great technical competence has been precious in my work. Moreover, he has been always at my side during the experimental campaign sharing the success and disappointments coming from the complexity and ambition of the experimental rig. With the same motivation, I want to thank also Gabriele Campanardi, in particular for his technical advices in the development of the test rig project and PIV set up.
Thanks also to my colleagues and very good friends, Luca, for his support in the development of the post-processing software, Alessandro for the support in the finite element analysis, Carlo, Simone and Giovanni. They made the office a place where spending time is always amazing.
My personal thanks are for my family, Dad, Mom, Yasmine and the new entry Jari; they are always close to me with their love and advices. Then, thanks to my Grandfather, my guide in everyday life.
And now, I think the most important thanks to my sweet half Antonella, we will belong to each other forever.

Abstract

In the aim of research about dynamic stall control for helicopter performance improvement, a new experimental-numerical activity started at Politecnico di Milano about this topic. The present work focuses on the description of the experimental activity carried out on oscillating airfoils. A new experimental rig has been designed consisting in a blade section model supported by a motorized strut that can move it in pitch around its quarter chord. The design and performance of the experimental rig have been purposely conceived to reproduce the deep dynamic stall condition of a full-scale retreating rotor blade section at 75% radius at high forward flight speed; the main goal of the activity has been the study of the phenomenon in conditions typical of the flight envelope of a helicopter and the test of passive control systems to alleviate the detrimental effects on helicopter performance. Several measurement techniques as, for instance, fast unsteady pressure measurements and Particle Image Velocimetry (PIV), have been employed to completely characterise the time dependent flow field.

The work describes in particular the results of a comprehensive experimental campaign carried out on a NACA 23012 blade section. The analysis of the comprehensive data set obtained by means of the two different measurement techniques enabled to improve the description of the main features that characterise the dynamic stall phenomenon in the different regimes described in the literature.

Moreover, a preliminary assessment of the modeling capabilities for these peculiar flow conditions, comparing different numerical CFD models against the experimental results, is presented in the work. After the experimental activity on the clean blade section, the experimental rig has been employed to test passive control systems, as self-activated movable flaps and Gurney flaps, both on a NACA 23012 and on a NACA 23015 blade section model. The results of the experimental investigation on the passive control devices illustrate the capabilities and the limitations in terms of blade performance improvement of the tested trailing edge devices in the different phases of the pitching cycle and suggest the way to control such devices by means of an active system in order to get a better contribution for dynamic stall alleviation.

Introduction

The dynamic stall phenomenon represents one of the main topic of investigation in rotorcraft aerodynamics and is nowadays the subject of several research activities, both in numerical and in experimental field. In fact, the strong demand for faster helicopters has spurred the research on new rotor design equipped with active devices integrated on the blades to alleviate the detrimental effects of the phenomenon, responsible of important limitations on helicopter performance. In this aim, the use of more sophisticated experimental techniques, as well as efficient numerical models, are necessary to get a more detailed description of the non-linear physics that characterise the dynamic stall phenomenon.
The present work describes the first phase of the experimental activity developed during the three years of my PhD period about the study and control of dynamic stall on the retreating blade of helicopter rotors. The first focus of this project has been the design and validation of a new experimental apparatus for testing a full scale two-dimensional pitching blade section in dynamic stall conditions. The experimental apparatus has been extensively used to obtain a complete experimental data set to describe in detail the main features of the phenomenon in the different regimes described in literature [1]. The use of different measurement techniques as, for instance, high-response pressure measurementsand Particle Image Velocimetry (PIV) enabled to collect a comprehensive data base that allowed to completely characterise the time-dependent flow field, as well as to validate CFD tools. After the test activity on a clean blade section, the main goal of the experimental rig has become the test of new control systems integrated on a full-scale helicopter blade section and the analysis of their effectiveness to mitigate the adverse effects on helicopter performance. In this aim, the activity of the present work focused the attention on the study of passive control devices. In particular, an experimental campaign has been carried out to evaluate the effects of self-activating trailing edge flaps and Gurney flap integrated on two different blade section models.
A brief overview of chpters contents follows.
Chapter 1 describes the main features of dynamic stall with a detailed insight for the rotorcraft environment application. In particular, the detrimental effects on rotor performance connected to the non-linear physics of the phenomenon are presented, together with the description of the conditions that leads to the occurrence of an aeroelastic instability that involves

the torsional degree of freedom of the blades, called in literature (*Stall Flutter*).

Chapter 2 presents a detailed description of the new experimental apparatus designed for testing full-scale pitching blade sections. In particular, the blade section models project, as well as the dimensioning and control of the motorized strut for the model pitching motion, are illustrated in detail. Moreover, the chapter illustrates the set up of the measurement techniques employed in the experimental campaign on the pitching blade section, as unsteady pressure measurement and Particle Image Velocimetry.

Chapter 3 shows the main results of the extensive experimental campaign carried out on a NACA 23012 blade section model. The tests reproduce the typical conditions of a full-scale retreating rotor blade section at 75% radius in forward flight. The analysis of the measured airloads curves illustrates the effects of the parameters that characterise the sinusoidal pitching cycle, as the mean angle of attack, the amplitude and the reduced frequency. The airloads curves measured for some interesting test cases are compared with the experimental curves measured in a reference work in literature and with the results of numerical simulations carried out in our Department. The analysis of the velocity fields measured by means of PIV on the upper surface of the airfoil enabled to obtain a complete description of the blade stall process, highlighting the details of the main aerodynamic features that characterise the deep dynamic stall regime.

Furthermore, the experimental analysis of an higher order pitching motion effects overlaid to the sinusoidal motion of the blade section model is presented in this chapter. This activity produces interesting considerations about the effects of rotor blades elasticity on their primary pitching motion at 1/rev.

Chapter 4 presents an overview of the main results obtained in recent literature about active control for dynamic stall alleviation and describes the set up and the results of the experimental campaign carried out on a NACA 23012 and a NACA 23015 blade section models equipped with passive self-activated flaps integrated at the trailing edge and Gurney flap. This activity illustrates their capabilities and limitations in terms of blade performance improvement in the different phases of the pitching cycle.

Chapter 5 presents the conclusions of the present work and the future developments of the activity about dynamic stall investigation and control.

Contents

List of Figures

List of Tables

Chapter 1

Dynamic Stall

1.1 The dynamic stall phenomenon in rotorcraft environment

The investigation of the dynamic stall phenomenon on the rotor retreating blade represents one of the major research topic in helicopter aerodynamics and aeroelasticity fields, due to the strong demand for faster helicopters [1]. The dynamic stall occurs on the rotor retreating blades at high forward flight speed or during maneuvers at high load factors and produces the following different adverse effects on helicopter performance: high control system loads; vibration affecting the helicopter dynamic performance in terms of speed, lift, maneuver capability and handling qualities; aerodynamic performance limitations such as a loss of lift, thrust and control; occurrence of an aeroelastic instability called *stall flutter* [6], causing blade structural damage and excessive cabin vibration. The several negative effects on helicopter performance and flight dynamics illustrates the dynamic stall importance in a more complete aerodynamic and aeroelastic analysis of the rotor and justifies the very large number of publications both in the numerical and the experimental field about this subject.

The dynamic stall phenomenon occurs on the helicopter rotor in forward flight when, as can be observed in Fig. 1.1, the combination of the forward and the rotational speeds results in large variations of local velocities over the rotor blades. The main effect of the velocities composition is the increase of the local velocity on the advancing blade and a decrease on the retreating blade; consequently, these variations in speed would produce an imbalance

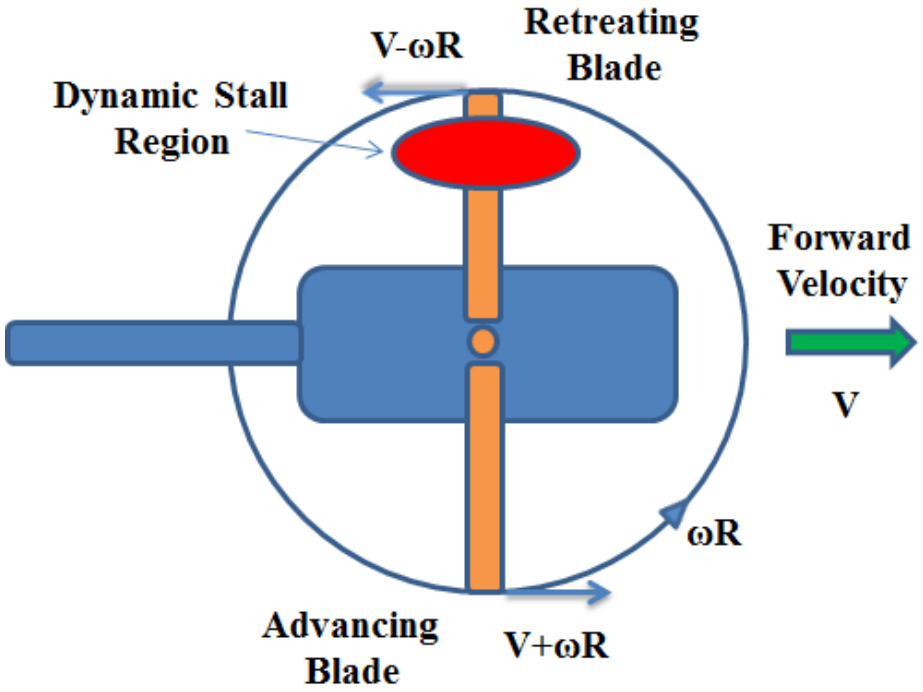

Figure 1.1: Layout of the flow on a helicopter rotor in forward flight.

or out-of-trim of the rotor. The rotor trimming is done by the application of cyclic pitch, in particular the rotor blade is pitched up when the local velocity is low and vice versa. With increasing forward speed the retreating blade experiences time-varying angle of attack resulting from blade flapping, cyclic pitch inputs and wake inflow. At high forward flight speed the angle of attack on the retreating side of the rotor could reach very high values greater than the characteristic static stall angle of attack of the blade airfoil (see Fig. 1.2). Then, the flow separation and stall occur on a rotor in a very dynamic and time-dependent manner as the retreating blade encounters a rapid variation of angle of attack due to the combination of a pitching and plunging motion.

Consequently, the physics of flow separation and the development of stall on the retreating blade presents different features from the stall mechanism exhibited by the same airfoil under static conditions. Moreover, the non-

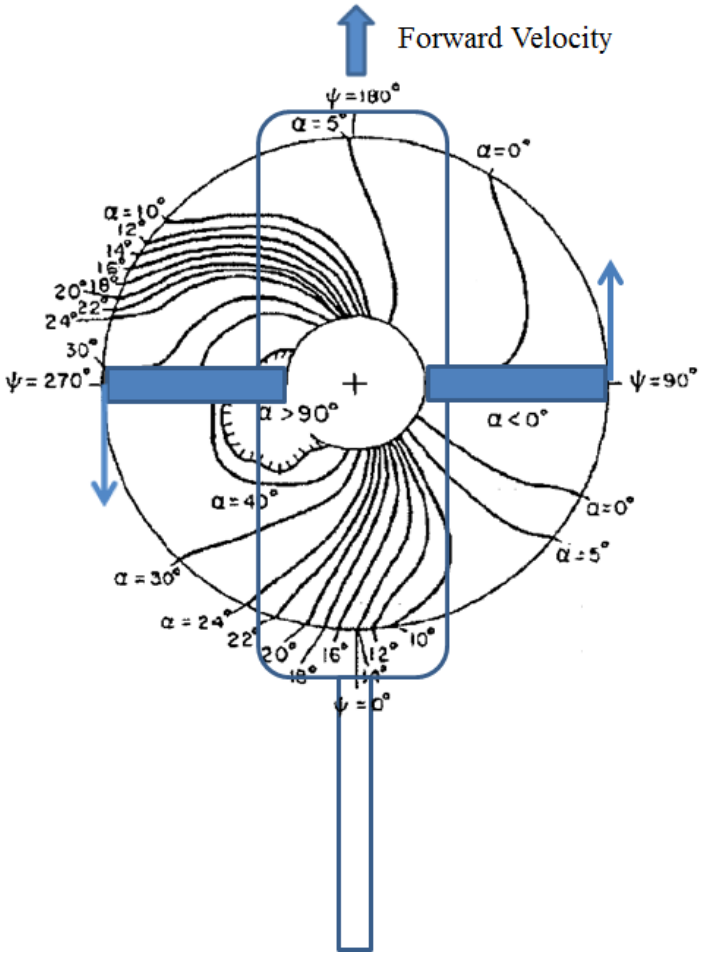

Figure 1.2: Contours of blade angle of attack for a S 61-F helicopter rotor at high forward flight speed; adapted from Carta [6].

linearities of the airloads associated with the dynamic stall process and the possibilities of lower aerodynamic damping could lead to a condition of aeroelastic instability described in literature as stall flutter [6].
The flow topology and the unsteady airloads acting on a blade airfoil during the dynamic stall process have been studied through several experimental activities on two-dimensional oscillating airfoils [2, 3]. In particular, the integration of pressure measurements along the midspan chord line of two dimensional blade section models have been carried out to evaluate the airloads hysteresis (lift and pitching moment) during a pitching cycle [32]

and made possible the dynamic performance characterisation of several helicopter sections and fixed-wing airfoils over a wide range of flow conditions [33]. Moreover, flow field measurements have been carried out in the past years using Particle Image Velocimetry technique to characterise the different stages of the dynamic stall process on pitching blade sections, for instance on a NACA 0012 airfoil as described in Raffel et al. [34]. Recently, the use of Time-Resolved PIV technique made possible to refine the investigation of the dynamic stall onset, in particular for conditions reproducing the helicopter rotor retreating blade [35].
One of the main goals of the present work, as will be described in the following chapters, is to achieve a detailed insight of the main aerodynamic issues that characterise the dynamic stall phenomenon through the use of the two measurement techniques: PIV flow surveys carried out on the upper surface of a pitching airfoil together with the measurements of the lift and pitching moment time histories.

1.2 Stall Flutter

The high non-linearities of the airloads acting on the retreating blade near the stall can introduce aeroelastic stability problems. In particular, the stall flutter occurs when negative aerodynamic damping changes a stable aeroelastic blade torsional mode into a divergent or high amplitude limit cycle oscillation [4]. The occurrence of this phenomenon can introduce blade structural damages and excessive vibrations in cabin. Therefore, the onset of dynamic stall limits the aeroelastic performance of a helicopter rotor.
The two-dimensional aerodynamic damping coefficient can be evaluated as follow [6]:

$$a_2 = -\frac{C_W}{\pi {\alpha_A}^2}, \tag{1.1}$$

where α_A is the airfoil oscillation amplitude and C_W is the coefficient of the work done by the aerodynamic moment over a pitching cycle, obtained integrating the product of the moment coefficient C_M in-phase components and the differential twist over the cycle:

$$C_W = \oint C_M(\alpha) d\alpha. \tag{1.2}$$

According to this definition, counterclockwise loops in the $C_M - \alpha$ curve contribute as positive values to the aerodynamic damping whereas clockwise loops as negative ones. If $a_2 < 0$, the airfoil extracts energy from the airstream and the oscillations will tend to increase in amplitude promoting an aeroelastic divergence or flutter situation. Consequently, when the net aerodynamic damping given by the area inside the $C_M - \alpha$ curve trace is negative, there is the condition for the stall flutter occurrence, as illustrated in Fig. 1.3 (airloads measured in the work by Singh et al. [42] for a pitching RAE 9645 airfoil).

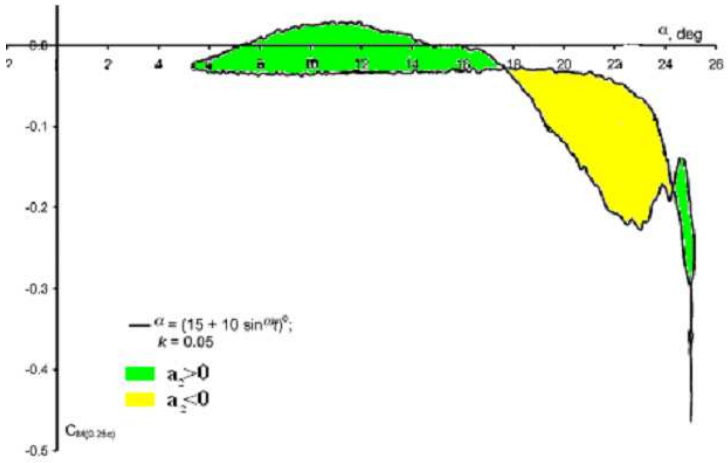

Figure 1.3: Aerodynamic damping for a pitching airfoil; adapted from Singh et al.[42].

The condition for a net negative aerodynamic damping occurs in particular when the airfoil oscillates in and out of stall, as the mean angle of attack of the pitching cycle is similar to the static stall angle of attack of the airfoil. This situation is illustrated in Fig. 1.4 that represents the $C_M - \alpha$ curves measured for a NACA 0012 airfoil oscillating in pitch with increasing mean angles of attack [11]. The $C_M - \alpha$ curves for the pitching cycles with a mean angle of attack 0° or 24° present counterclockwise loops and a positive aerodynamic damping; the $C_M - \alpha$ curve for the pitching cycle with a mean angle of attack 12°, similar to the airfoil static stall angle, presents a greater area of the clockwise loop respect to the counterclockwise loop area, with a consequent net negative aerodynamic damping.

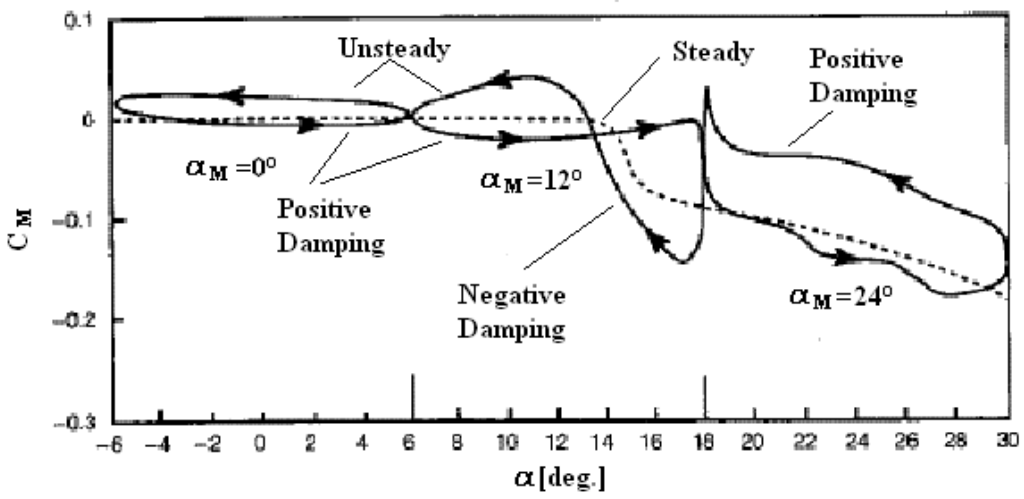

Figure 1.4: Behavior of the measured moment coefficient for a NACA 0012 pitching airfoil; adapted from Prouty [11].

The occurrence of stall flutter on a complete rotor has been evaluated in the work by Carta [6]. In particular, the torsional aerodynamic damping has been calculated for the case of a heavily loaded S-61 F rotor blade at high forward flight speed and presents negative values in the region from 225° to 10° of blade azimuth.
The large values of torsional stress and pitch link loads measured in the same azimuthal region, demonstrates that the calculation of the aerodynamic damping gives a good indication of the possibility of stall flutter occurrence.

1.3 Dynamic Stall regimes

The analysis of the wind tunnel experiments on two dimensional oscillating airfoils allowed to comprehend the effects of the variation of the parameters that characterise the pitching sinusoidal motion, as the mean angle of attack (α_M), the amplitude (α_0) and the reduced frequency (k).

The maximum angle of attack reached during the sinusoidal oscillation represents the primary parameter that determines the degree or extent of flow separation and consequently determines the different features of the two

dynamic stall regimes described in literature as *Light Dynamic Stall* and *Deep Dynamic Stall* (see Fig. 1.5 [1]).

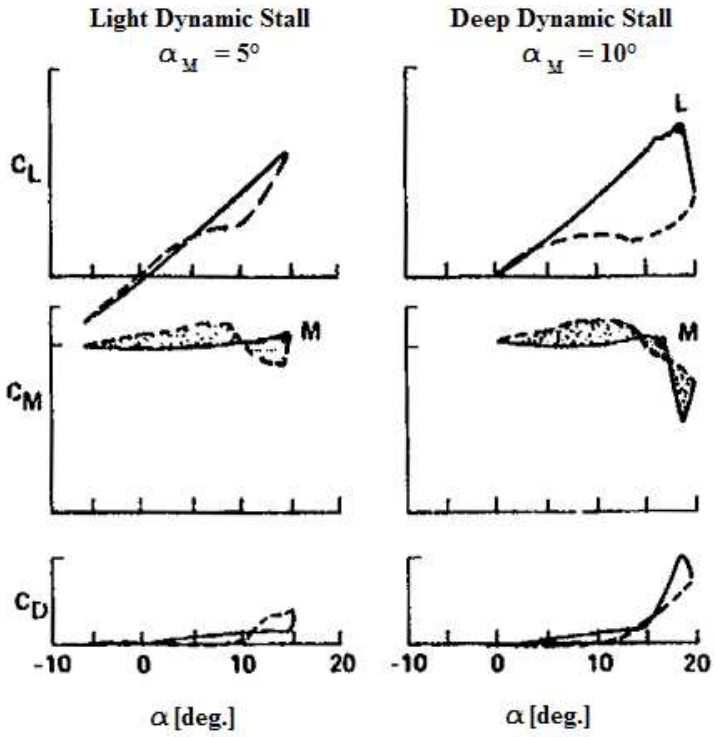

Figure 1.5: Dynamic Stall regimes on a NACA 0012 pitching airfoil $\alpha(t) = \alpha_M + 10° sin(\omega t)$, $k = 0.1$; solid lines increasing α, dashed lines decreasing α; adapted from McCroskey [1].

The *Light Dynamic Stall* regime occurs when the maximum angle of attack reached during the pitching cycle exceeds a little the static stall angle of attack of the airfoil. This regime is characterised by a delay in the onset of the lift stall respect to the static case and by minor flow separation from the airfoil. The airloads show small deviations from the attached flow behavior and small hysteresis. The viscous zone extent for these motion conditions is in the order of the airfoil thickness but the airloads behaviors are especially sensitive to parameters as the airfoil geometry, the reduced frequency and the Mach number.

The *Deep Dynamic Stall* regime occurs when the mean angle of attack is similar to the static stall angle of attack of the airfoil and the oscillation amplitude is conspicuous ($> 5°$). This regime is characterised by the vortex-shedding phenomenon and large deviations of the airloads respect to the attached flow behavior; consequently, the airloads curves present a great amount of hysteresis. The viscous zone extent for these motion conditions is in the order of the airfoil chord. Moreover, the regime is characterised by rapid airloads overshoots after the stall but the airloads behaviors are less sensitive to parameters as the airfoil geometry, the reduced frequency and the Mach number.

1.4 Dynamic Stall on a rotor

The dynamic stall phenomenon occurs over several radial and azimuthal regions of the retreating side of a helicopter rotor. A few experimental activities on in-flight rotor allowed to understand the occurrence of dynamic stall on helicopter blades.
The works by Isaacs & Harrison [12] and Bousman [13] identified for a typical forward flight condition the locations on the rotor disk of lift and nose-down pitching moment overshoots by means of spanwise pressure measurements over a rotor blade. In particular, the experimental results show the occurrence of large lift and pitching moment transients especially between 77% and 92% of the rotor radius in the first quadrant of the disk and for an azimuthal position of 270° that corresponds to the retreating side of the rotor. The rapid airloads overshoots produce high structural loads and stresses that can exceed the blades and the pitch links control system fatigue limits[14].

The three-dimensional effects of dynamic stall have been studied experimentally also in the works by Lorber [15], Pizialli [16] and Berton [17]. In particular, the first two works used a cantilevered semi-span pitching blade instrumented with miniature pressure transducers at various stations along the span and chord; this set up enabled to measure the sectional lift and pitching moment.
For instance, the unsteady lift curves measured at different span sections for deep dynamic stall conditions reveal a behavior similar to those found on oscillating 2-D airfoils, as the airload exhibits the same overshoots and hysteresis effects. When moving outboard on blade span the phenomenon

resumes a mitigation of the airloads hysteresis. This feature can be considered associated with a reduction of the effective angle of attack induced by the tip vortex that dominates the flow field in this region; consequently, the effective angle of attack of the blade never becomes large enough to produce the flow separation on the airfoil upper surface.

Chapter 2

Experimental rig

2.1 The wind tunnel

The experimental activity has been conducted at Politecnico di Milano in the low-speed closed-return wind tunnel of the Aerodynamics Laboratory (see Fig. 2.1. The wind tunnel has a rectangular test section with 1.5 m height and 1 m width. The maximum wind velocity is 55 m/s and the turbulence level is less than 0.1%.

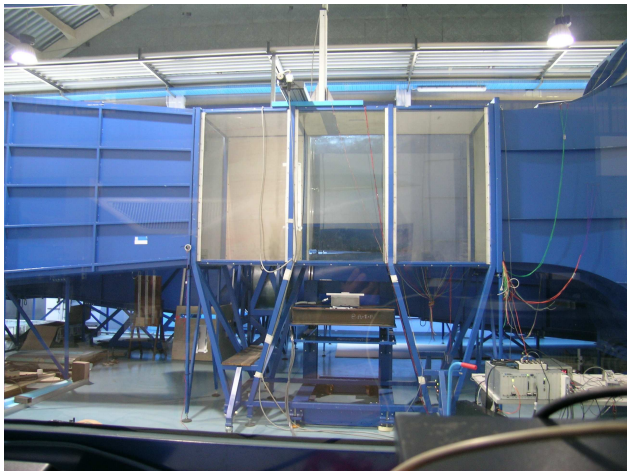

Figure 2.1: Test section of the low-speed wind tunnel at the Aerodynamics Laboratory of Politecnico di Milano

2.2 The blade section model

The first step of the oscillating airfoil rig project has been the design of a two-dimensional blade section model that is moved in pitch around its quarter chord. Two different blade section models with NACA 23012 and NACA 23015 have been designed and manufactured. The NACA 23012 airfoil has been selected since, being a typical helicopter blade airfoil, it has been employed in experimental activities in the past years about the study of the dynamic stall phenomenon on pitching blade sections [25, 37] and consequently offers the possibility to compare the test results with the literature, useful for the validation of the rig performance and the measurement techniques set up. The NACA 23015 has been essentially used for the tests with trailing edge self-activated movable flaps in order to compare their effects on two airfoils with different thickness (as described in Chapter).
The blade section model has a 0.3 m airfoil chord and a 3.1 aspect ratio. The chord dimension is typical of a medium size full-scale helicopter rotor blade.

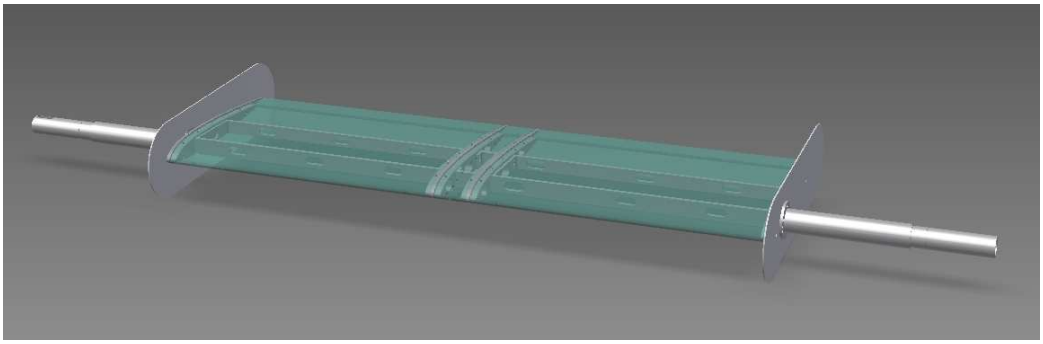

Figure 2.2: Layout of the NACA 23012 blade section model.

The NACA 23012 blade section model is composed by three aluminium machined external sections (3 mm thickness) attached on an internal metallic frame also in aluminium (see Fig. 2.2). The total weight of the model is about 8.75 kg. The internal metallic frame is composed by four airfoil ribs connected by three wing boxes. Each end rib is connected to a steel tubular shaft with axis on the 25% of the chord. The design of the NACA 23015 blade model resumes the same characteristics of the NACA 23012 model except by the fact that the external sections have been manufactured in an aluminium-based thermoplastic resin (alumide) by means of the rapid prototyping tech-

nique; in particular, the external sections present a 5 mm thickness and the central section has a higher span (90 mm instead of 50 mm). The models present an interchangeable midspan section for the different measurements techniques employed; in particular two central sections have been designed and constructed, one for PIV flow surveys and another for unsteady pressure measurement equipped with pressure taps positioned along the midspan chord line. End plates were used during the tests to minimize interference effects of the wind tunnel walls boundary layer.

2.3 Experimental rig set up

The pitching airfoil rig has been designed following the indications of similar experimental apparatus described in literature [18, 19]. In particular, the layout of the dynamic stall rig has been designed consisting in the blade section model supported by a motorized strut that can move it in pitch around its quarter chord, as can be seen in Fig.2.3.
The blade section model is mounted horizontally in the wind tunnel test section and is pivoted about the quarter-chord position on the two tubular steel shafts positioned on self-aligning bearings, see Fig. 2.4 and Fig. 2.5.
The model is installed on a heavy metallic supporting structure composed by steel beams and aluminium profiles on which are connected the tubular shafts, as can be observed in Fig. 2.6. The total weight of the support structure is about 400 kg.
The blade model pitching motion is driven by a brushless servomotor with a gear drive. The driving mechanism is positioned on a cantilevered aluminium profile. The model is connected to the driving mechanism by a torsionally stiff steel laminae coupling between the model tubular shaft and the gear drive that allows angular and axial displacements, as can be seen in the particular of the motorized strut in Fig. 2.7.

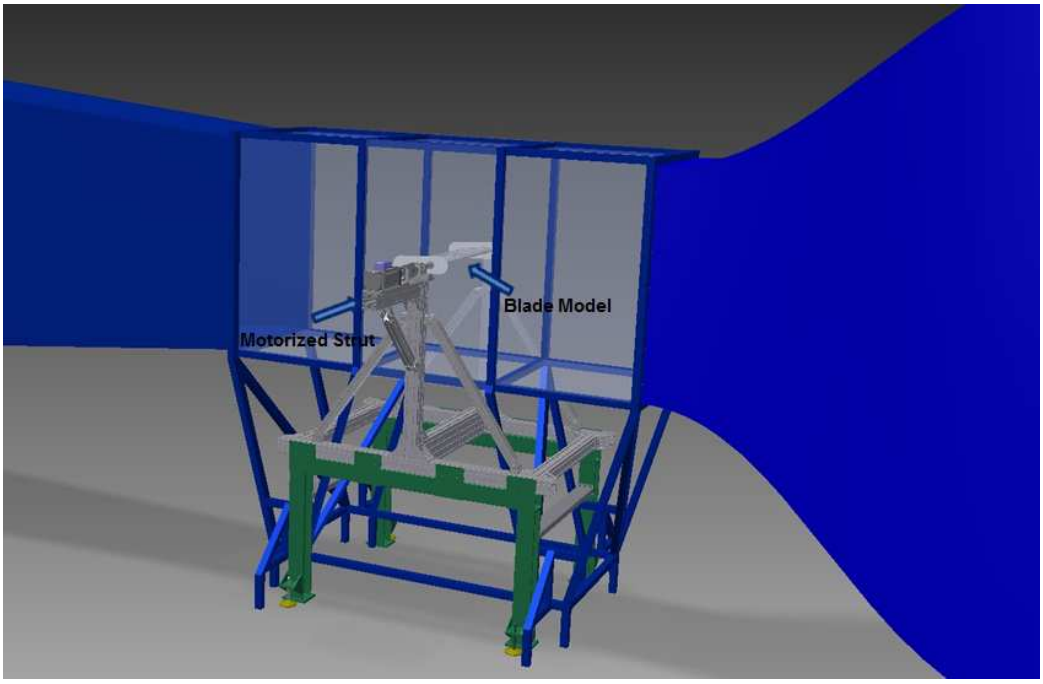

Figure 2.3: Dynamic stall rig layout in the wind tunnel.

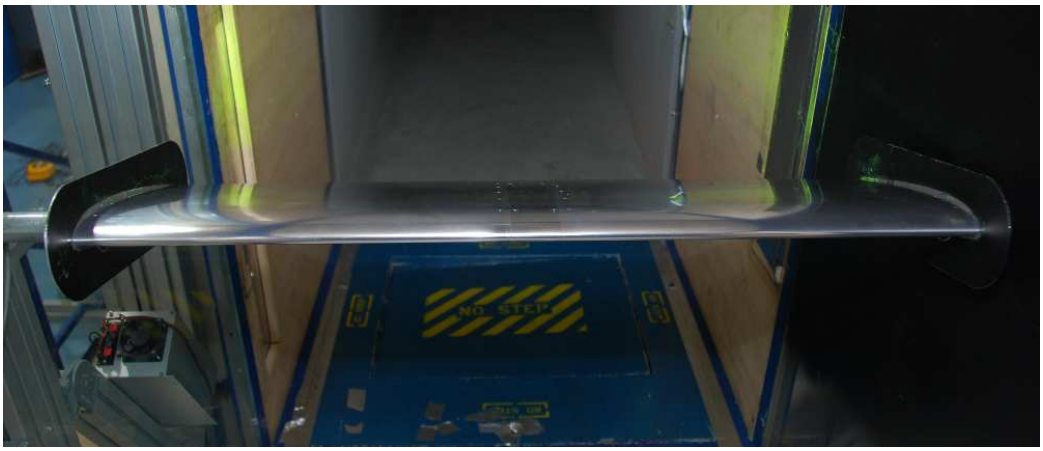

Figure 2.4: NACA 23012 blade section model inside the wind tunnel.

Two encoders are mounted directly on one external shaft (see Fig. 2.8): in particular, a 2048 *imp/rev* absolute digital encoder with **EnDat 2.2** protocol is used for feedback control and a 4096 *imp/rev* incremental analog

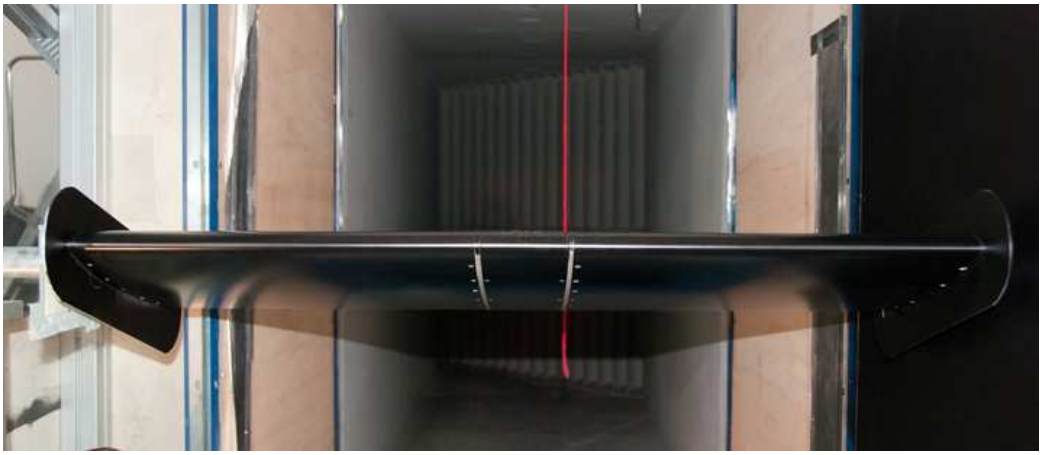

Figure 2.5: NACA 23015 blade section model inside the wind tunnel.

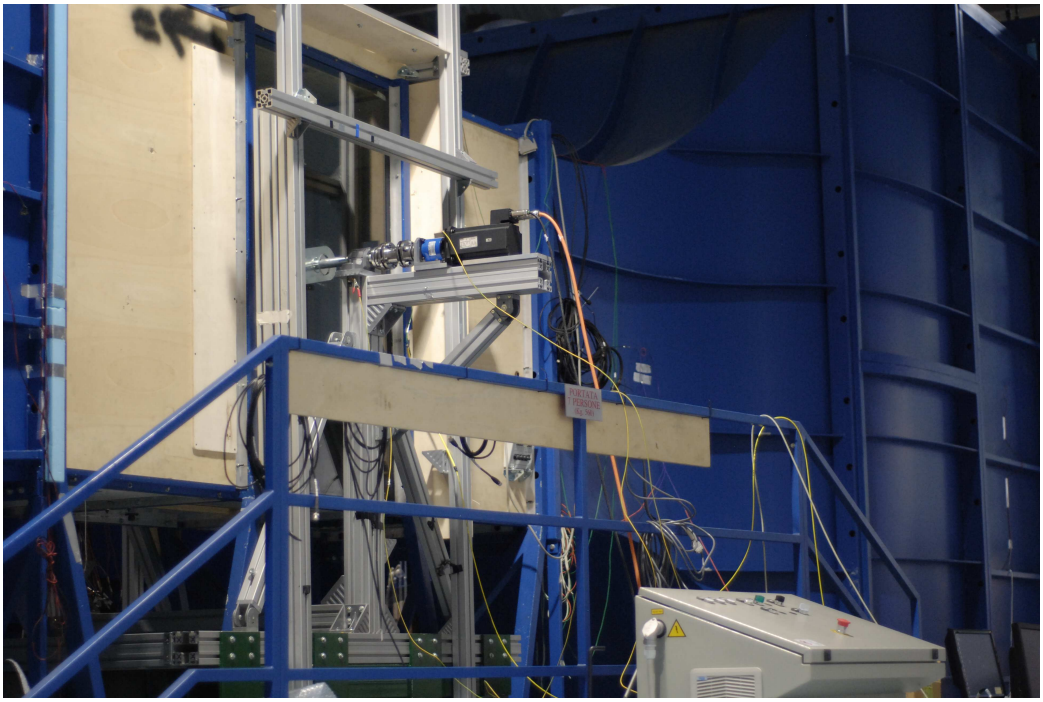

Figure 2.6: Set up of the dynamic stall rig in the wind tunnel.

encoder is used to determine the model instantaneous position.
The performance of the driving mechanism in terms of maximum continu-

Figure 2.7: Particular of the motorized strut.

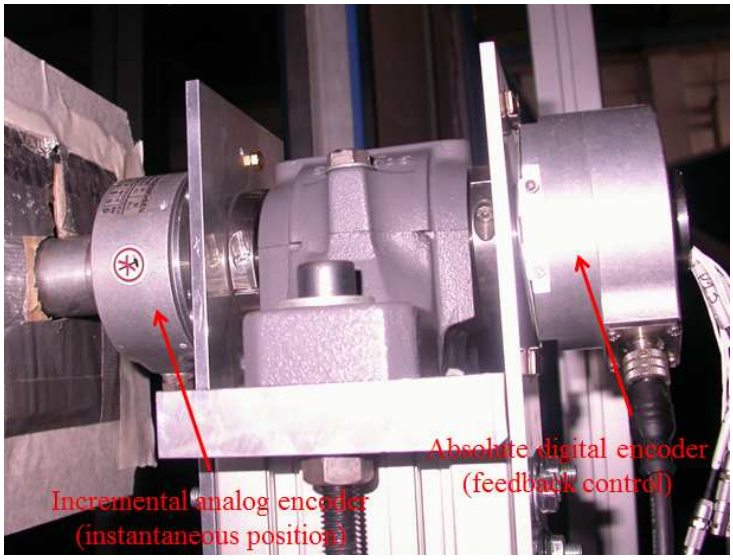

Figure 2.8: Particular of the external shaft with the encoders.

ous torque and angular velocity has been evaluated during the early stage of the rig design with the aim of reproducing the deep dynamic stall condition of a full-scale retreating rotor blade section at 75% radius at high forward

flight speed. The selected dimensioning condition has been a pitching cycle characterised by 15° mean angle attack, 15° oscillation amplitude and a reduced frequency $k = 0.1$ with a free-stream wind tunnel velocity of 50 m/s corresponding to $Re = 1 \cdot 10^6$. The unsteady aerodynamic airloads for the assumed dimensioning condition have been preliminary evaluated using the Theodorsen approach for a two-dimensional harmonically oscillating airfoil in incompressible flow [20]. Moreover, also the inertia characteristics of the blade section model have been taken in account to evaluate their contribute to the maximum dimensioning torque. The calculation of the maximum required performance for the driving mechanism produced a maximum torque of about 30 Nm and a maximum angular velocity of about 83 rpm. In order to satisfy the dimensioning requirements, the driving mechanism has been composed by a servomotor with 10 Nm maximum continuous torque and a 12:1 gear drive. This solution provides 120 Nm continuous torque with a 250 rpm maximum angular velocity allowing to get a conspicuous performance overhead respect to the dimensioning condition, enabling the possibility to test other full-scale blade section models with chord in the range of $0.3 - 0.5$ m (large size helicopter blades).

2.4 Blade model FEM structural analysis

A finite element structural analysis has been carried out for the blade section models using **MD Nastran** [56].
The blade models have been meshed using solid tetrahedral elements for the internal structure (see Fig. 2.9(a)) and plates two-dimensional elements for the external sections (see Fig. 2.9(b)).
The structure of the blade models are constrained at the external shafts not allowing all the translations and the rotations. As a first step, a modal analysis has been carried out in order to verify the separation of the blade modal frequencies from the maximum pitching frequency planned for the experimental campaign.
The results of the modal analysis for the NACA 23012 blade model illustrated in Fig. 2.10 demonstrate that the frequency of the first bending mode, equal to 111.15 Hz, is well above the 5.3 Hz pitching motion frequency corresponding to the reduced frequency of a retreating helicopter blade in forward flight ($k = 0.1$). The same consideration is valid also for the NACA 23015 blade section model as the first bending mode is equal to 68.79 Hz.

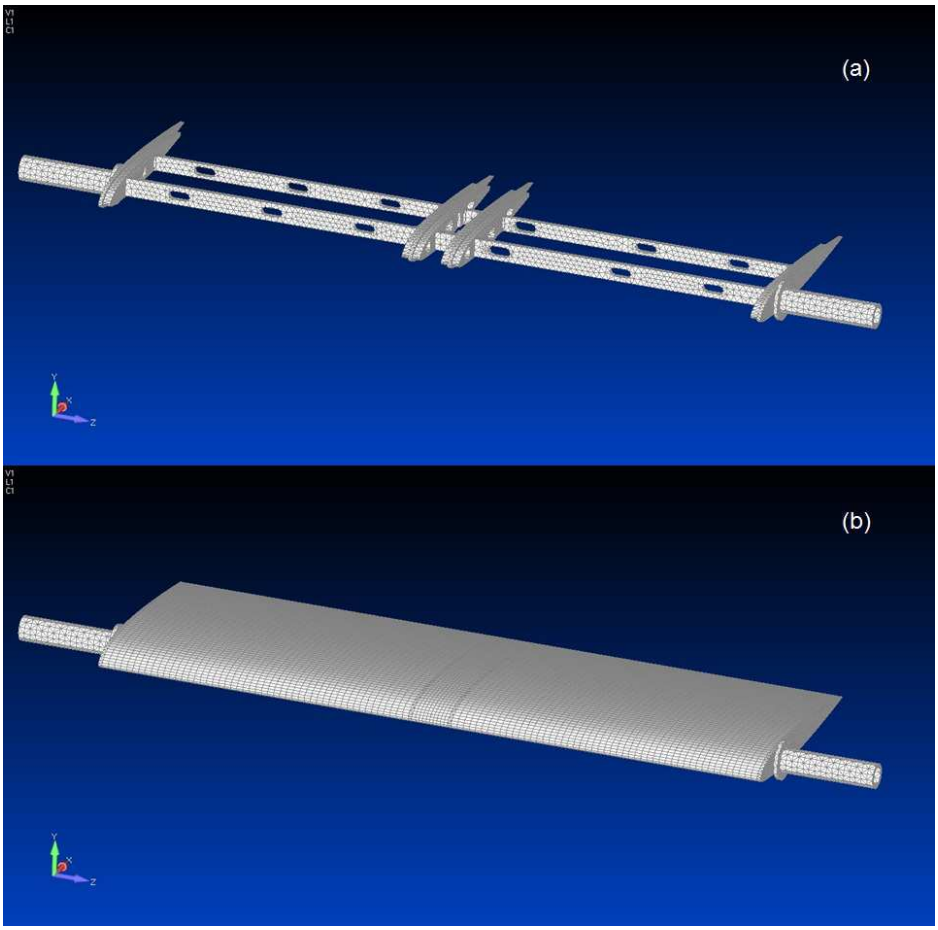

Figure 2.9: Structural mesh of the NACA 23012 blade section model: (a) internal structure meshed with solid tetrahedral elements; (b) external sections meshed with plates two-dimensional elements.

Then, a static structural analysis has been carried out on the blade models loaded. In particular, a torque of 50 Nm around the pitching axis has been applied on the model center of gravity nodal point, considering a value higher than the maximum torque evaluated for the dimensioning condition considering both the aerodynamic and inertia contributetions. The torque is distributed to all the nodal points of the internal structure by means of a rigid body element (RBE3 [56]). The lift maximum value evaluated with the

Theodorsen model [20] for the dimensioning condition has been distributed to all the nodal points of the model external sections with a triangular law in chord. The ratio between the heights of the aerodynamic force triangular distributions on the airfoil upper and lower surface corresponds to the static stall angle of attack condition evaluated with XFoil [36].

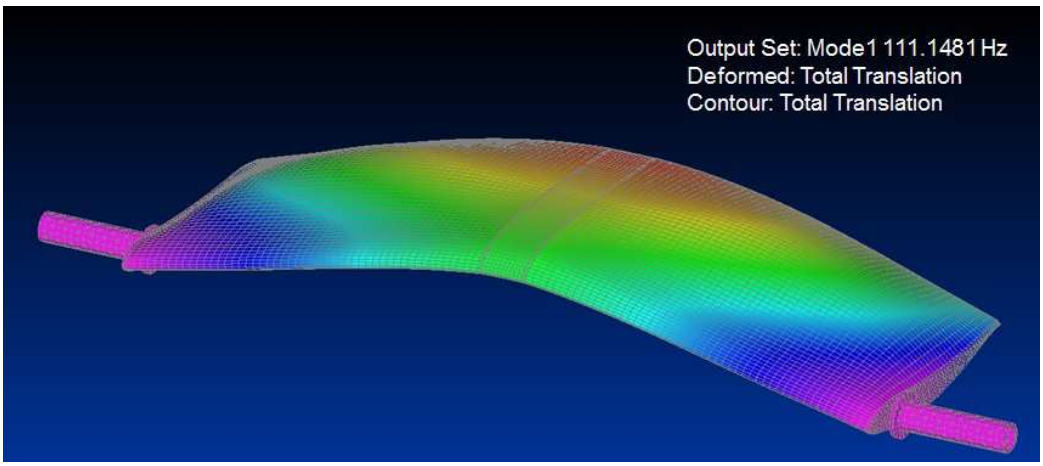

Figure 2.10: Modal analysis results for the NACA 23012 blade section model: first bending mode at 111.15 Hz.

The results of the static structural analysis for the NACA 23012 blade model illustrated in Fig. 2.11 demonstrate that the maximum stress for the considered load condition is lower than the yield point of the aluminium used for the project. In particular, the maximum evaluated stress value is about 53 MPa in the internal structure and about 21 MPa in the external sections, while the yield point of the aluminium employed is about 350 MPa (see 2.11).The maximum displacement evaluated for the model external sections is less than 1 mm, then the airfoil aerodynamic behavior can be considered not compromised. The same consideration can be considered valid also for the NACA 23015 blade section model as the maximum displacement evaluated for this model under the same load condition is a little higher than 1 mm; consequently, the NACA 23015 model is less rigid than the NACA 23012 model and this behavior can be explained by the lower mechanical properties of the material used to manufacture the external sections respect to the aluminum, even if they present a higher thickness (5 mm instead of 3 mm).

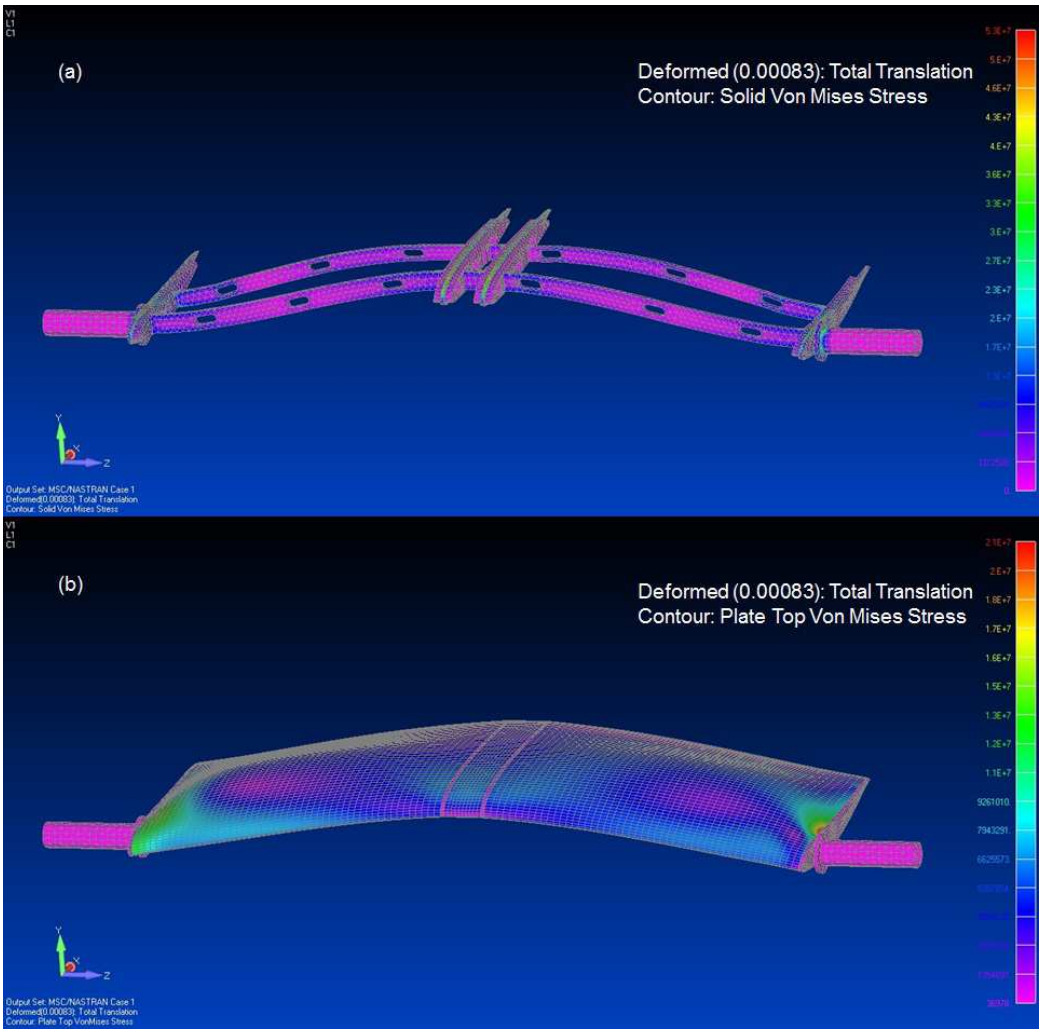

Figure 2.11: Static structural analysis results for the NACA 23012 blade section model: (a) contours of solid Von Mises stresses on the internal structure; (b) contours of plate Von Mises stresses on the external sections.

2.5 Control of the pitching mechanism

The model sinusoidal pitching motion and the pitching cycle parameters, for instance, the mean angle of attack, the amplitude and the oscillation frequency, are controlled by an interface software implemented in **Labview** [21] (see Fig. 2.12).

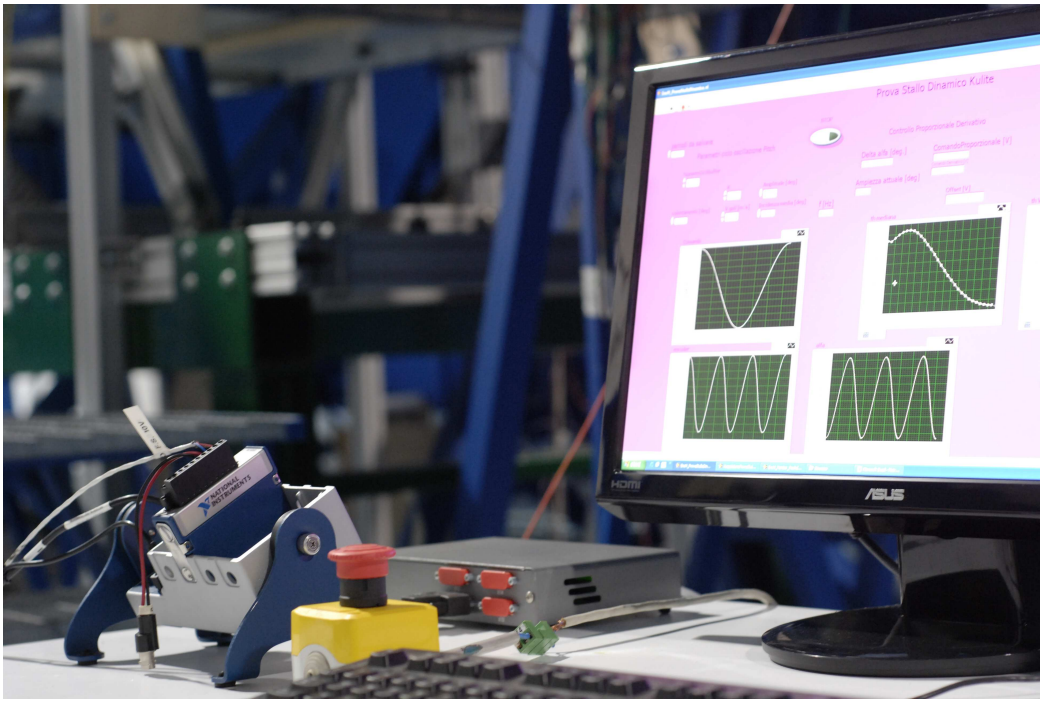

Figure 2.12: Particular of the pitching system control desk.

The motion of the motor shaft is governed by a voltage analog signal sent as input to the motor servodrive with a sinusoidal law in velocity. The command signal is controlled by a proportional and derivative action on a period T that covers a number of oscillating cycles selected by the user.
The error parameter of the proportional control is the deviation of the model angular position mean value (on a period T) measured by the encoder feedback from the mean angle of attack of the requested oscillating cycle ($\Delta\alpha_m T$).
The error parameter of the derivative control is the variation in time of the proportional control error parameter. Moreover, a control on the oscillating cycle amplitude is applied using a factor equal to the ratio between twice the amplitude of the requested oscillating cycle and the angular position peak to peak value on a period (Q_{α_0}).
Figure 2.13 illustrates the layout of the implemented control system for the pitching drive mechanism.

The performance of the control system allows to obtain an error in posi-

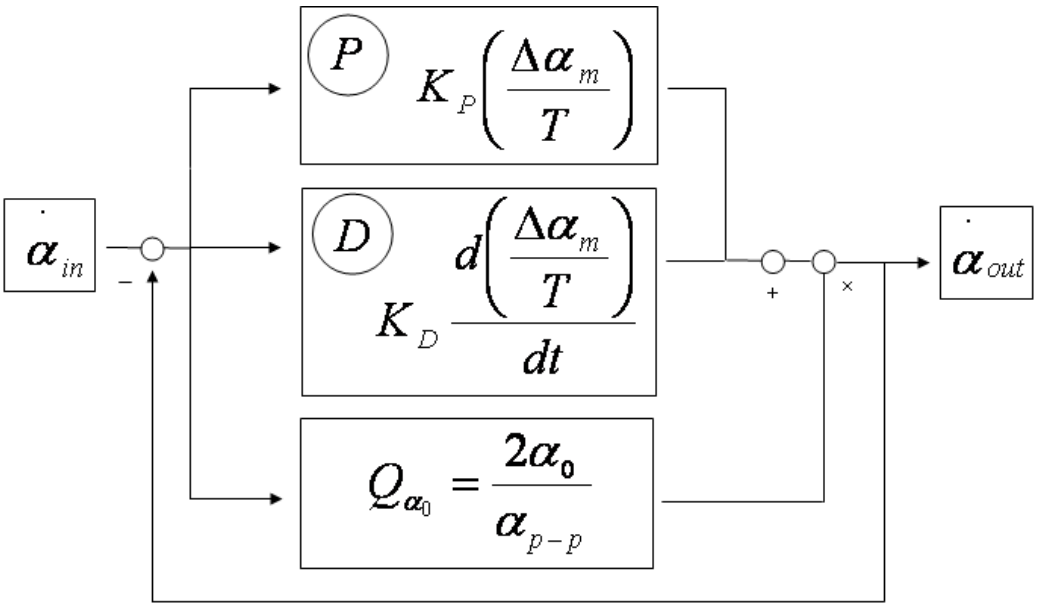

Figure 2.13: Layout of the implemented control system for the pitching drive mechanism.

tion $\Delta\alpha_m$ less than 0.1° after few oscillation periods.

2.6 Measurement techniques set up

2.6.1 Unsteady pressure measurement

The airloads during a pitching cycle have been evaluated by means of unsteady pressure measurements in correspondence of the pressure taps on the model midspan section.
The midspan chord line of the model central section is instrumented with 21 **Kulite XCS-093** unsteady pressure transducers (accuracy 0.15% FSO) with a slight increase in concentration near the leading edge. Table 2.1 and 2.2 presents the positions of the surface pressure taps for the two blade section models, starting from the leading edge and following a closed loop from the upper to the lower surface.

The very thin region of the airfoils at the trailing edge does not allow to arrange a pressure transducer after the 90% of the chord. Each pressure transducer is positioned in a straight or L-shaped nylon machined pipe and

#	x/c	#	x/c	#	x/c
1	0	8	0.453	15	0.459
2	0.01	9	0.618	16	0.373
3	0.044	10	0.76	17	0.285
4	0.096	11	0.9	18	0.185
5	0.164	12	0.9	19	0.118
6	0.28	13	0.767	20	0.06
7	0.358	14	0.628	21	0.02

Table 2.1: Pressure taps location on the NACA 23012 model midspan section.

#	x/c	#	x/c	#	x/c
1	0	8	0.478	15	0.485
2	0.052	9	0.616	16	0.362
3	0.032	10	0.755	17	0.253
4	0.077	11	0.9	18	0.16
5	0.146	12	0.85	19	0.091
6	0.242	13	0.757	20	0.044
7	0.353	14	0.618	21	0.014

Table 2.2: Pressure taps location on the NACA 23015 model midspan section.

sealed with a miniature rubber o-ring. The signal cables pass through the model internal frame and come out from the external tubular shaft opposite to the motor; this solution enables to reduce the stresses on the cables during the oscillation cycles (see Fig. 2.14).

Figure 2.14: Particular of the pressure transducers cables.

Figure 2.15 present the particular of the NACA 23012 model central section instrumented with the pressure transducers.

The pressure signals acquisition has been carried out using a **National Instruments** compact data acquisition system **cDAQ-9172** equipped with six **NI 9237** 24 bit simultaneous bridge modules. The transducers signals have been acquired with 50 kHz simultaneous sampling rate on 21 channels for a time period corresponding to 30 complete pitching cycles. The high sampling rate has been suggested to capture the fine detail of the dynamic stall phenomenon characterised by severe unsteadiness conditions, especially for the tests with high reduced frequency ($k = 0.1$). The model angular position has been measured simultaneously to the pressure transducers signals by means of the incremental encoder mounted directly on the model tubular shaft opposite to the motor. The simultaneous acquisition of the encoder signals has been used for the evaluation of the phase averaged airloads.

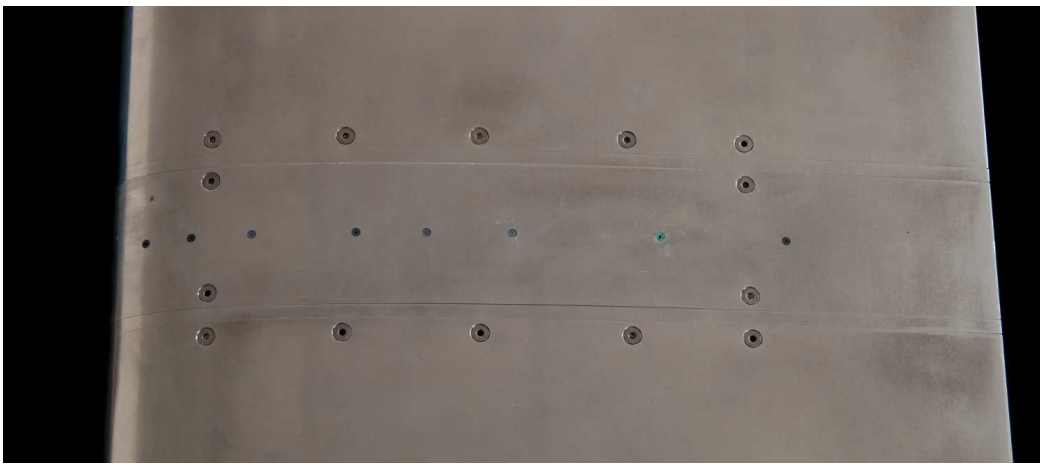

Figure 2.15: Particular of the NACA 23012 model central section for unsteady pressure measurements.

2.6.2 Particle Image Velocimetry set up

Figure 2.16 shows the layout of the PIV instrumentation set up in the wind tunnel for the velocity field measurement on the upper surface of the pitching airfoil.
A **Pixelfly PCO** double shutter CCD camera with a 12 bit, 1280×1024 pixel array and a 55 mm **Nikon** lens have been used to acquire the image pairs. In order to get more resolution of the image pairs, the measurement window for this application was nominally 103 $mm \times 82$ mm, then, to perform the flow survey above the entire airfoil upper surface, the measurement field has been composed by 4 measurement windows spanning the airfoil chord direction with a small superposition length at the edges of each window. The CCD camera has been mounted on a dual axis traversing system guided by two stepper motors that allowed to move the measurement window along two orthogonal directions (see 2.17).
The PIV system used a **Dantec Dynamics** Nd:Yag double pulsed laser with 200 mJ output energy and a wavelength of 532 nm. The laser sheet passed through an opening in the wind tunnel roof aligned with the flow and positioned at the midspan of the test section width. The laser has been mounted on a single axis traversing system to move the sheet along the wind tunnel flow direction, enabling the use of a smaller width sheet with higher energy centered on each measurement window.

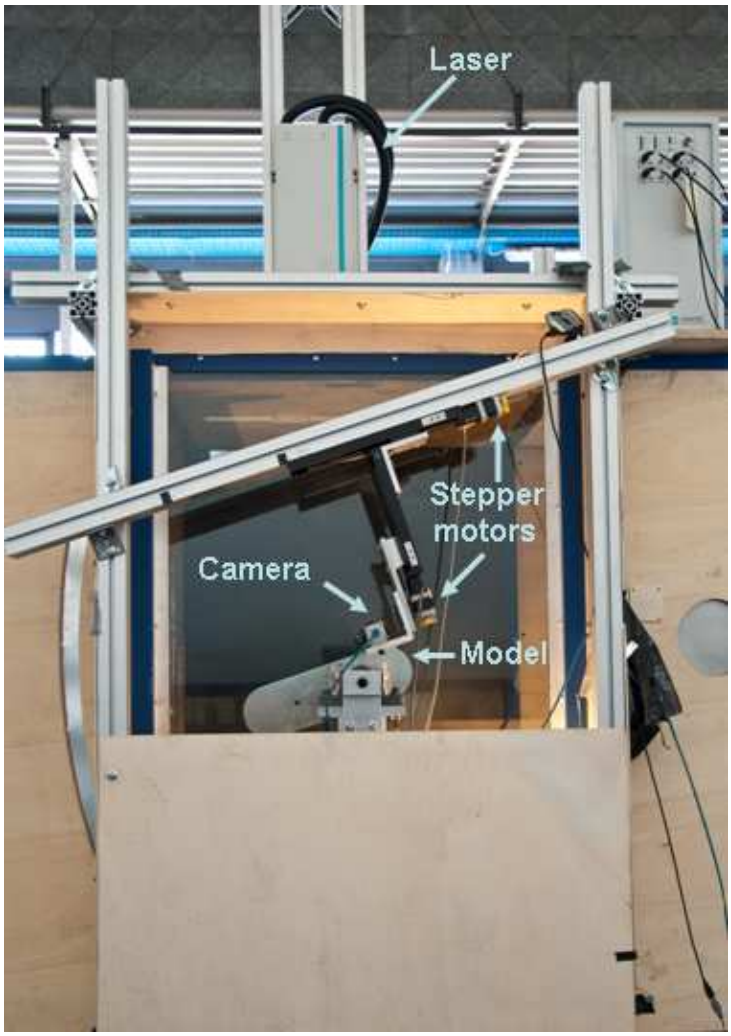

Figure 2.16: PIV setup in the wind tunnel test section.

The laser and the camera have been mounted on a external metallic structure made of aluminium profiles that is connected to the heavy basement of the rig in order to avoid the transfer of the wind tunnel vibrations to the PIV measurement devices, specially during the tests at high speed.
The tracer particles have been injected in correspondence of a wind tunnel section just after the fans and consisted in small oil droplets with diameter in the range of $1 - 2\ \mu m$ generated by means of a particle generator (**PIVpart30** by **PIVTEC**) with Laskin atomizer nozzles.

Figure 2.17: Particular of the double shutter camera mounted on a dual axis traversing system.

The PIV instrumentation has been controlled by an interface software implemented in **MATLAB** [22]. The software controlled the synchronization of the two laser pulses emission with the exposure of the image pairs by the camera. In particular, the software sends commands using the **RS-232** protocol to a 6 channels **Quantum Composer 9618** pulse generator. The pulse generator receives as input a trigger signal when the encoder reads the model position corresponding to the airfoil angle of attack selected by the user for the PIV measurement. Starting from the external trigger, the pulse generator controls the time sequence of the image pairs exposure as well as the lasers and Q-switches pulses, following the layout reported in Fig. 2.18.

The time sequence has been evaluated taking in account the Δt delay of the image pairs, that can be selected by the user depending on the test velocity, the camera time jitters and the Q-switch delays respect to the laser pulses reported on the laser data sheet and reproduced to optimize the energy emission of the two lasers.

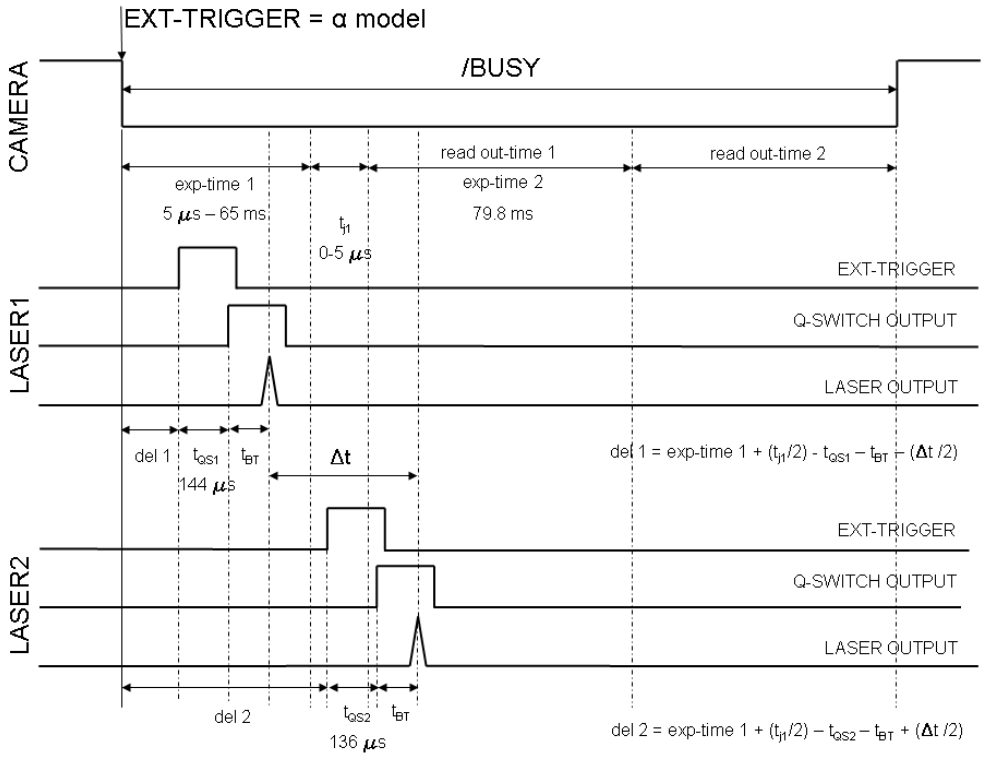

Figure 2.18: Layout of the implemented control system for the PIV instrumentation.

Before the PIV measurements, a calibration of the measurement window has been done to evaluate the image magnification. For the calibration, an equispaced grid positioned on the midspan section of the model has been used. The image pairs post-processing has been carried out by means of the **PIVviev 2C/3C** software [23], developed by PIVTEC in close cooperation with the PIV-Groups of the German Aerospace Center (DLR) in Gottingen and Cologne. The PIVview software is a complete PIV evaluation program including the implementation of advanced processing algorithms as multiple-pass and multiple-grid methods [23, 38].

Chapter 3

Experimental results

3.1 Unsteady pressure measurements

The main goal of the unsteady pressure measurements has been the complete characterisation of the NACA 23012 airfoil performance testing a large number of different pitching cycle conditions, typical of the flight envelope of a helicopter rotor retreating blade in forward flight. In this aim, the pitching cycles parameters, as mean angle of attack α_M, oscillation amplitude α_0 and reduced frequency k, have been changed systematically in order to analyse the characteristics of the airloads time histories in the light and deep dynamic stall regimes [1]. The most of the dynamic tests have been carried out at $k = 0.1$ with $Re = 1 \cdot 10^6$ and $Ma = 0.15$, in order to reproduce the condition of a full-scale retreating rotor blade section at 75% radius in forward flight. A few tests have been carried out also at $Re = 6 \cdot 10^5$ to evaluate the effect of the Reynolds number.
The time history of the lift and pitching moment has been obtained by the integration in chord of the phase averaged pressure signals, using a bin of 0.1° angle of attack amplitude. The presented dynamic results are not corrected by the wind tunnel effects because well-established correction methods are not available for pitching airfoils, in particular for high oscillation amplitudes [30].
The standard deviation of the airloads coefficients have been evaluated for dynamic tests and plotted on the measured airloads curves. In order to improve the clearness of the dynamic curves, in the following figures the symmetric standard deviation of the airloads measurements is plotted every

five bins (0.5° angle of attack).

3.1.1 Static tests

Before the dynamic tests, static tests have been carried out at $Re = 1 \cdot 10^6$ in order to validate the airloads measurement technique.
Figure 3.1 presents the comparison of the static $C_L - \alpha$ curve with the curve measured by NACA; the C_L are corrected by the wind tunnel wall effects [57, 58]. The static $C_L - \alpha$ curves present a very good agreement in the total range of considered angles of attack.

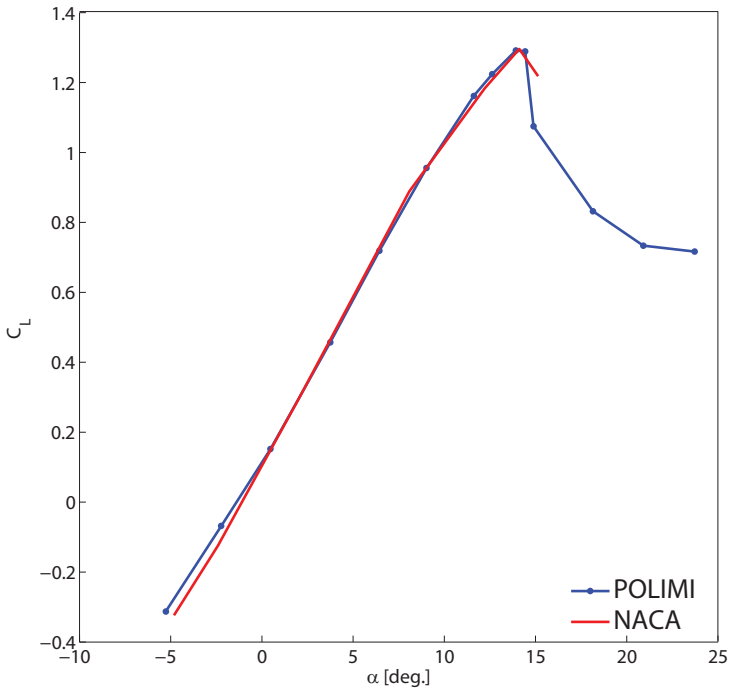

Figure 3.1: Comparison of the steady $C_L - \alpha$ curves for the NACA 23012 airfoil at $Re = 1 \cdot 10^6$.

3.1.2 Effect of mean angle of attack

The effects of mean angle of attack variations have been evaluated reproducing pitching cycles with α_M in the interval between 5° and 20° with a

constant oscillation amplitude of 10° and a reduced frequency equal to 0.1. Many physical features of the flow could be simply deduced by the pressures measurements taking into account the observation of other authors, as Leishman[25] and McCroskey [1].
The conditions tested reproduce the two different regimes, light and deep dynamic stall. In particular, in the former regime the maximum angle of attack reached by the blade model during the sinusoidal oscillation is near the airfoil static stall angle of attack. As can be seen from the results of the test with $\alpha_M = 5°$ in Fig. 3.2, this regime is characterised by minor flow separation from the airfoil as the flow is attached during almost the whole pitching cycle and consequently the airload curves present a small amount of hysteresis.

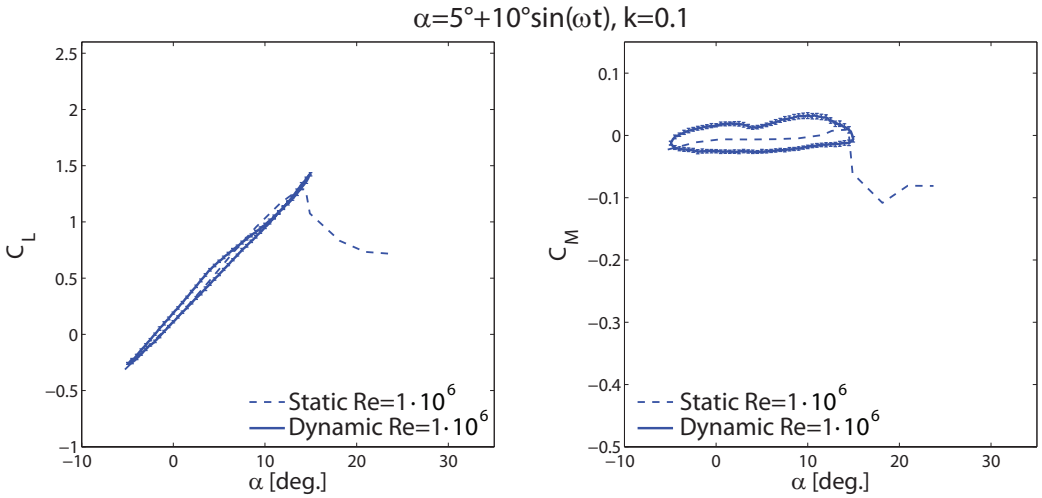

Figure 3.2: Lift and pitching moment curves for NACA 23012 pitching with $\alpha(t) = 5° + 10° sin(\omega t)$ at $Re = 1 \cdot 10^6$ (*Light Dynamic Stall* regime).

The conditions tested with $\alpha_M = 10°$, 15° or 20° represent the deep dynamic stall regime as the maximum angle of attack reached by the blade model is above the airfoil static stall angle of attack and the oscillation amplitude is conspicuous. This regime is characterised by the vortex-shedding phenomenon and a high amount of hysteresis as, during a larger part of the pitching cycle, the flow is separated.
Figure 3.3 presents the airloads curves measured in the test with $\alpha_M = 10°$

at two different Reynolds numbers, $Re = 6 \cdot 10^5$ and $Re = 1 \cdot 10^6$.

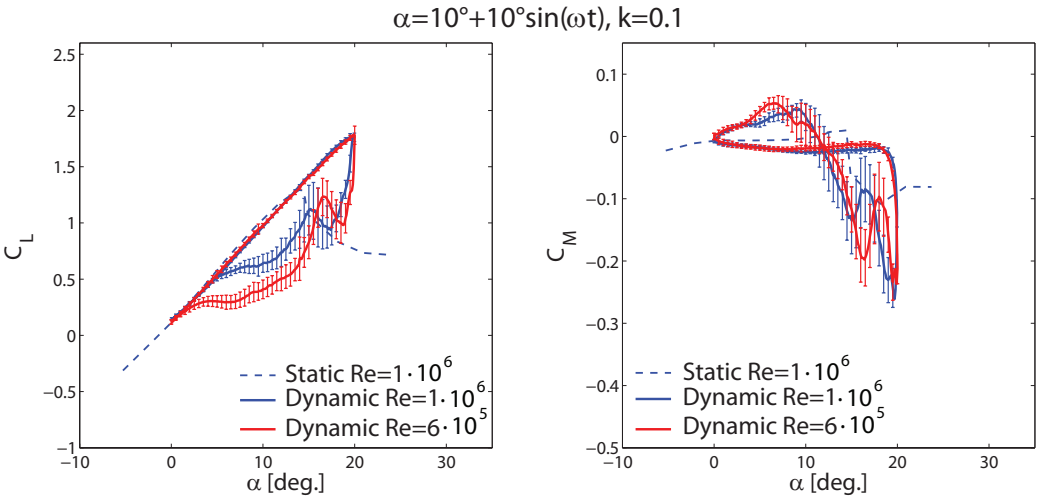

Figure 3.3: Lift and pitching moment curves for NACA 23012 pitching with $\alpha(t) = 10° + 10° sin(\omega t)$ at $Re = 6 \cdot 10^5$ and $Re = 1 \cdot 10^6$ (*Deep Dynamic Stall* regime).

As can be observed from the $C_L - \alpha$ curve, during the upstroke motion the lift grows linearly to a maximum value higher than static stall value, as the flow separation is delayed by a reduction in adverse pressure gradients produced by a kinematic induced camber effect due to the positive rapid pitching rate [5, 7]. In fact, for this test condition, the separation does not occur during almost all the upstroke motion.
The flow is completely separated for almost all the downstroke motion, as the flow reattachment occurs only at 4° angle of attack, well below the static stall angle. The lag of the flow reattachment process during the downstroke motion of the airfoil is explained by a negative induced camber effect produced by the negative pitching rate [10].
The different behavior of flow topology during the motion of upstroke and downstroke produces an asymmetry of the airloads with respect to the motion of the body and a large amount of hysteresis. It has to be outlined that a net negative aerodynamic damping, as in this case, produced by a higher area of C_M clockwise loop respect to the anticlockwise one could lead to the stall flutter occurrence described in Sec.1.2 [6].

Figure 3.4 presents the airloads curves measured in the test with $\alpha_M = 15°$ at two different Reynolds numbers, $Re = 6 \cdot 10^5$ and $1 \cdot 10^6$.

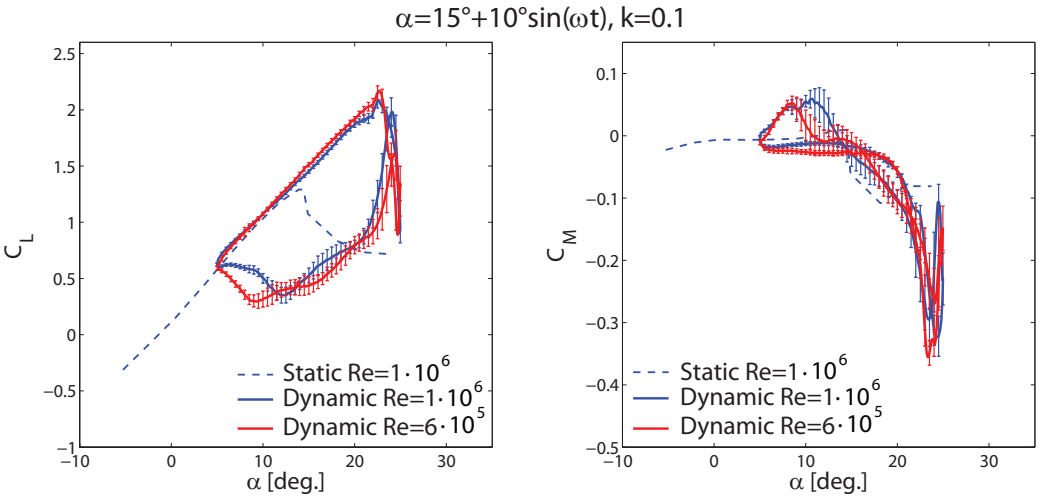

Figure 3.4: Lift and pitching moment curves for NACA 23012 pitching with $\alpha(t) = 15° + 10° sin(\omega t)$ at $Re = 6 \cdot 10^5$ and $Re = 1 \cdot 10^6$ (*Deep Dynamic Stall* regime).

As can be observed from the airloads curves, this test condition is characterised by the vortex-shedding phenomenon.
In fact, at about $\alpha = 20°$ during the upstroke motion, the flow separation starts with the formation of a small vortical disturbance that quickly rolls up and grows sweeping downstream over the airfoil upper surface. This issue is probably the main feature of the dynamic stall process and is described in literature as *Dynamic Stall Vortex* (**DSV**) [1]. The **DSV** grows sweeping downstream over the airfoil upper surface with a speed between one third and one half of the free-stream velocity [8, 9]. The change in pressure distribution over the airfoil upper surface due to the **DSV** migration produces a non-linear change of the $C_L - \alpha$ curve slope between $\alpha = 20°$ and $\alpha = 23°$. The vortex sweep produces also a significant increase in nose-down pitching moment resulting from an aft movement of the center of pressure and consequently an increase in torsional loads. Another interesting aspect introduced by the (**DSV**) migration is the delay between the pitching moment break, that occurs at about $\alpha = 20°$ and the lift stall, that occurs at about $\alpha = 23°$; in fact, the pitching moment divergence starts at the stage of the

vortex disturbance formation, while the lift stall occurs as the vortex detaches the airfoil passing into the wake. The stage of vortex detachment at about $\alpha = 24°$ is accompanied by rapid overshoots of lift and pitching moment.
At the beginning of the downstroke motion, the airloads curves present secondary peaks of lift and pitching moment due to the formation and convection over the airfoil chord of a secondary vortex. During the downstroke motion the flow is completely separated for all the downstroke motion, as the flow reattachment occurs when the airfoil restarts the upstroke motion.
As can be observed from the tests results presented in Fig.3.3 and 3.4, the Reynolds effect on the measured dynamic airloads curves is quite small, as the lift and pitching moment curves present the same behavior corresponding to the occurrence during the pitching cycle of the same characteristic aerodynamic features so that can be reasonably assumed that the main aerodynamic phenomena are the same at the two Reynolds numbers.

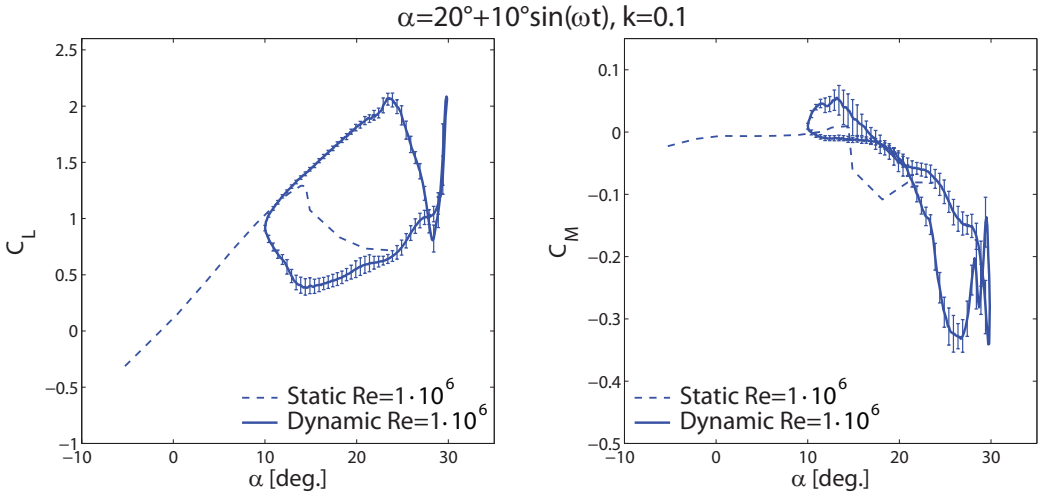

Figure 3.5: Lift and pitching moment curves for NACA 23012 pitching with $\alpha(t) = 10° + 10° sin(\omega t)$ at $Re = 1 \cdot 10^6$ (*Deep Dynamic Stall* regime).

Figure 3.5 presents the airloads curves measured in the test with $\alpha_M = 20°$ at $Re = 1 \cdot 10^6$, that represents the most severe condition tested in the deep dynamic stall regime.
The airloads curves present a quite interesting behavior; in fact, it is possible to notice a secondary peak near the end of the upstroke motion. This

feature occurs also at the beginning of the downstroke motion for the test condition characterised by $\alpha_M = 15°$, as mentioned earlier; this behavior is explained by the formation of a secondary vortex that moves on the airfoil upper surface.

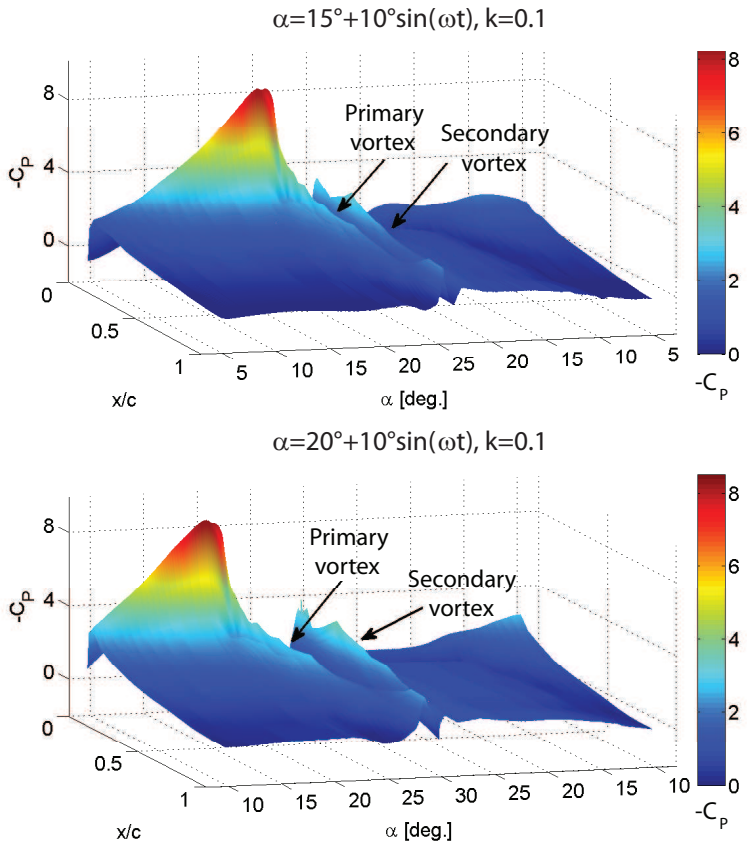

Figure 3.6: Pressure coefficient time history on the airfoil upper surface in *Deep Dynamic Stall* conditions at $Re = 1 \cdot 10^6$.

The convection of the two vortex for these two test conditions is clearly visible in Fig.3.6 that shows the time history of the pressure coefficient C_P on the airfoil upper surface during the whole pitching cycle. The primary vortex, for both the test conditions, starts at about $\alpha = 21°$ in upstroke, producing a pressure divergence at the trailing edge as it moves over the chord. The

secondary vortex occurs at the beginning of the downstroke motion (about $\alpha = 24°$) for the test with $\alpha_m = 15°$ and at the end of the upstroke (about $\alpha = 28°$) for the test with $\alpha_m = 20°$. For both the test conditions the formation of the secondary vortex produces a pressure wave that convects faster than the primary over the chord.

In Fig.3.7 the dynamic airloads curves measured for three pitching cycles conditions at $Re = 1 \cdot 10^6$ are compared with the curves measured in the work by Leishman [25] at $Re = 1.5 \cdot 10^6$. For the test condition with $\alpha_M = 6°$ and $\alpha_M = 10°$ the airloads curves are in good agreement. For the test condition with $\alpha_M = 20°$, characterised by very high angles of attack, the curves presents the same behavior but with sensibly different values of the lift and pitching moment coefficients. Although the different Reynolds number has to be considered, the most of the differences between the present results and the reference work could be due to the differences of the set up.

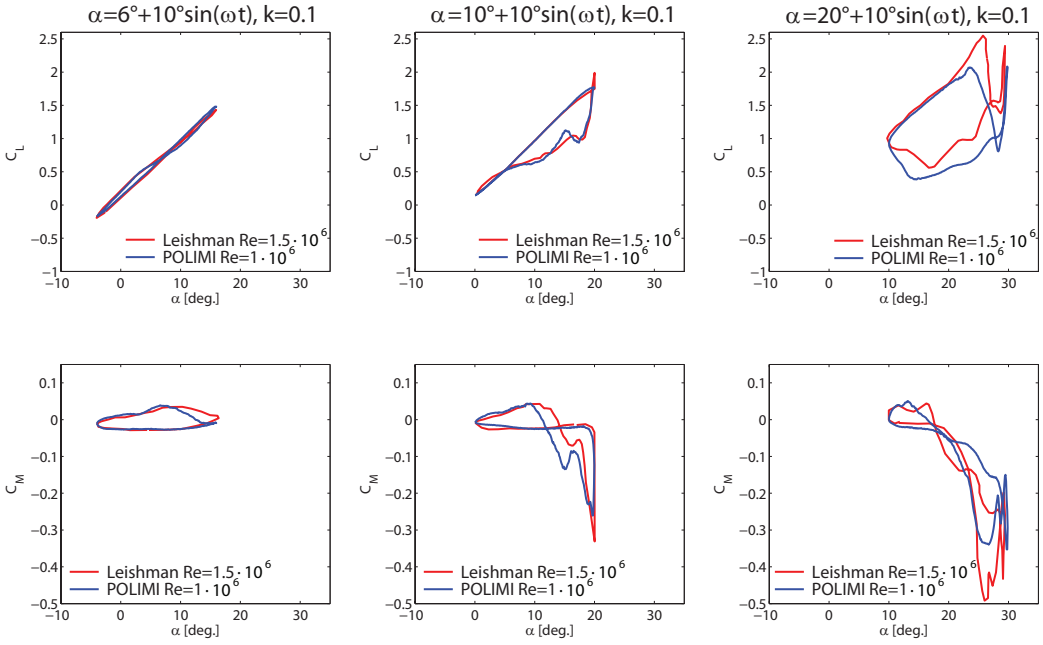

Figure 3.7: Comparison of the dynamic airloads curves for NACA 23012 at $Re = 1 \cdot 10^6$ with the curves measured in the work by Leishman [25].

3.1.3 Effect of oscillation amplitude

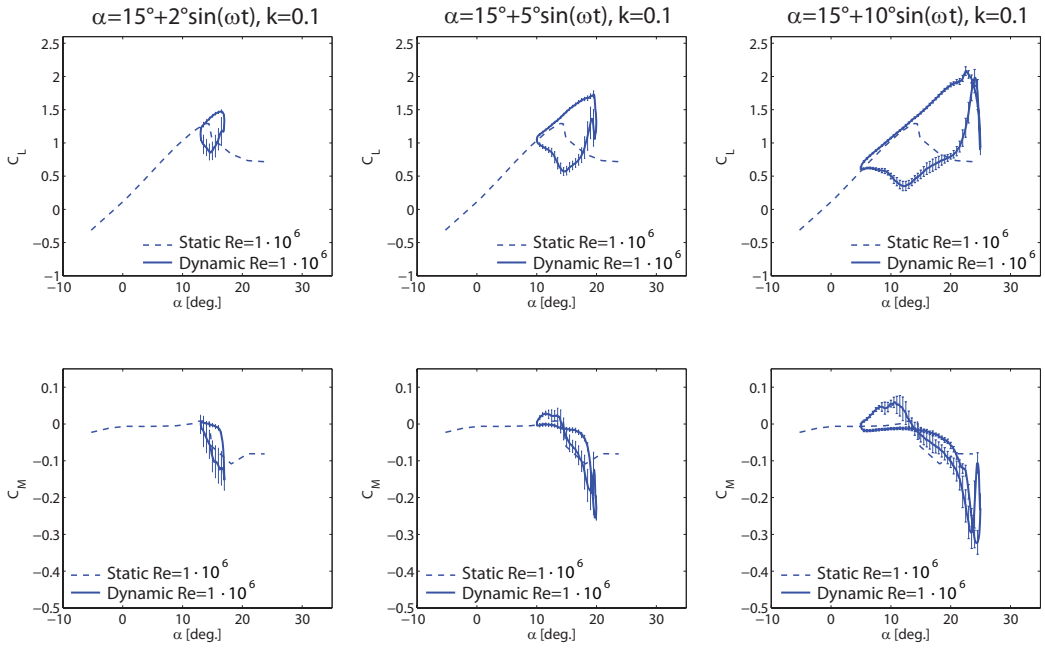

Figure 3.8: Effects of oscillation amplitude variations on lift and pitching moment curves for NACA 23012 at $Re = 1 \cdot 10^6$.

The effects of oscillation amplitude variations have been evaluated reproducing pitching cycles with α_0 in the interval between 2° and 10° with a constant mean angle of attack of 15° and a reduced frequency of 0.1. As can be seen from the tests results presented in Fig.3.8, the higher is the oscillation amplitude magnitude the more extended is the hysteresis area of the airloads curves. In fact, in these test conditions characterised by a constant mean angle of attack similar to the airfoil static stall angle, the flow topology during the motion of upstroke and downstroke is completely different, as during the upstroke motion the flow is attached to the airfoil, while during the whole downstroke motion the flow is fully separated and the reattachment does not occur until the upstroke motion restarts.

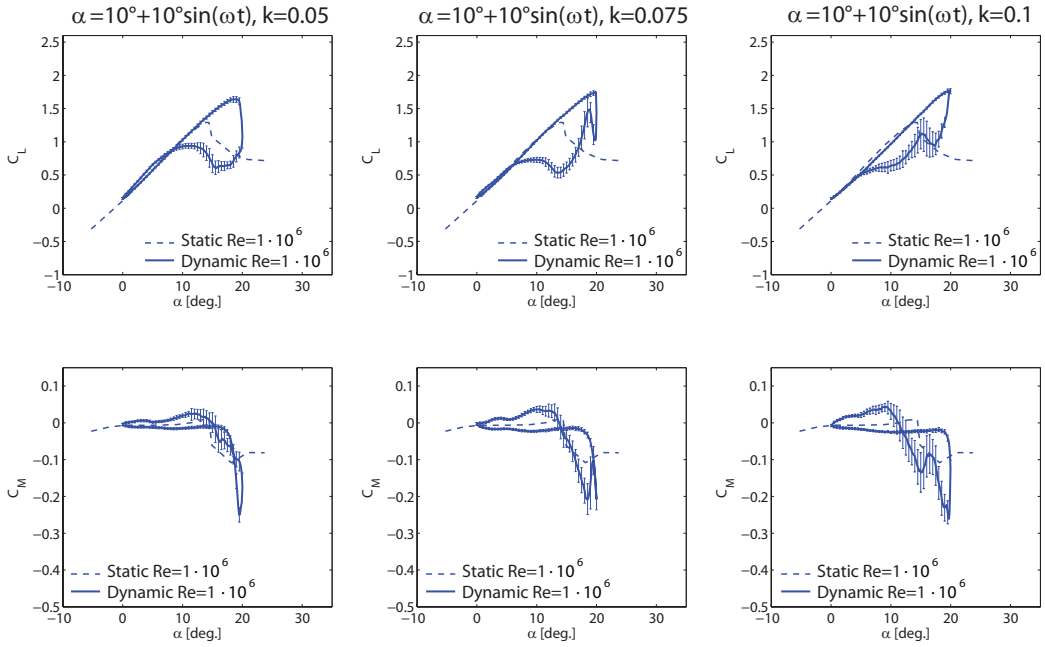

Figure 3.9: Effects of reduced frequency variations on lift and pitching moment curves for NACA 23012 at $Re = 1 \cdot 10^6$.

3.1.4 Effect of reduced frequency

The effects of reduced frequency variations have been evaluated reproducing pitching cycles with k in the interval between 0.05 and 0.1 with a constant mean angle of attack and oscillation amplitude of 10°. The tests results are presented in Fig.3.9. The effect of the reduced frequency increase is the delay of the onset of flow separation at a higher angle of attack, that produces a reduction of the airloads overshoots and hysteresis. This effect can be explained by the increase of a kinematic induced camber effect due to the rapid pitching motion of the airfoil, that decreases the pressure gradients over the chord for a certain lift value [5, 7]. Moreover, the increasing reduced frequency produces also the delay of the onset of secondary vortex formation. As can be observed from Fig.3.9, the $C_M - \alpha$ curves for the higher reduced frequencies tested present a clockwise loop with area greater than the counterclockwise loop; this condition, corresponding to a net negative aerodynamic torsional damping, could lead to the occurrence of the aeroelastic instability described in Sec.1.2 as *Stall Flutter* [6].

3.2 Higher order pitching motion

A higher order pitching motion overlaid to the sinusoidal motion of the airfoil is an interesting condition to test in order to evaluate the effects of the elasticity of the blades on the primary pitching motion at 1/rev. In particular, the following dual-sine pitching motion has been tested for the NACA 23012 airfoil to compare the measured airloads to the single-sine pitching motion law, similarly to the experiment of Gardner et al. [68]:

$$\alpha(t) = 15^\circ + 7^\circ sin(\omega t) - 1^\circ sin(5 \times (\omega t)) \tag{3.1}$$

at a reduced frequency $k = 0.1$ and $Re = 4 \cdot 10^5$. Figure 3.10 presents the shape of the tested dual-sine pitching law characterised by a 5/rev sinusoidal pitching motion with 1° amplitude subtracted to the 1/rev motion with 15° mean angle of attack (similar to the airfoil static stall angle of attack) and 7° amplitude.

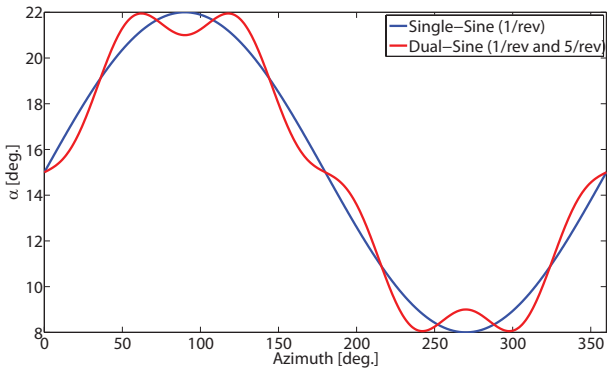

Figure 3.10: Comparison of the tested dual-sine higher order pitching motion and single-sine pitching motion.

As can be observed from Fig. 3.10, the two pitching motion laws share the same maximum and minimum angle of attack but present different shapes over a cycle.

Figure 3.11 presents the comparison of the measured lift and pitching motion coefficients for the single and dual sine pitching motion.
For the dual-sine case the separation and then the stall is delayed to a higher angle of attack respect to the single-sine case, as the angular velocity of the

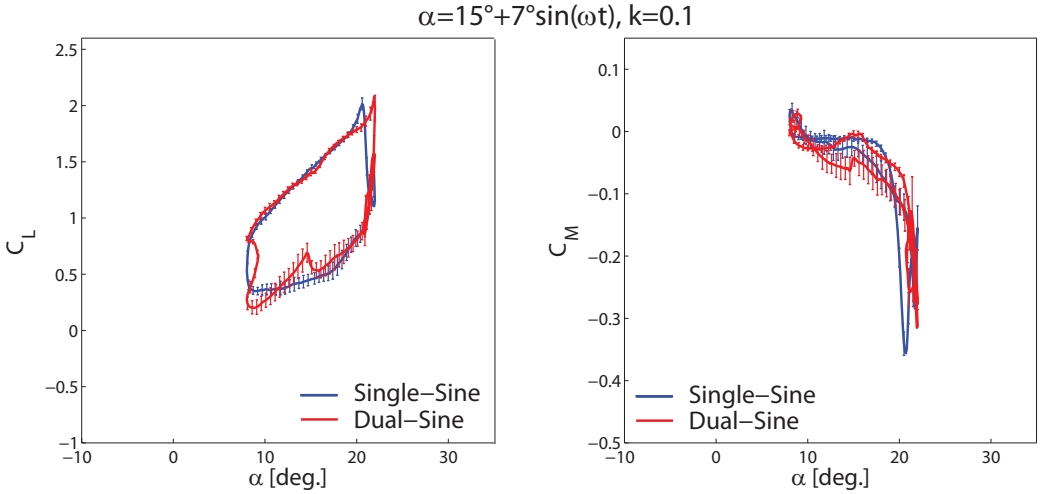

Figure 3.11: Comparison of airloads curves measured for NACA 23012 with single and dual-sine pitching motion at $Re = 4 \cdot 10^5$.

pitching airfoil in upstroke is higher around the separation angle of attack. This increases the kinematic effect of induced camber producing a further delay of the dynamic stall. The peak of the pitching moment coefficient occurs at the maximum angle of attack and presents about a 11% reduction respect to the single-sine case.

3.3 Comparison with numerical simulations

As mentioned earlier, one of the main goals of the experimental campaign on pitching airfoils is to obtain reliable data set to validate Computational Fluid Dynamics tools. A first step of this research activity, presented in this work, has been to evaluate modeling capabilities, comparing different numerical CFD models against the experimental results. The validation of reliable numerical models will be useful for the future phase of the activity consisting in the development and design of efficient control devices for dynamic stall alleviation. In this aim, within a PhD research activity at the Dipartimento di Ingegneria Aerospaziale of Politecnico di Milano, several two-dimensional numerical models have been built using **EDGE** [26], a Navier-Stokes solver developed at FOI, the Swedish Research Agency. Different turbulence models, such as the model by Hellsten [28, 29], and the $k - \omega$ SST by Menter

[27], have been tested, to assess their performances for these peculiar unsteady conditions.

3.3.1 CFD solver and numerical methodology

The **EDGE** code can be used to solve RANS (Reynolds Averaged Navier-Stokes) equations, DES (Detached-Eddy Simulation) and LES (Large Eddy simulation) for both two and three-dimensional problems with different flow conditions from laminar to fully turbulent.
The governing equations used for this activity has been the two-dimensional unsteady incompressible turbulent Navier-Stokes solved on structured grids using a node-centered finite volume technique. A blend of second and fourth order differences are chosen as artificial dissipation to eliminate the effect of oscillations in vicinity of shock waves or stagnation points. A dual time stepping method is applied for going ahead implicitly in time, in order to perform time accurate calculations. Before starting the unsteady computation, a steady state solution is used as an initial solution at the mean angle of attack of the pitching cycle.

Grid generation

The first grid geometry has a structured O-grid topology with 530×160 (84800) quadrilateral elements. As dynamic stall simulations show a considerable dependency on the quality of grid used, a second structured C-grid mesh with 1100×190 quadrilateral elements with a better resolution near the airfoil leading edge and trailing edge was used. This mesh presents a higher wall normal resolution using 40 highly stretched layers around the airfoil wall to enhance the velocity profile resolution within the boundary layer. Furthermore, the number of points in streamline direction is almost doubled compared to the O-grid mesh. For both the meshes, the wall-normal grid resolution of the closest internal node from the airfoil is of the order of $y+ = 1$. The location of the far-field is set to be at 20 chord length away from the airfoil to dispel the boundary reflections.
In Fig.3.12 and 3.13, a detailed view of the computational grids near the airfoil is shown. In the considered test cases, the whole grid performs a sinusoidal pitching motion as a rigid body.

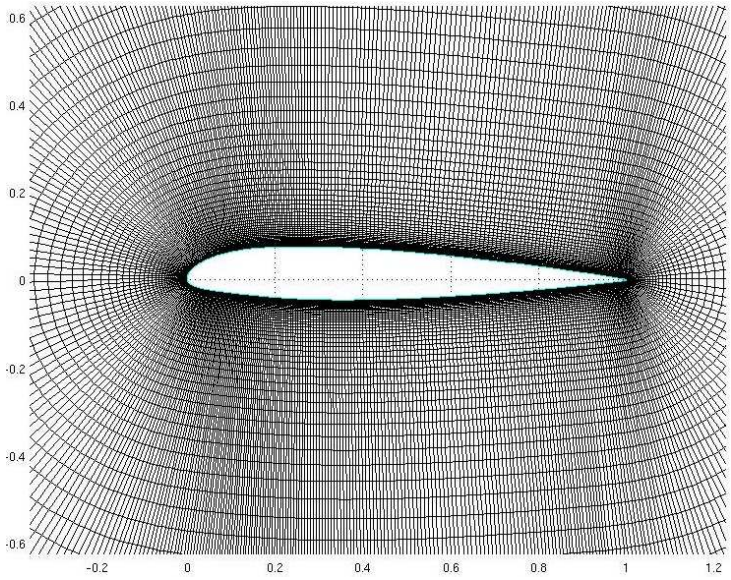

Figure 3.12: Detailed view of the used O-type grid.

Turbulence modeling

Turbulence models used for both test cases are Menter SST $k-\omega$ [27] and EARSM (Explicit Algebraic Reynolds Stress Model) by Wallin & Johansson coupled to Hellsten $k-\omega$ [28, 29]:

a) Menter SST $k-\omega$

The Menter SST $k-\omega$ is a two-equation turbulence model which is a blending of $k-\omega$ model inside the boundary layer and $k-\omega$ model away from the surface using a shifting function. This model is originally developed for aeronautics applications where the need for an accurate prediction of flows with pressure induced separation is substantially important. This model gives reasonable results both for attached and separated flows.

b). EARSM + Hellsten $k-\omega$

The Explicit Algebraic Reynolds Stress Model (EARSM) makes explicitly relation between Reynolds stresses and the mean flow field. Hence, in EARSM by Wallin & Johansson, Reynolds stress tensor is directly shown using the velocity gradient and the turbulence scales. The derivation of $k-\omega$ is based on the eddy-viscosity relation, whereas the principle of EARSM is expressed

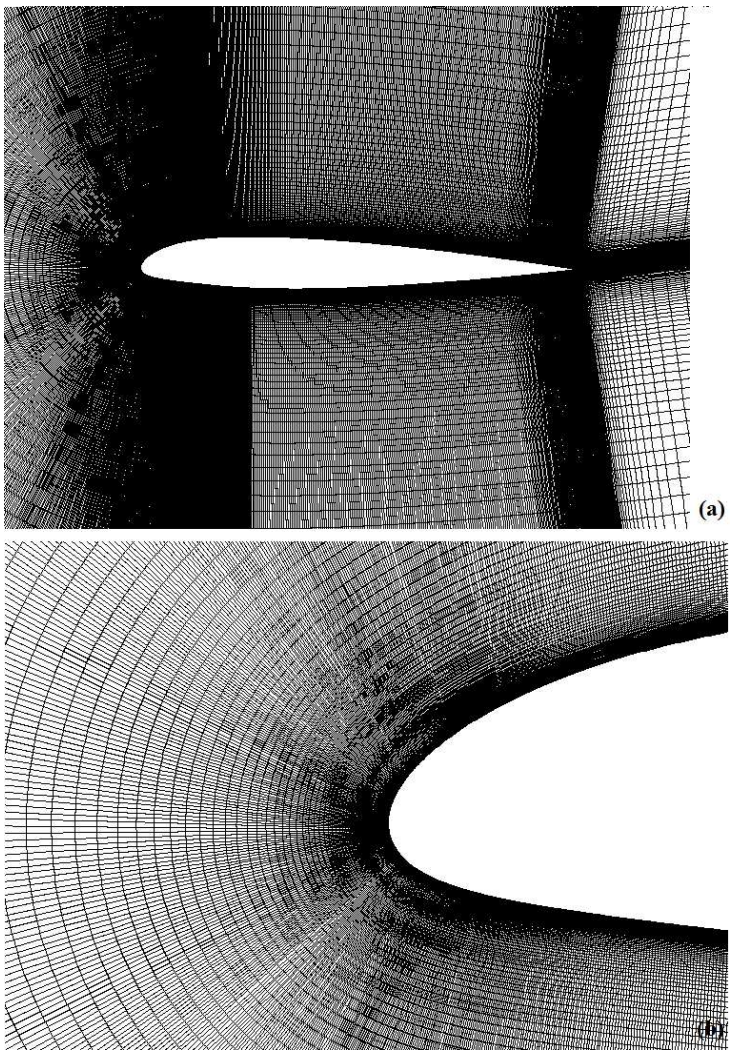

Figure 3.13: Detailed view of the used O-type grid: (a) close view of the airfoil; (b) close view of the leading edge.

using Reynolds Stress models. Hence, a new $k-\omega$ model presented by Hellsten which is in a good compatibility with EARSM, have been used in this work. The ω equation is calibrated fully consistently with EARSM model. Therefore, this model shows better accuracy compared to the classical two-equation models.

3.3.2 Comparison of the results

The test cases considered in this work are two pitching cycles characterised respectively by 10° and 15° mean angle of attack, 10° amplitude and reduced frequency $k = 0.1$. The numerical simulations for the O-grid model have been carried out at $Re = 1 \cdot 10^6$. Figure 3.14 presents the comparison of the measured airloads curves with the results of the simulations carried out with Hellsten and Menter $k - \omega$ turbulence models for the O-grid mesh.

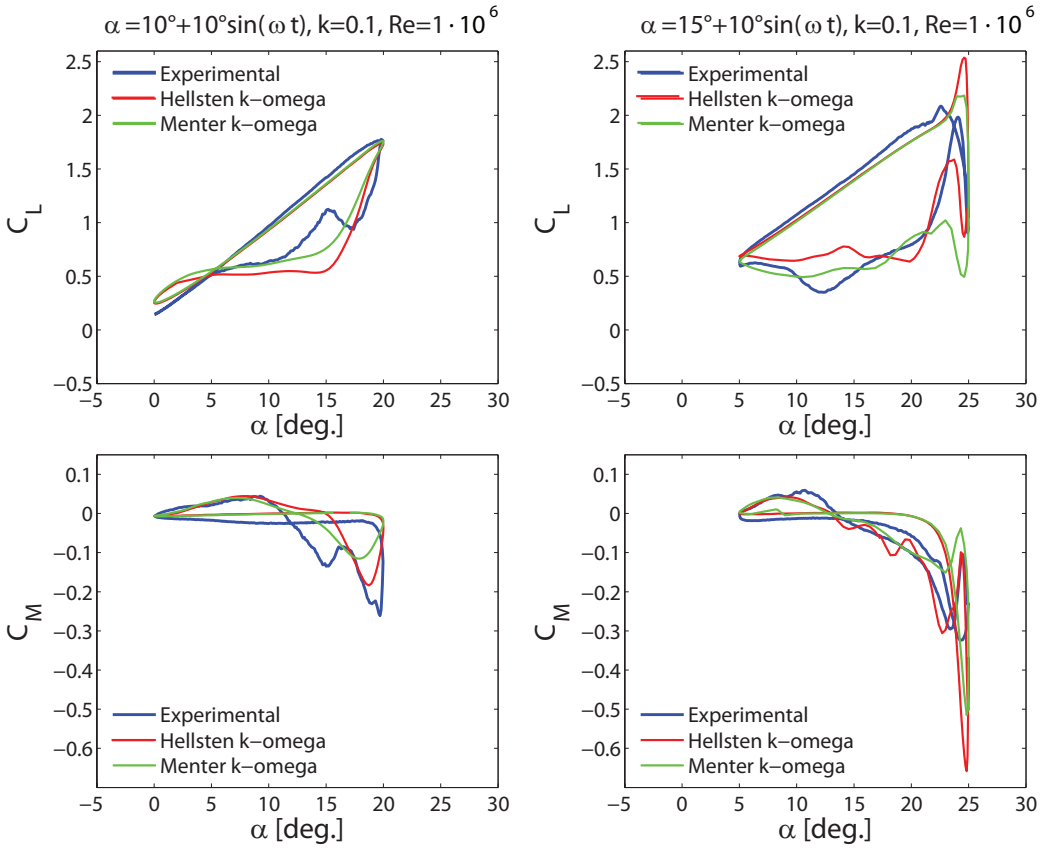

Figure 3.14: Comparison of experimental and numerical results for O-grid mesh.

For the pitching cycle case with 10° of mean angle of attack, the numerical results, for both the turbulence models, are in good correlation during the upstroke motion but do not reproduce the increase of lift and pitching moment that is observed in the experimental curves during the downstroke

motion for angle of attack between 18° and 14°. This behavior could be explained by the fact that in this range of angles the numerical model with a low resolution grid is not capable to reproduce the formation and migration over the airfoil upper surface of the vortex typical of the phenomenon.
For the pitching cycle case with 15° of mean angle of attack, the numerical results, for both the turbulence models, present a delay respect to the experimental curve of the non-linear increase of lift in upstroke due to the formation and migration of the DSV. Moreover, the numerical curves present a peak of lift and pitching moment during the cycle greater than the measured ones.
The simulations with the finer C-grid have been focused at the moment on the test condition with mean angle of attack equal to 10° but at a lower Reynolds number $Re = 6 \cdot 10^5$. Figure 3.15 presents the comparison of the measured airloads curves with the results of the simulations carried out with Hellsten $k - \omega$ turbulence model for the C-grid mesh.

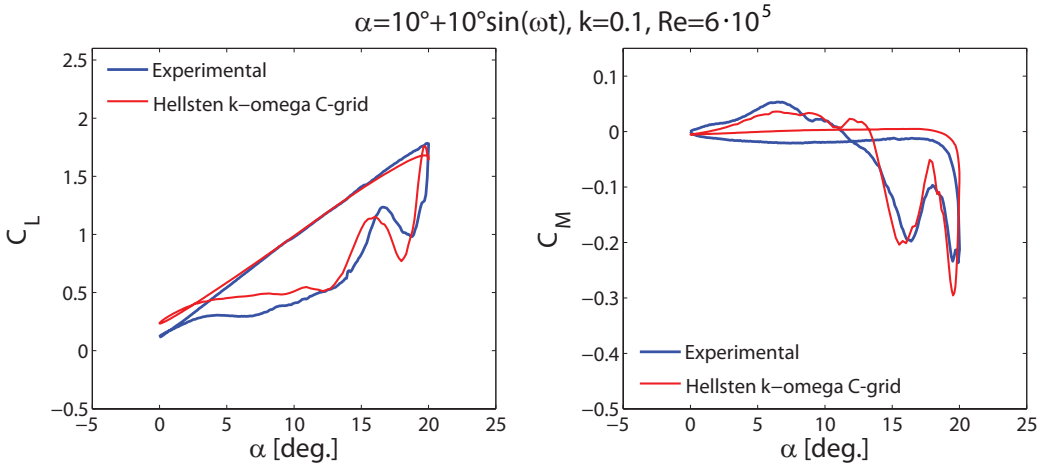

Figure 3.15: Comparison of experimental and numerical results for C-grid mesh.

The numerical results obtained with the finer C-grid mesh present a very good agreement with the experimental results. In fact, for the downstroke motion the numerical model captures the secondary increase of the airloads with a very small delay in terms of angle of attack.
The current research activity is going on with the investigation of diverse dynamic stall conditions using more advanced numerical techniques, such as

the Detached Eddy Simulation or the Large Eddy Simulation, to verify the capabilities of a more accurate numerical model. Moreover, the numerical research activity is going to verify the three-dimensional effects by means of the comparison between experimental results and the results of simulations carried out with a three-dimensional model reproducing exactly the experiment in the wind tunnel.

3.4 PIV flow surveys

This section presents the results of the PIV flow surveys carried out above the upper surface of the pitching NACA 23012 airfoil in dynamic stall condition. In particular, two interesting pitching motion conditions have been selected corresponding to deep dynamic stall:

$$\alpha(t) = \alpha_M + 10^\circ sin(\omega t) \tag{3.2}$$

with $\alpha_M = 10^\circ$ or 15° and a reduced frequency $k = 0.1$. The wind tunnel velocity has been limited to 30 m/s corresponding to $Re = 6 \cdot 10^5$ as the long run time required by the present measurement would produce, at higher velocity, a too long highly stressing load cycle on the model strut.
The main goal of the PIV flow surveys was to describe the detail of the flow physics that characterise the NACA 23012 dynamic stall process. For the present test campaign, the multigrid technique [38] has been employed to correlate the image pairs, starting from an interrogation window of 96×96 pixels to a 32×32 pixels window. In order to filter out the effect of turbulent oscillations, the velocity flow fields have been phase averaged over 40 image pairs for each measurement window. In the following figures the measured velocity fields are presented by the instantaneous streamlines. Some information about the boundary layer are lost specially near the airfoil leading edge, due to laser sheet reflection on the aluminium midspan section.
In order to point out the differences between the flow fields in steady and dynamic conditions, a preliminary steady PIV survey has been carried out with the airfoil at $\alpha = 18^\circ$ corresponding to a post-stall condition. Figure 3.16 presents the comparison between the flow fields measured at $\alpha = 18^\circ$ in the steady case and in the dynamic condition described by Eq.3.2 with 15° of mean angle of attack in upstroke motion.

The steady case at $\alpha = 18^\circ$, see Fig. 3.16(a), presents a completely separated flow starting from the airfoil leading edge, while in dynamic condition

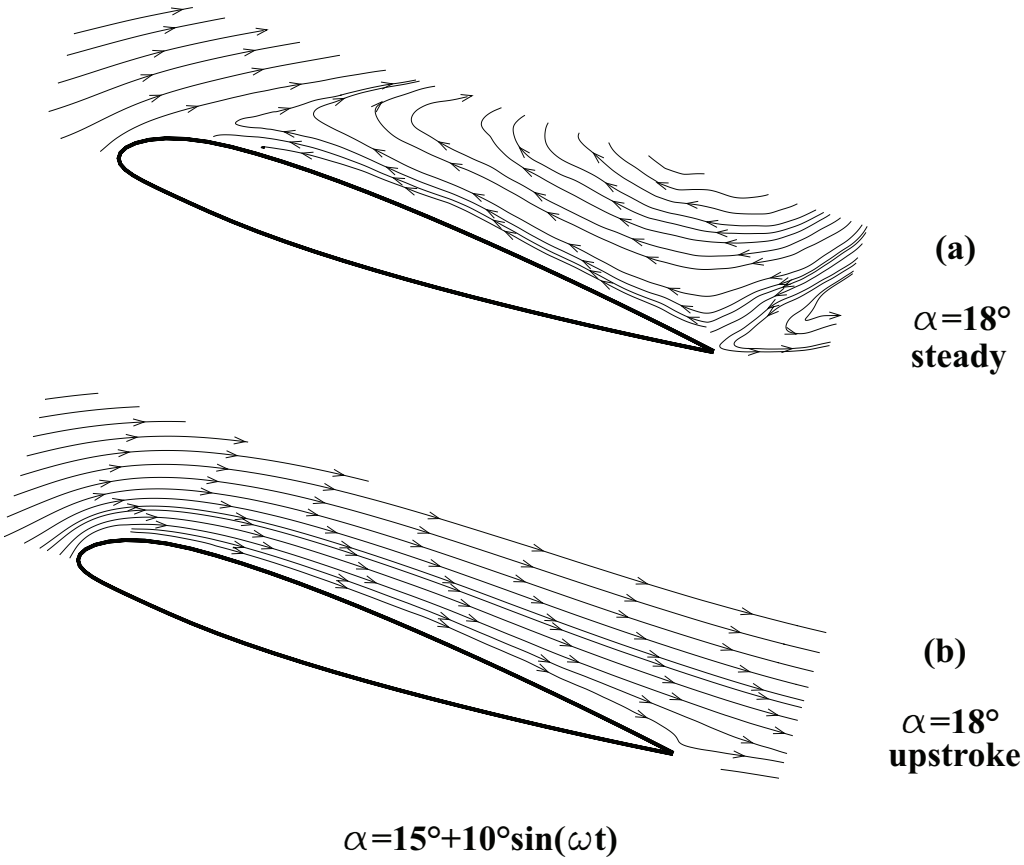

Figure 3.16: Comparison of a steady and dynamic PIV flow survey for NACA 23012 at $\alpha = 18°$ and $Re = 6 \cdot 10^5$.

at the same incidence in upstroke the flow is fully attached (see Fig. 3.16(b)), as the stall is delayed at a higher incidence by the effect of the rapid positive pitching rate. The analysis of these flow fields validates the measurement technique and the set up.

3.4.1 $\alpha(t) = 10° + 10° sin(\omega t)$

The dynamic condition in the title has been the object of a complete survey that allowed to describe the flow physics over all the pitching cycle. Figure

3.17 presents a series of pictures illustrating the flow field measured at different angles of attack, both in upstroke and downstroke. In order to better comprehend the different stages of the dynamic stall process, all the flow fields are presented together with the airloads curves measured for the same dynamic condition, with a red spot in correspondence of the illustrated flow field angle of attack.
The flow on the upper surface of the airfoil is attached for almost all the upstroke motion, in particular from $\alpha = 0°$ to $\alpha = 18°$, where also the lift coefficient increases linearly (see Fig. 3.17(a) to 3.17(f)). At $\alpha = 19°$ the flow separation starts at the airfoil trailing edge with the formation of a small vortical structure (see Fig. 3.17(g)) that grows towards the leading edge as the airfoil reaches the maximum angle of attack at $\alpha = 20°$ (see Fig. 3.17(h)); the formation of the vortical structure produces the peak of lift and nose-down pitching moment coefficients.
During almost the whole downstroke motion the flow presents a wide separation and is characterised by the formation and migration of strong vortical structures, as for instance at $\alpha = 16°$ (see Fig. 3.17(m)). This issue produces the increase of lift and pitching moment observed in the experimental airloads curves between 18° and 14° angle of attack. The flow reattachment occurs only at a very small angle of attack in downstroke near to $\alpha = 4°$, as can be observed from Fig. 3.17(p). The different behavior of the flow topology during the motion of upstroke and downstroke explains the asymmetry of the airloads with respect to the motion of the body that produces a large amount of airloads hysteresis.

3.4.2 $\alpha(t) = 15° + 10° sin(\omega t)$

The flow field survey carried out for the dynamic condition described in the title above illustrates the main feature of the deep dynamic stall regime, consisting in the formation and migration above the airfoil upper surface of the dynamic stall vortex (**DSV**) that occurs in the last part of the upstroke motion. In fact, this phenomenon can be observed from the flow field pictures series corresponding to the higher angles of attack in upstroke presented in Fig. 3.18.
As observed for the previous dynamic condition, at $\alpha = 18°$ the flow is fully attached to the airfoil upper surface; in particular, the lift coefficient is about 50% higher than the static stall value (see Fig. 3.18(a)). At $\alpha = 20°$ a thin layer of reversed flow starts at the airfoil trailing edge (see Fig. 3.18(b)) and

produces the formation of the characteristic vortical structure as the angle of attack increases (see Fig. 3.18(c)). The change of pressure distribution produces a non-linear increase of the lift coefficient curve and the break of the nose-down pitching moment that starts to increase rapidly as the **DSV** moves on the airfoil upper surface.
As can be observed from Fig. 3.18)(d), the dynamic stall vortex characterised by a clockwise rotation reaches the airfoil midchord at $\alpha = 23°$ where the lift and of the nose-down pitching moment coefficients present the maximum peak. At the higher angle of attack of $\alpha = 24°$, the vortex grows, moves downstream (see Fig. 3.18(e)) and detaches from the trailing edge; the shedding of the **DSV** produces the lift stall, delayed respect to the pitching moment stall and consequently the airloads experiences large and rapid variations. At the maximum angle of attack in upstroke, $\alpha = 25°$, where the airfoil reverses the pitching motion (see Fig. 3.18(f)), the **DSV** is completely detached from the airfoil and the flow on the upper surface is fully detached.

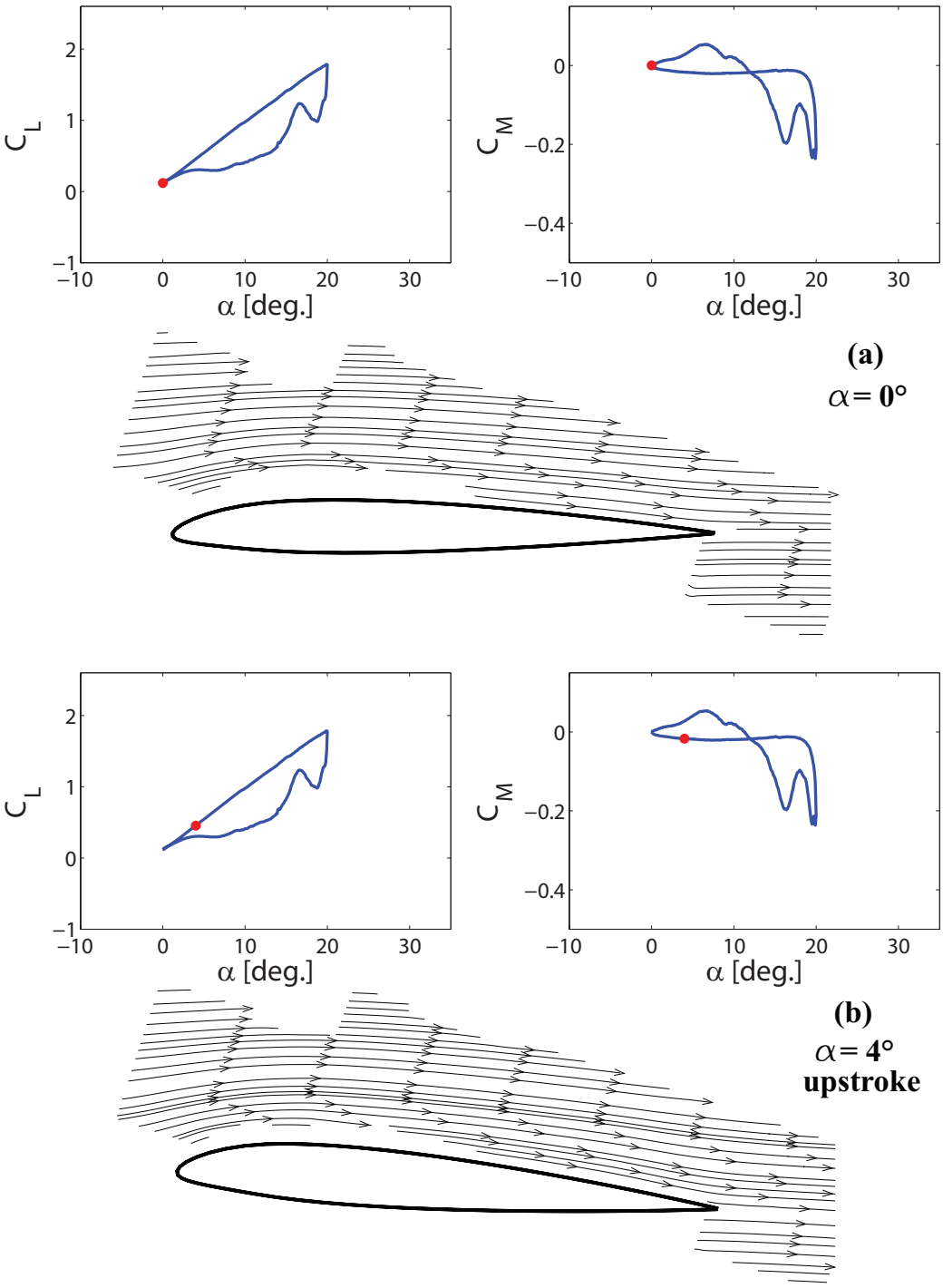
C_L
α [deg.]
C_M
α [deg.]
(a)
α = 0°
C_L
α [deg.]
C_M
α [deg.]
(b)
α = 4°
upstroke

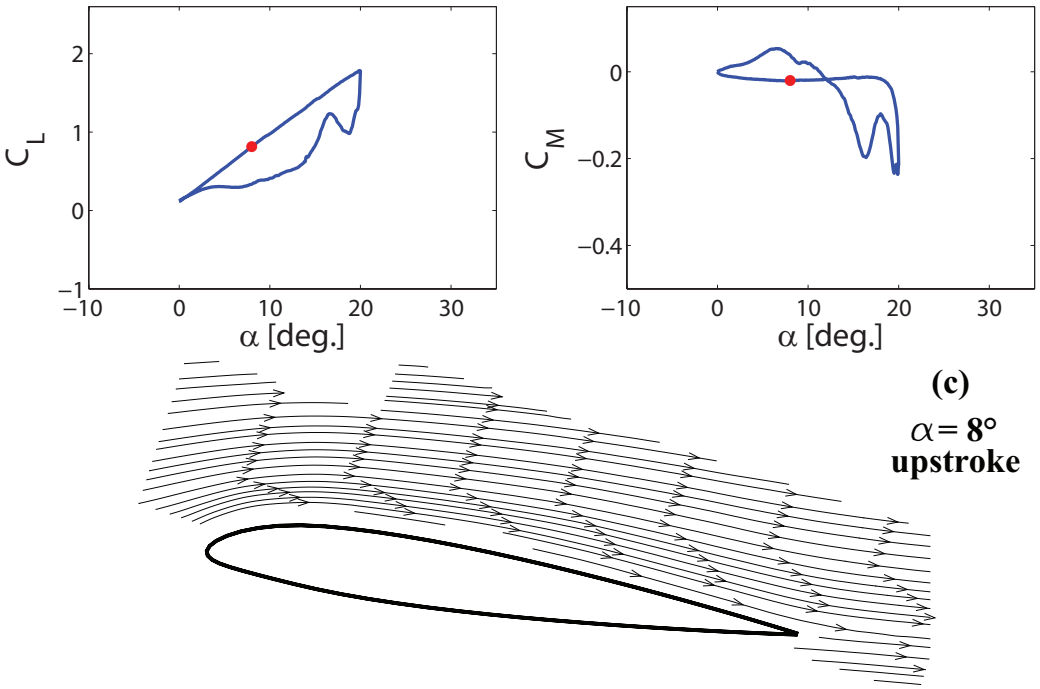
C_L
α [deg.]
C_M
α [deg.]
(c)
α = 8°
upstroke

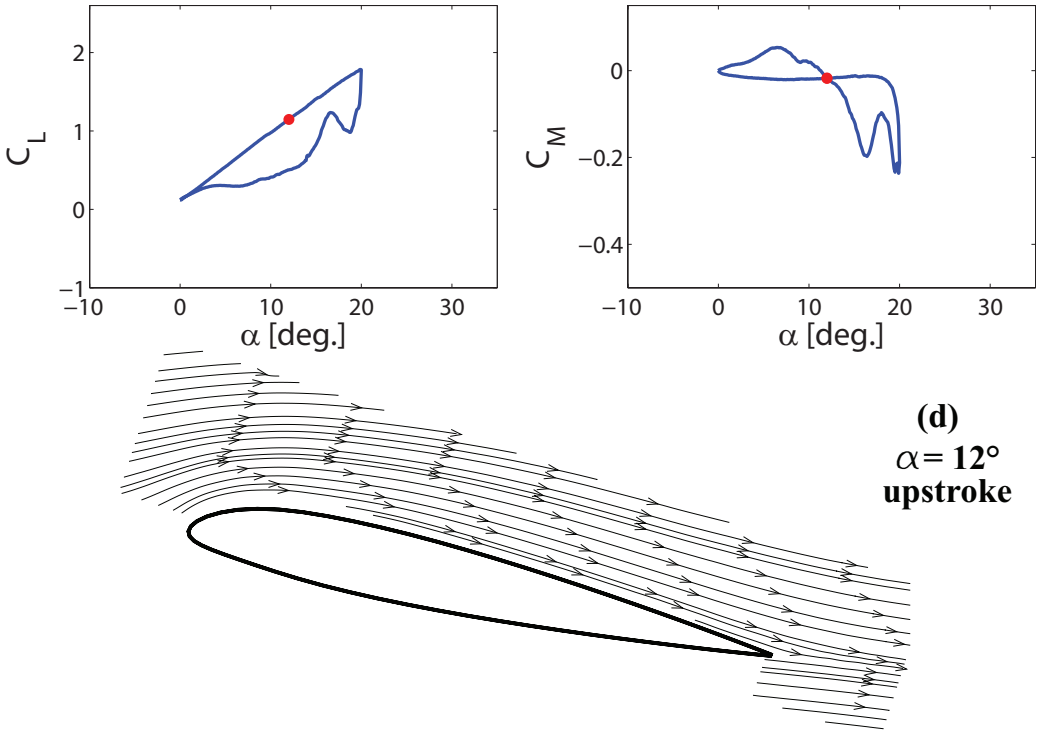
C_L
α [deg.]
C_M
α [deg.]
(d)
α = 12°
upstroke

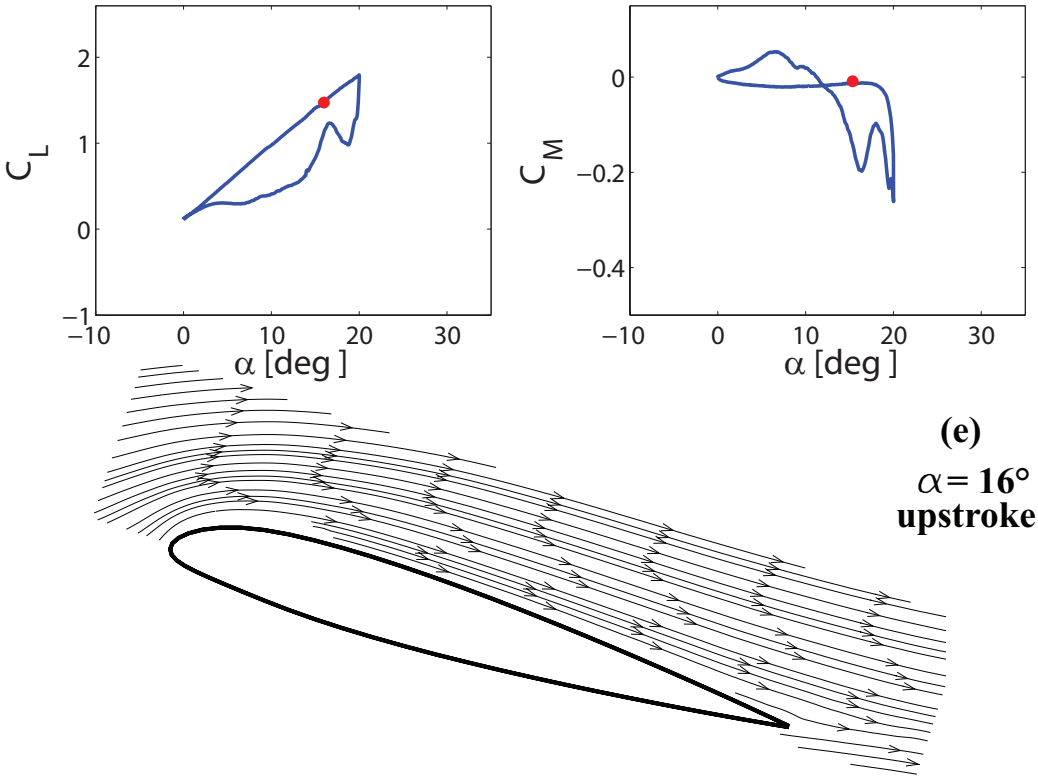

(e)
$\alpha = 16°$
upstroke

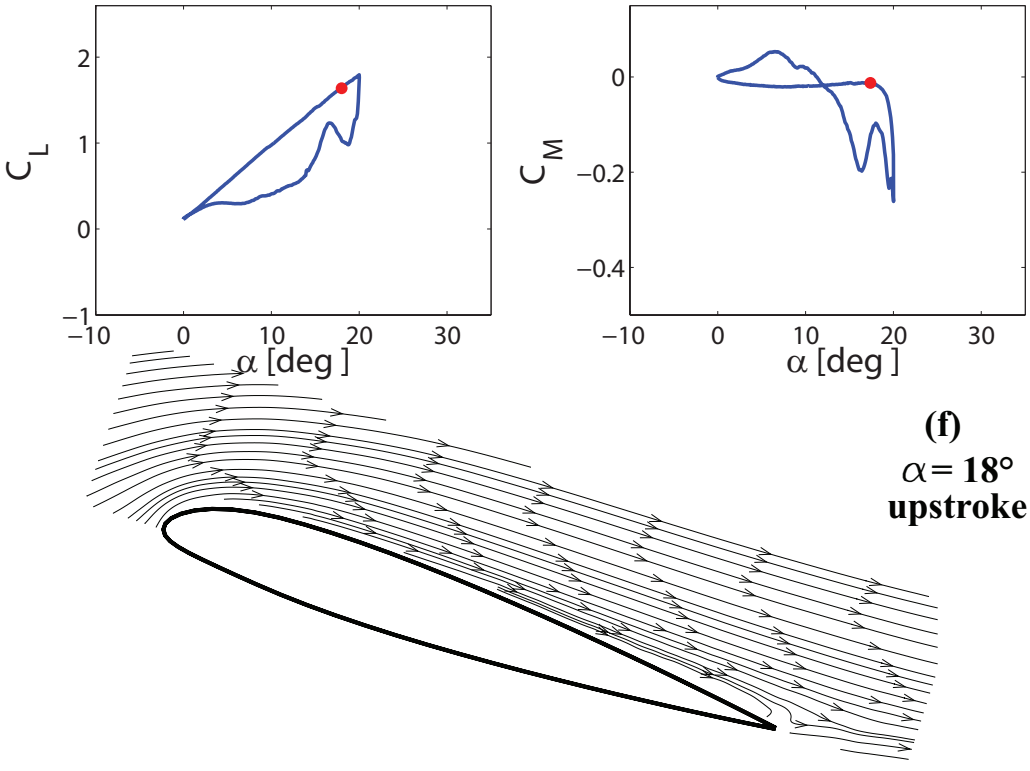

(f)
$\alpha = 18°$
upstroke

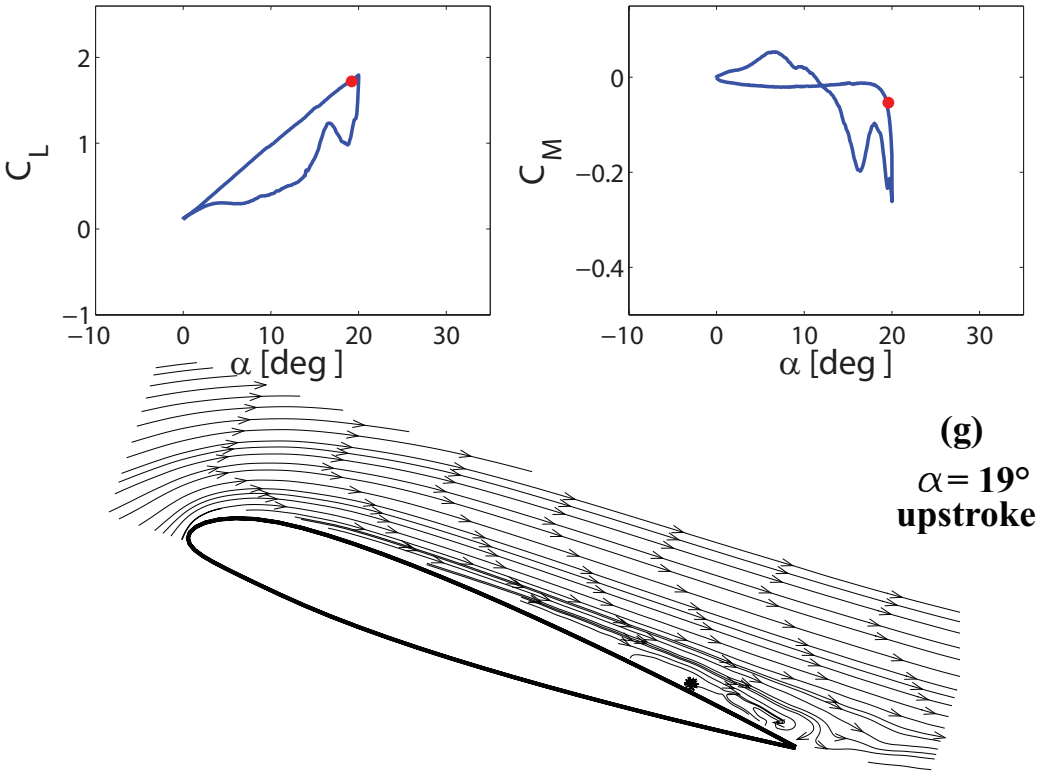

(g)
$\alpha = 19°$
upstroke

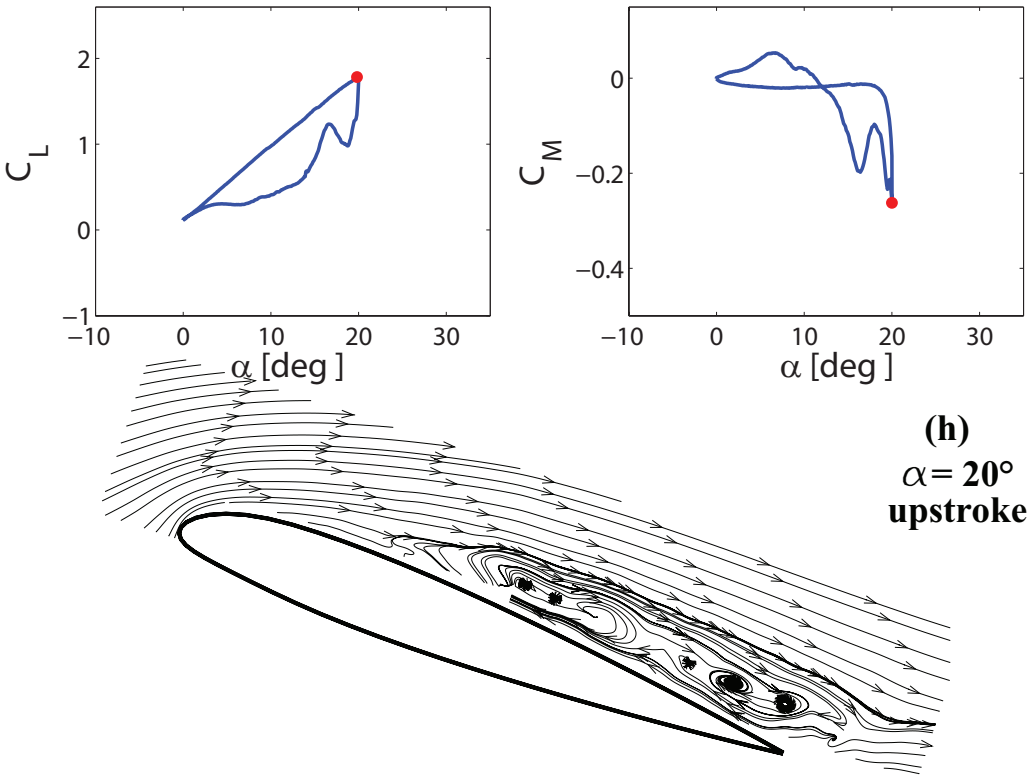

(h)
$\alpha = 20°$
upstroke

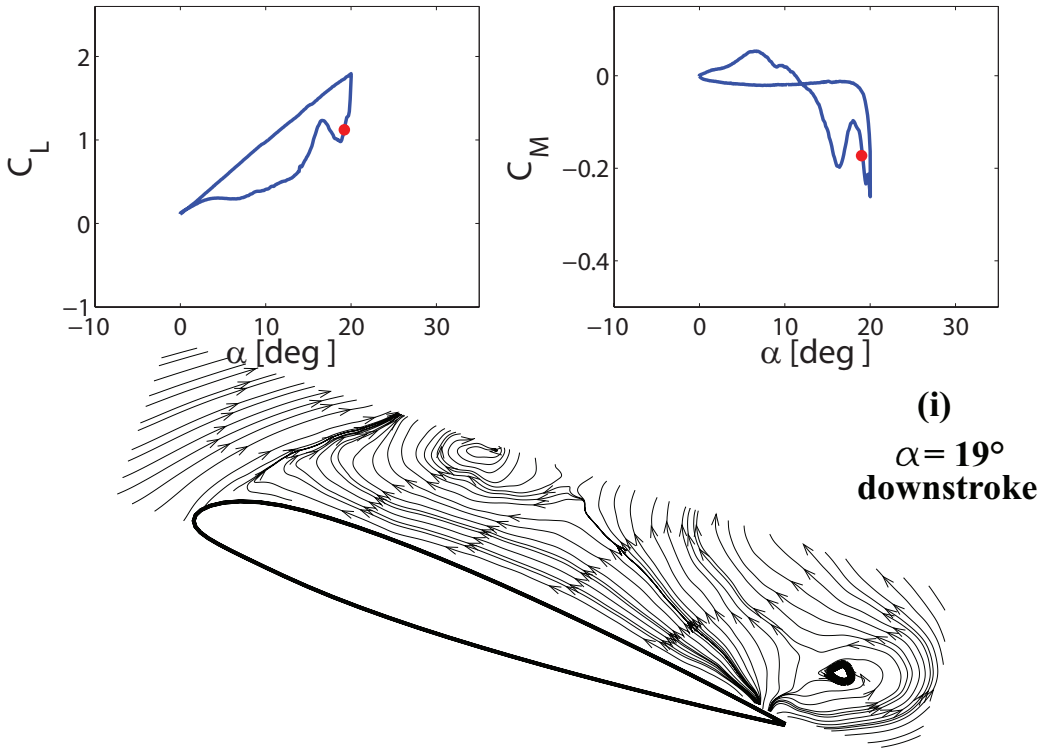
C_L
C_M
α [deg]
(i)
α = 19°
downstroke

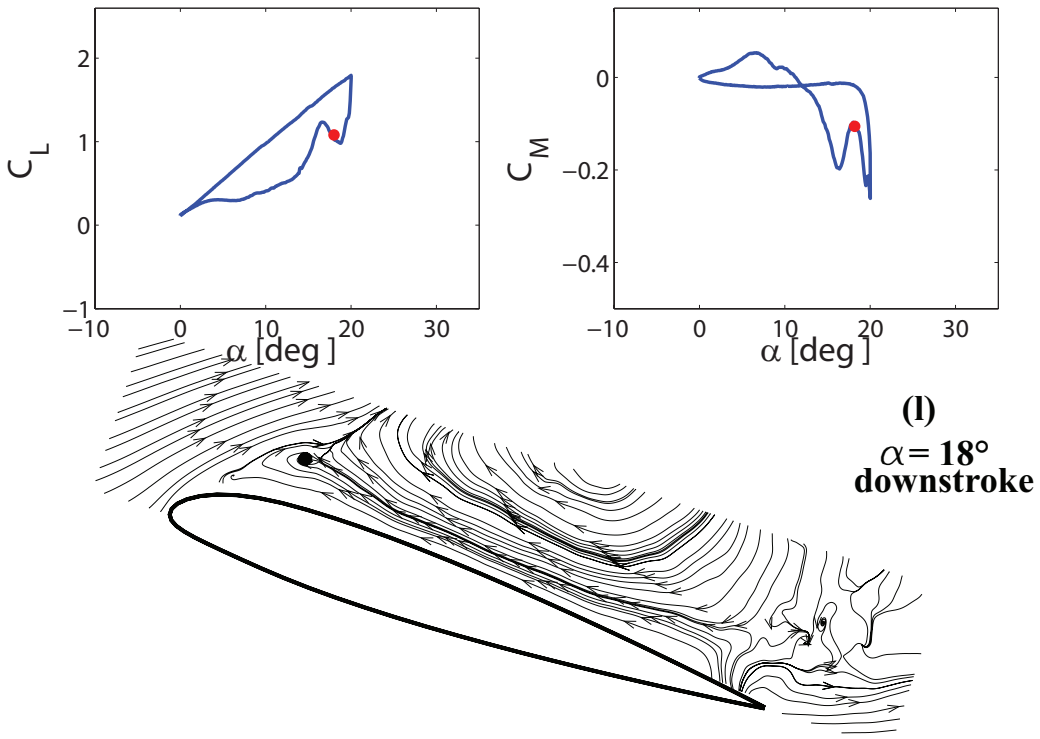
C_L
C_M
α [deg]
(l)
α = 18°
downstroke

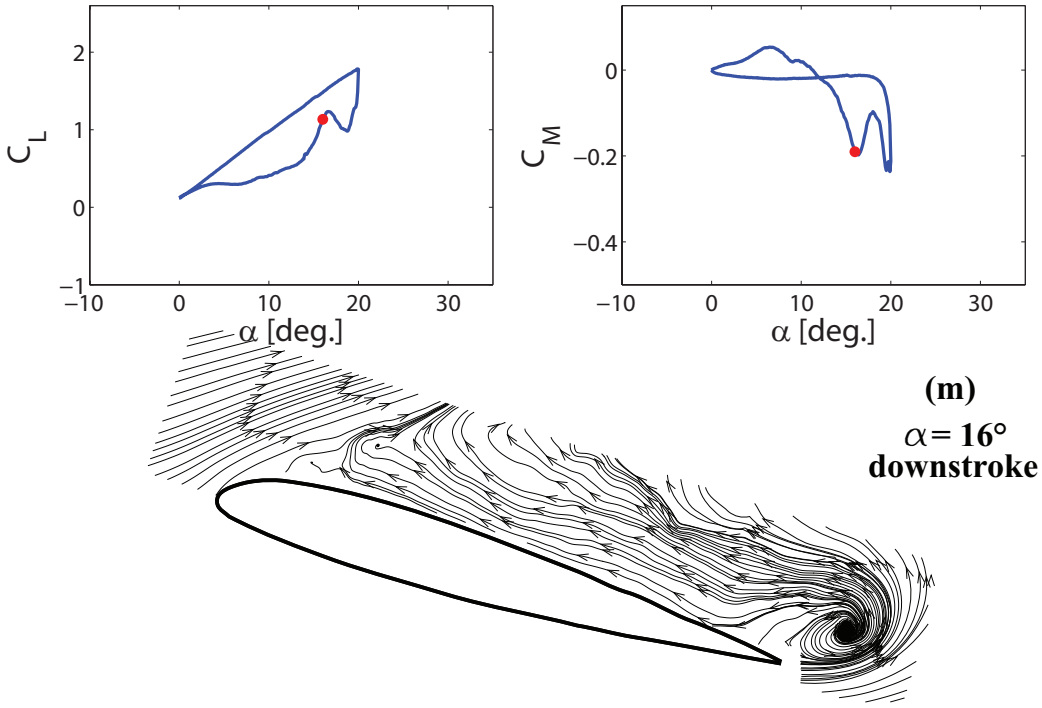
C_L
C_M
α [deg.]
α [deg.]
(m)
α= 16°
downstroke

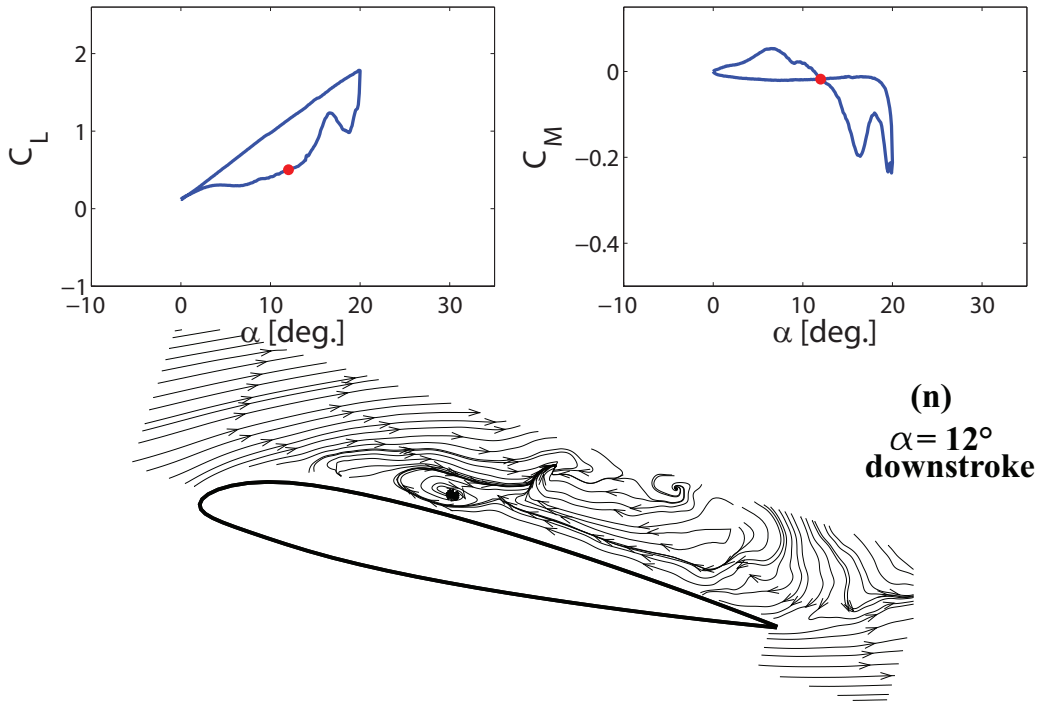
C_L
C_M
α [deg.]
α [deg.]
(n)
α= 12°
downstroke

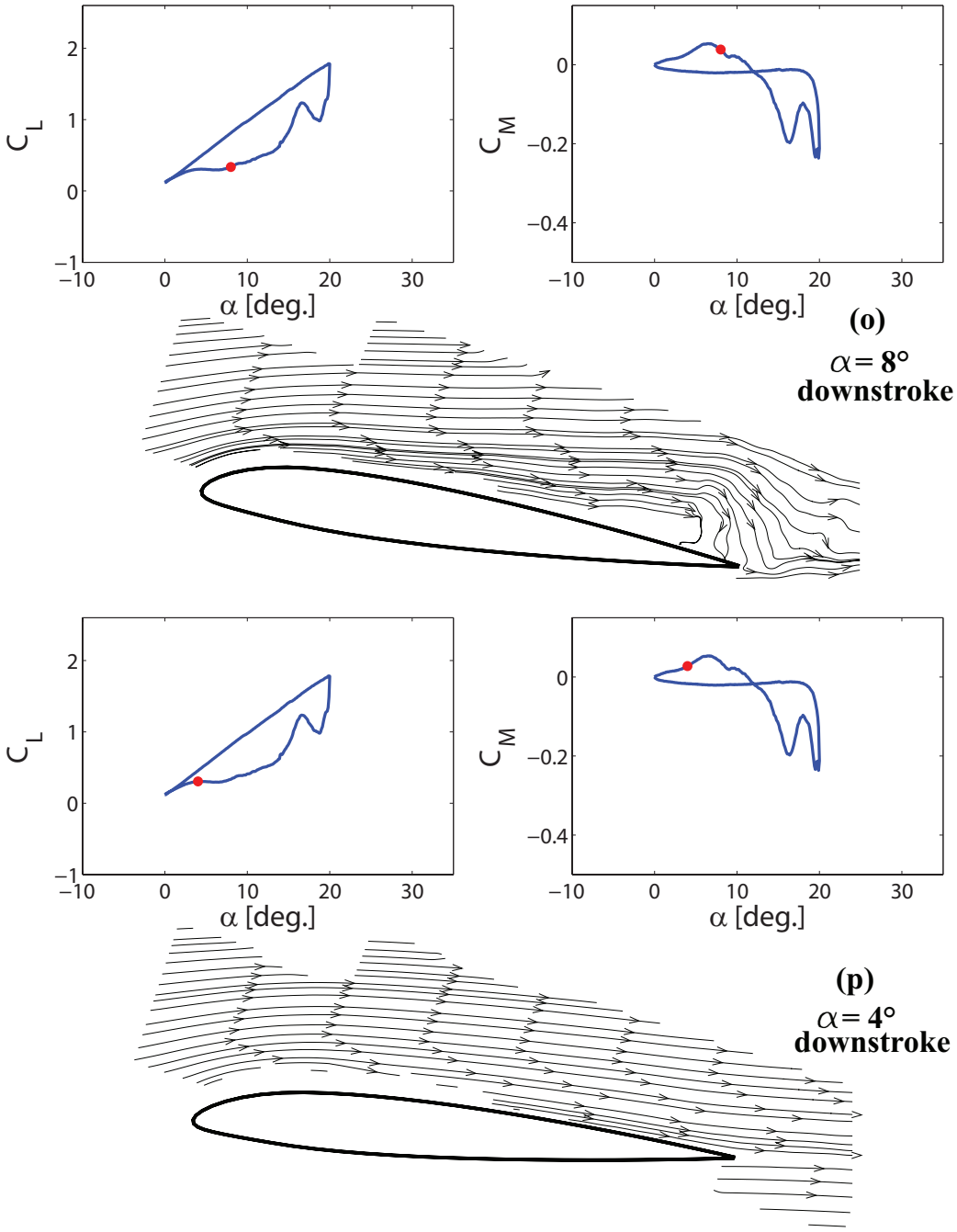

Figure 3.17: NACA 23012 PIV flow surveys for $\alpha(t) = 10° + 10°sin(\omega t)$ at $Re = 6 \cdot 10^5$ in Deep Dynamic Stall condition.

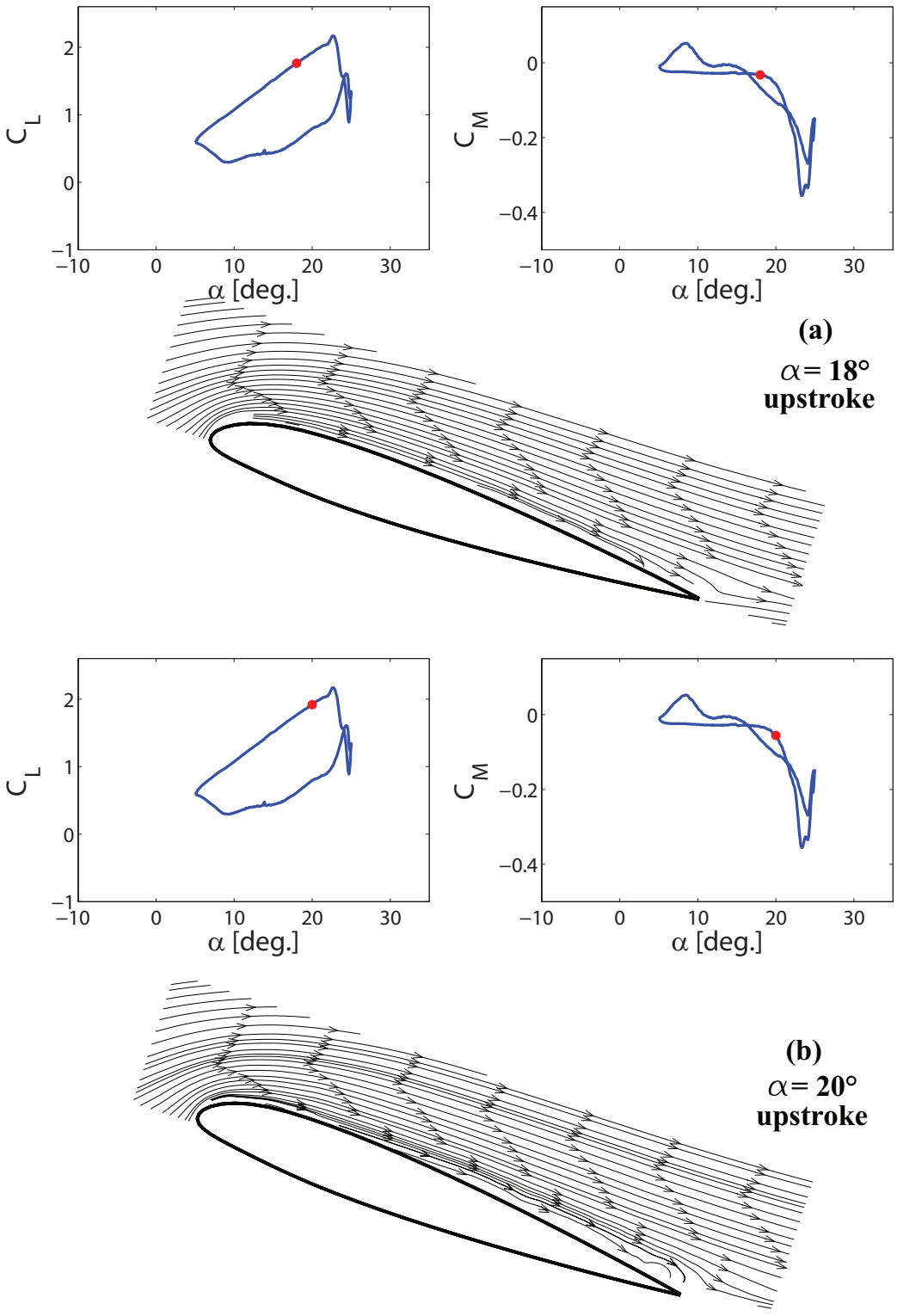
C_L
α [deg.]
C_M
α [deg.]
(a)
α= 18°
upstroke
C_L
α [deg.]
C_M
α [deg.]
(b)
α= 20°
upstroke

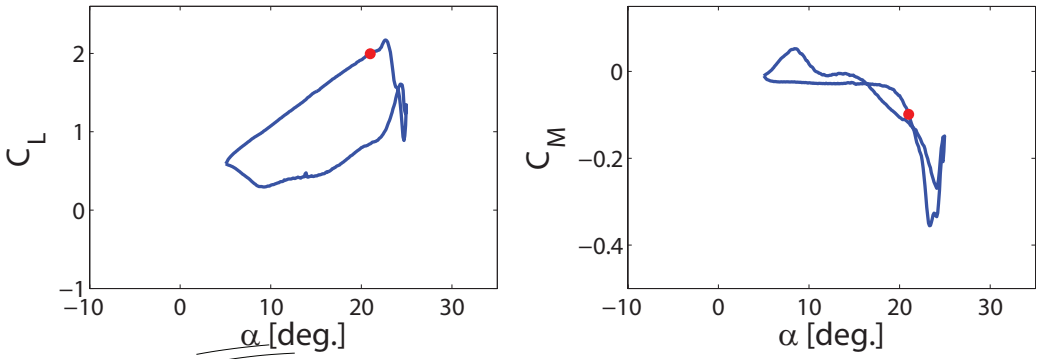

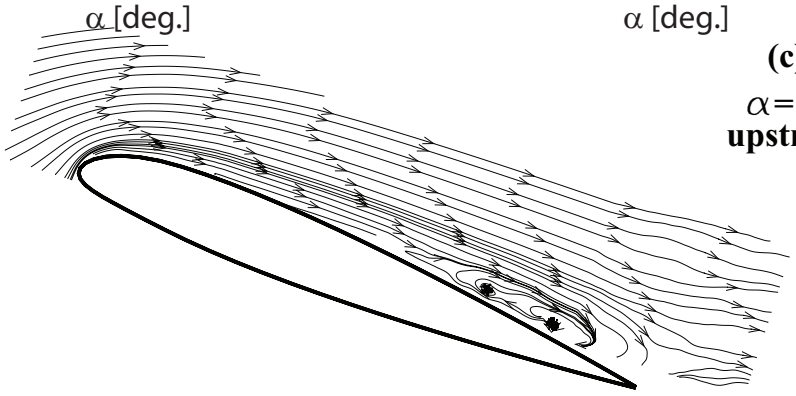

(c)
$\alpha = 21°$
upstroke

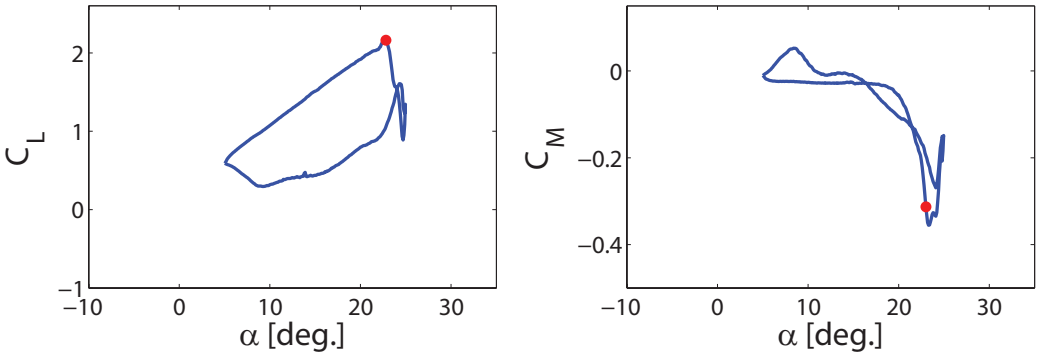

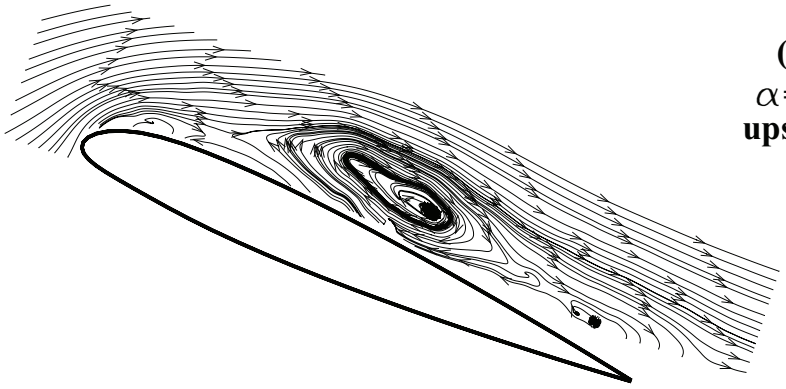

(d)
$\alpha = 23°$
upstroke

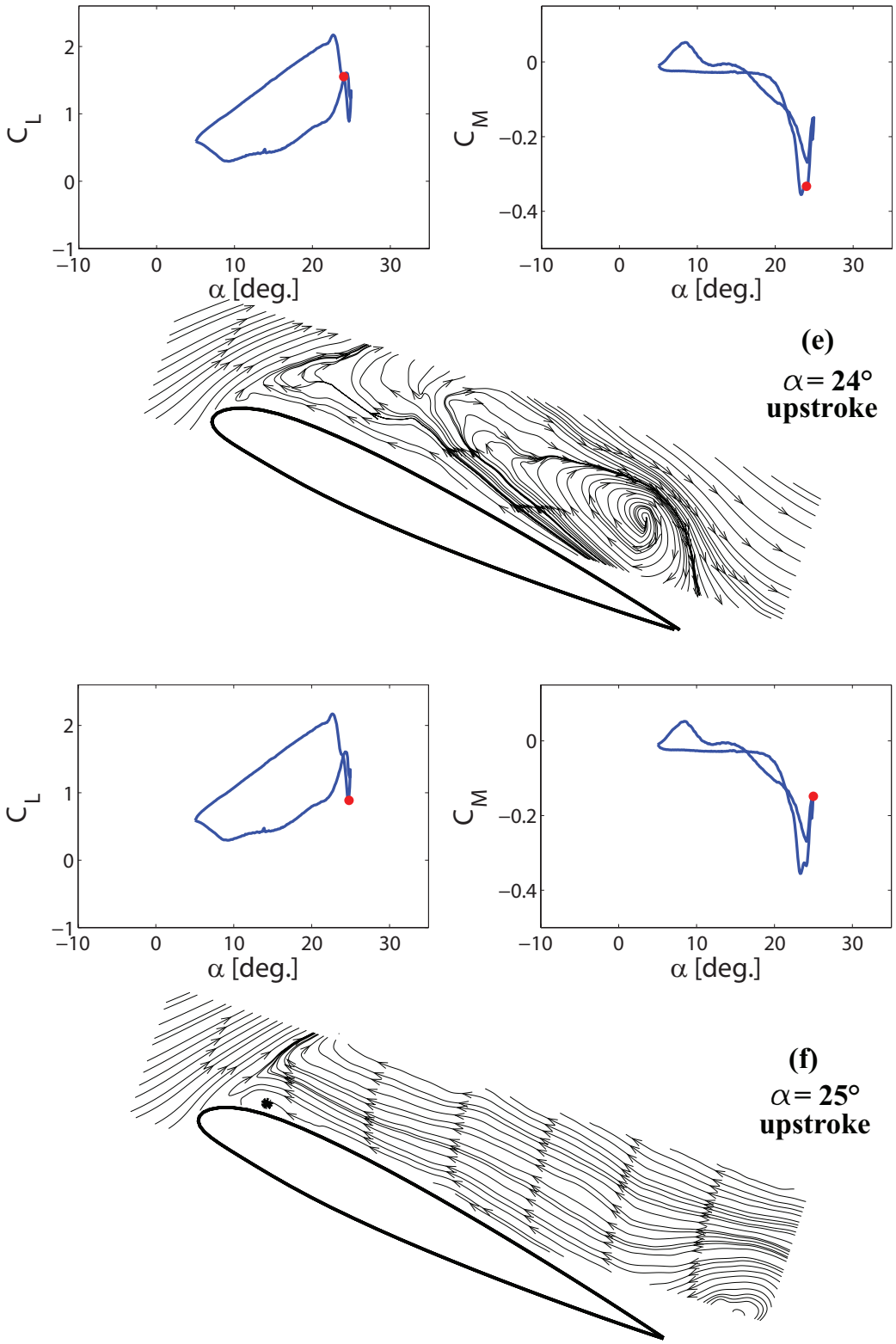

Figure 3.18: NACA 23012 PIV flow surveys for $\alpha(t) = 15° + 10° sin(\omega t)$ at $Re = 6 \cdot 10^5$ in Deep Dynamic Stall condition.

Chapter 4

Dynamic Stall control

The onset of the dynamic stall phenomenon on rotor blades produces a series of negative effects on helicopters performance as described in Sec.1.1. For this reason, the dynamic stall control is one of the more challenging research topic in rotorcraft aerodynamics and aeroelasticity field. In fact, recently, the design and tests of new active and passive control systems to alleviate the detrimental effect of the dynamic stall phenomenon have been the subject of many numerical and experimental works. The main goals proposed by the dynamic stall control devices are fundamentally the reduction of the loads acting on the pitch links and the increase of the helicopter forward speed and maneuver capability.
The experimental activity carried out on the NACA 23012 pitching airfoil enabled to validate the new experimental apparatus and the measurement techniques involved, as well as to evaluate the performance of the airfoil section in dynamic stall conditions. After the experimental activity on the clean blade section, the focus of the work has become the evaluation of the possible benefits gained through the use of passive trailing edge flaps integrated on the model blade section. In this aim, the trailing edge flaps have been tested both on the NACA 23012 and on the thicker NACA 23015 blade section model, in order to verify their effects on two airfoil characterised respectively by a leading edge and a trailing edge stall process.
Before the description of the experimental campaign about the use of passive control devices, a brief overview of the recent works about active control systems for dynamic stall alleviation is presented in the next section, in order to quantify and compare their performances.

4.1 Overview of Dynamic Stall active control

In the recent literature several numerical and experimental works on two-dimensional pitching blade sections analysed the effectiveness of active control systems for dynamic stall alleviation. In particular, the research activity focuses the attention on the active periodic modification of the airfoil shape during a blade pitching cycle, in order to delay the onset of the dynamic stall introducing an appropriate variation of the pressure field around the airfoil. As an example, sophisticated mechanism integrated in the blade section have been designed for dynamically deforming the leading edge airfoil shape by means of an active variable droop [39]. The active rotation of a 25% chord variable droop leading edge demonstrates a reduction of the drag and pitching moments peaks during the oscillating cycle due to a weakening of the DSV in respect to the clean airfoil condition.

Moreover, the same "morphing" approach has been proposed in other works concerning the use of an impulsively actuation of leading edge slats [40] or trailing edge flaps [41]. In particular, by means of a impulsively downward slat deflection, the higher pressure airflow coming from the airfoil lower surface energizes the boundary layer on the airfoil upper surface, delaying the flow separation and the consequent formation of the vortical structure typical of the dynamic stall phenomenon.
A very interesting work is the numerical activity by Feszty et al. [41] about trailing edge flap active control on a NACA 0012 airfoil oscillating in deep dynamic stall regime. This work shows, through computational fluid dynamics, a mitigation of the large negative pitching moments and aerodynamic damping due to the upward deflection of a 16% chord trailing edge flap with actuation consisting in a brief pulse signal of sinusoidal shape with duration of about 1/3 of the airfoil motion time period.

The detailed analysis of the flowfield showed that the upward deflection of the flap produces a weakening of the DSV due to a reduction of the pressure difference between the airfoil upper and lower surface. Moreover, the downstream convecting dynamic stall vortex, responsible for the large negative pitching moments and associated negative damping, is more rapidly detached from the airfoil by means of the flap upward deflection.

Another interesting technique, used to delay the onset of dynamic stall without any modification of the airfoil shape, is the use of blowing devices integrated in the blades [43]. Such devices have been studied in an experimental work by Singh et al. [42] that evaluated the effects on the measured airloads curves of the blowing carried out by a spanwise array of air-jet vortex generators located near the leading edge; in particular, such devices are positioned at 12% chord of a RAE 9645 pitching blade section and spaced at interval of 10% chord along the span. Blowing from the front array energizes the boundary layer on the airfoil upper surface so that the separation do not occur during almost all the upstroke motion. The DSV is weakened and occurs only at the end of the upstroke motion producing the delay of C_M break and of the non-linear increase of C_L, as well as the reduction of pitching moment negative peak. The main effect of such blowing devices in terms of dynamic stall control is the reduction of the clockwise negative loops of the pitching moment coefficient characterised by negative aerodynamic damping, due to an acceleration of boundary-layer reattachment during the downstroke motion.

In the recent years the attention of the scientific community has been attracted by the study of plasma actuators for stall control purpose. In fact, many experimental activities optimized the plasma actuators set up with the aim of delaying the airfoil flow separation at a higher angle of attack in steady condition [44, 45, 46]. Then, a first experimental work on a NACA 0015 pitching airfoil tested the effects of plasma actuators for dynamic stall alleviation [47].

The plasma actuators consists in two copper electrodes separated by a dielectric insulator and laminated asymmetrically on the airfoil upper surface near the leading-edge region.

The actuators are supplied by an a.c. voltage in the order of 10 kV, so that the surrounding air ionizes and plasma forms in the regions of high electrical field potential; the ionized air, in presence of an electrical field gradient, results in a body force and produces a velocity component in the mean free-stream direction over the airfoil upper surface.
The effects of a steady and unsteady actuation of the plasma control devices are different. For the steady actuation, the a.c. voltage signal that supplies the electrodes has a frequency well above the fluid response frequency, so that the fluid senses a constant body force over the pitching cycle. The induced flow in the free-stream direction energizes the boundary layer delaying the

flow separation.

The effect of such devices with steady actuation is the increase of the lift over most of the cycle, except at the peak angle of attack. Moreover, the principle advantage of steady actuation is the suppression of a sharp drop of the lift coefficient at the beginning of the downstroke motion.

For the unsteady actuation, the a.c. voltage signal that supplies the electrodes is impulsively switched on and off with an unsteady period. The experimental activity verified that, for flow control purposes, is sufficient a percentage of time within the period when the a.c. voltage is on (duty cycle) of only 10%; then, the required power for the actuator is 90% less than for steady actuation.
The unsteady actuation introduces unsteady disturbances near the region of incipient flow separation that cause the generation of large coherent vortical structures capable to delay the onset of separation and to anticipate the reattachment during downstroke motion. The optimal actuators unsteady forcing frequency, evaluated by static tests, is obtained when the Strouhal number is near unity. Moreover, the optimal forcing frequency is based on the generation of 2 or 3 vortical structures over the separated length (considered as the airfoil chord) at any given instant of time.

The effects of the unsteady actuation of plasma devices produced on the airloads a reduction of the negative pitching moment coefficient peak and the delay of the pitching moment coefficient stall. Moreover, the unsteady actuation produces a consistent reduction of the pitching moment clockwise loop characterised by a negative aerodynamic damping, an increase of the counterclockwise loop characterised by positive aerodynamic damping and also an increase of lift at low angles of attack.

4.2 Passive control

As can be noticed from the overview of the active control systems presented in the previous section, in all the described cases, the tested active devices required the availability of non-negligible power in the rotating system through a slip ring and to design a sophisticated control system to command the actuation. Moreover, for instance, the integration in the rotor blades of a mechanism necessary for the actuation of movable surfaces, as slats or flaps, could complicate consistently the blade architecture and introduce a high

increase of the blade weight. For these reasons, the use of passive devices for stall alleviation is very appealing because they do not require power for the actuation and their complexity, in terms of airworthiness and operating cost, can be much lower compared to active systems.
The study of passive devices has been developed in the recent years for both steady and unsteady stall control purposes. For instance, a recent experimental work presents the benefits obtained in dynamic stall condition by a typical helicopter airfoil oscillating in pitch with the leading edge shape modified by the use of a "glove" surface with passive vortex generators [48].

Another interesting work concerning the use of this kind of devices has been presented just in the last months and concerns the investigation of dynamic stall control by means of fixed vortex generators positioned in the trailing edge region of a OA209 pitching blade section; in particular, in this work, numerical URANS simulations are compared to the experimental results obtained with Time-Resolved PIV [67].
As mentioned earlier, the attention of the present experimental work is focused on the study of self-activating trailing edge flaps integrated on the model blade section. The main objective of this activity consists in evaluating the possible benefits obtained by these devices for rotorcraft dynamic stall alleviation.
Moreover, another interesting goal to be assessed by this preliminary experimental activity is to suggest the way to design and tune a mechanical device to drive the actuation of such devices.

4.2.1 Pop-up flaps

The concept of a passive spoiler or "pop-up" flap was originally inspired by the observation of birds behavior when flying at high angles of attack.

During the landing approach or in gusty winds the birds feathers on the upper surface of the wings tend to pop up delaying the flow separation and enabling the flight at lower flight speed, as the lift is increased [49, 50].
Until now, this concept has been essentially investigated in static conditions and tested on fixed-wing aircraft [50, 51, 52]. The "pop up" flap in steady condition acts at high angles of attack, when flow separation starts producing a reverse flow at the trailing edge (see Fig. 4.1).

When flow separation at the trailing edge region occurs, the flap lifts and self-adjusts to an equilibrium position depending on the aerodynamic forces and flap weight. The "pop up" flap produces a partial flow reattachment

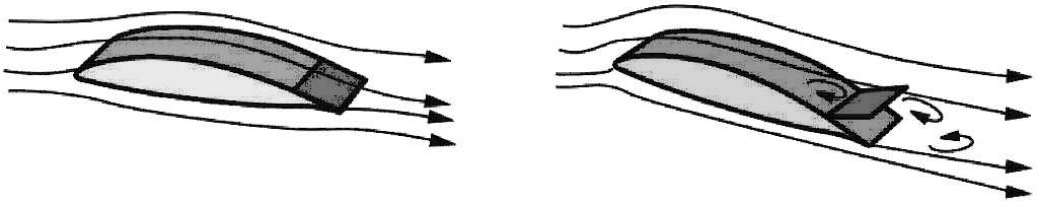

(a) Low angle of attack: flap closed (b) High angle of attack (post-stall): flap closed

Figure 4.1: "Pop-up" flap mechanism in steady condition: the self-adjusting flap is closed at low angle of attack and pops up automatically at higher angles; adapted from Meyer et al. [50].

delaying the stall, while, at low incidence, the flap remains attached to the airfoil surface and does not have any effect on the aerodynamics.
The work by Meyer et al. [50] illustrates the results of a complete numerical-experimental investigation on the use of self-activated "pop up" flaps carried out on a wing section in steady conditions.

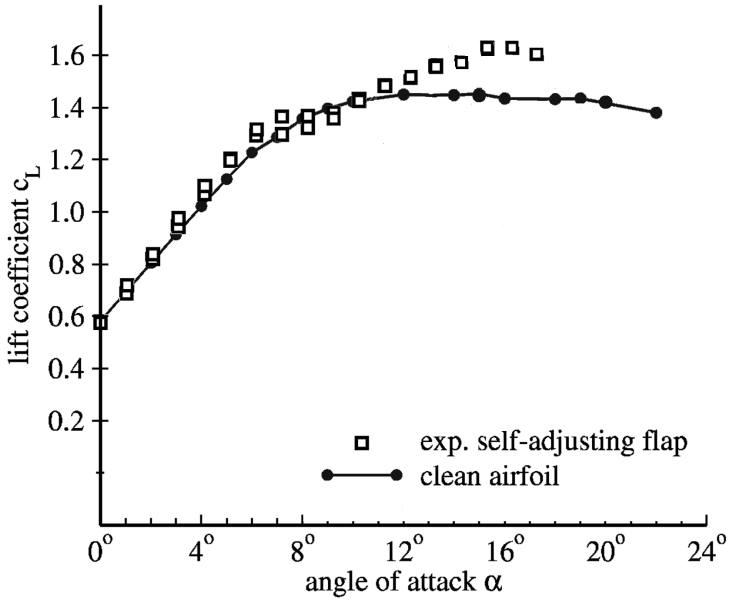

Figure 4.2: Effect of self-activated "pop up" flap on lift coefficient for a HQ17 airfoil at $Re = 1 \cdot 10^6$; adapted from Meyer et al. [50].

In particular, Fig. 4.2 represents the benefit in terms of measured lift enhancement gained by the use of a self-activated flap manufactured from an aluminum sheet and mounted on a HQ17 airfoil at 80% chord via a free-moving hinge.

4.3 Experimental activity on "pop up" flaps

The preliminary experimental investigation on self-activated "pop up" flaps involved measurements on the pitching NACA 23012 and NACA 23015 blade section models with a simple flap design. Two spoiler configurations have been tested; the first configuration consists in a aluminium sheet of 0.6 mm thickness with a chordwise length equal to 8% of the airfoil chord, hinged with adhesive tape on the upper surface at 91% of the chord from the leading edge (see Fig. 4.3). The spoiler position in chord has been suggested by the steady state experiments described by Meyer et al. [50], as the trailing edge of the movable flap should be located upstream ($\geq$ 1% chord) of the airfoil trailing edge in order to respond properly to flow separation.

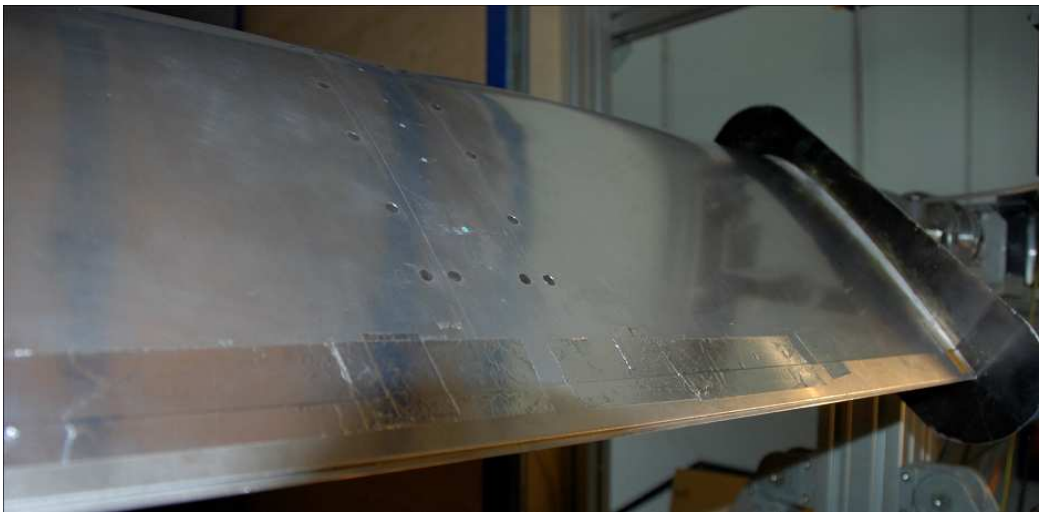

Figure 4.3: Self-activated spoiler on the NACA 23012 blade section model.

The second configuration consists in a "L" shaped spoiler in carbon fiber with a chordwise length of 25 mm and the end prong with 5 mm length.

The "L" shaped spoiler has been hinged on the airfoil surface so that the end prong acts as a Gurney flap at the airfoil trailing edge (see Fig. 4.4).

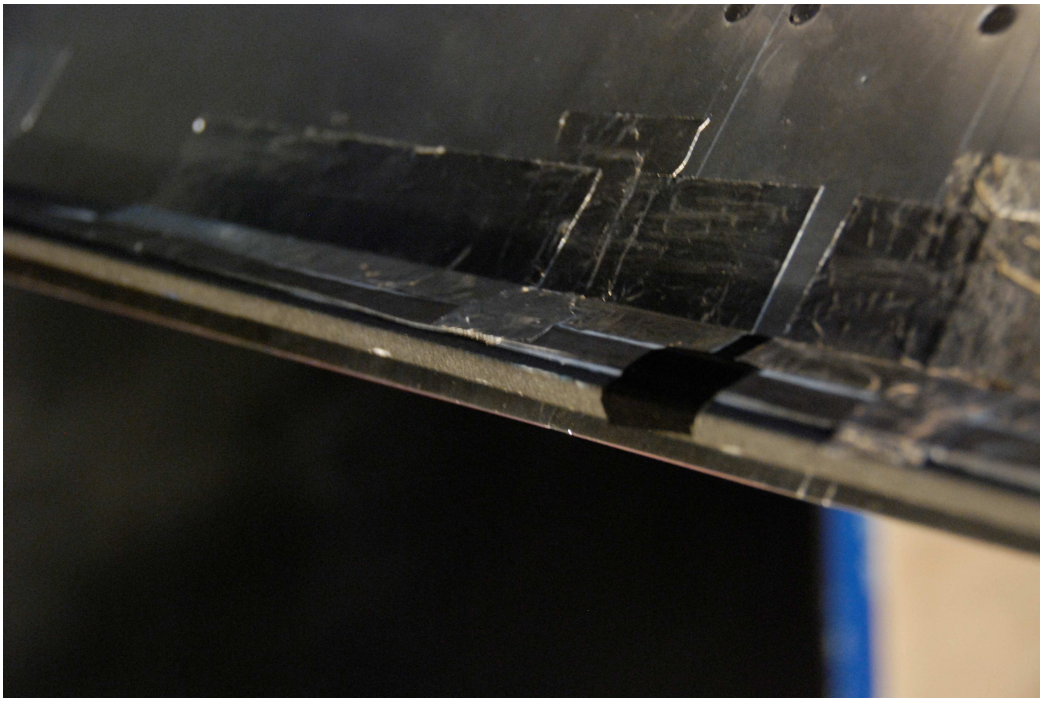

Figure 4.4: Particular "L" shaped spoiler on the NACA 23012 blade section model.

For this activity, two pitching cycle conditions have been tested, characterised by a mean angle of attack of 10° or 15°, 10° amplitude and reduced frequency $k = 0.1$ at $Re = 6 \cdot 10^5$.
Figure 4.5) presents the comparison between the airloads measured for the clean airfoil and with the two configurations of self-activated spoiler (respectively "Spoiler" and "Spoiler Gurney" in the legend).

As can be observed from the test results, the self-activated spoilers for the NACA 23012 airfoil have small influence on the measured airloads coefficients for both the configurations and pitching cycles tested. In particular, the baseline spoiler configuration does not contribute with significant effects to the airloads curves behavior that remains closely similar to the clean airfoil configuration curves. The self-activated "Gurney spoiler" produces an

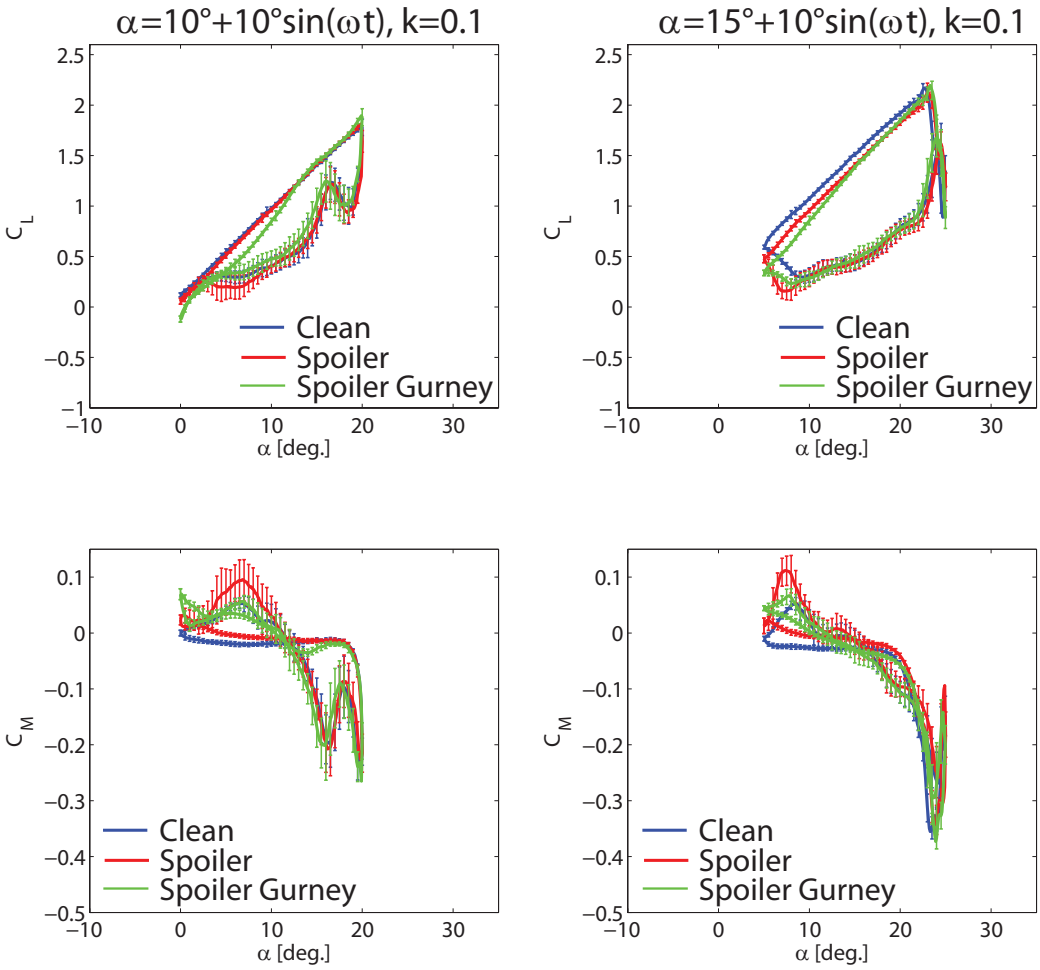

Figure 4.5: Comparison of airloads curves measured for the NACA 23012 blade section model equipped with trailing edge spoilers at $Re = 6 \cdot 10^5$.

increase of the lift coefficient curve slope during the upstroke motion but any appreciable effects in terms of reduction of pitching moment coefficient peaks and work done by the pitching moment over an oscillating cycle with negative aerodynamic damping (clockwise loop).
The motivation of such low effects could be explained by the very small angle reached by the two spoiler configurations during the tested pitching cycle conditions. In fact, before the airloads measurements, a few tests have been carried out using the PIV image acquisition system to determine the ampli-

tude and the phase of the motion of the spoiler with the Gurney flap. In particular, the motion of this spoiler has been tuned with the $1/rev$ of the airfoil motion adding a mass at the spoiler trailing edge. The images taken with the PIV camera reveals that the spoiler is opened with a maximum angle of 18° near the mean angle of attack of the oscillating cycle in upstroke ($\alpha = 10°$), while during the downstroke the spoiler does not succeed to close and reaches an equilibrium position of about 10°.
Moreover, the lack of pressure transducers positioned at the trailing edge region, in particular in the last 30 mm of the airfoil chord, could produce the loss of interesting information about the effects of the self-activated spoiler on pressure distribution.
Another reason to explain the very small influence of the trailing edge self-activated spoilers on the NACA 23012 stall could be the fact that this airfoil is characterised by a leading edge stall process. Consequently, the same spoiler configurations have been tested in the same pitching cycle conditions on the thicker NACA 23015 blade section model characterised by a trailing edge stall process.

As can be observed from the results in Fig. 4.6), the self-activated spoilers for the test condition characterised by 10° mean angle of attack produce similar effects to those noticed for the NACA 23012 airfoil. In particular, the "Gurney spoiler" modifies the linearity of the lift coefficient curve increase during the upstroke motion.
On the contrary, for the test condition characterised by 15° mean angle of attack, both the spoiler tested produce an appreciable effect consisting in a delay of the stall to a higher angle of attack during the upstroke motion, as evaluated in the work by Meyer et al. [50] for an airfoil in steady conditions. As observed for the NACA 23012 airfoil, also the tests results for the NACA 23015 airfoil do not present any remarkable effect about the reduction of pitching moment coefficient peak and hysteresis with negative aerodynamic damping.

4.4 Experimental activity on Gurney flap effects

In order to evaluate the effects of a Gurney flap on blade performance in dynamic stall conditions, the "Gurney" spoiler has been attached on the NACA

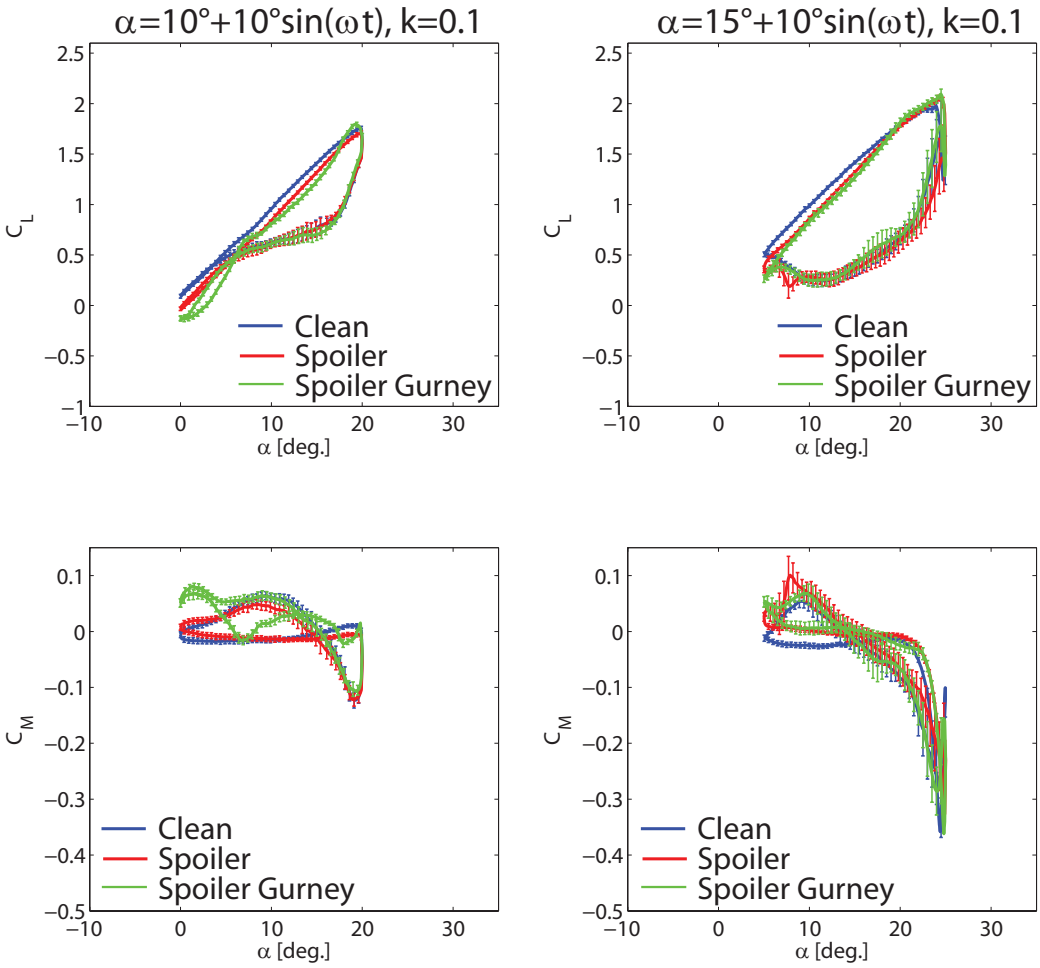

Figure 4.6: Comparison of airloads curves measured for the NACA 23015 blade section model equipped with trailing edge spoilers at $Re = 6 \cdot 10^5$.

23012 model both on the upper (Gurney flap pointing downward) and the lower airfoil surface (Gurney flap pointing upward at the trailing edge) by means of adhesive tape. In this configuration, the Gurney flap protrudes from the airfoil trailing edge with 4 mm height.
Figure 4.7) presents the comparison between the airloads measured for the clean airfoil and with the Gurney flap pointing downward ("Gurney" in the legend) and upward ("Gurney up" in the legend), for a pitching cycle condition characterised by a mean angle of attack of 10°, 10° amplitude and

reduced frequency $k = 0.1$ at two different Reynolds numbers, $Re = 6 \cdot 10^5$ and $Re = 1 \cdot 10^6$. The motivation to test the downward and upward configuration is the evaluation of a possible path for an active protrusion of the Gurney flap that could produce potential benefits for dynamic stall alleviation.

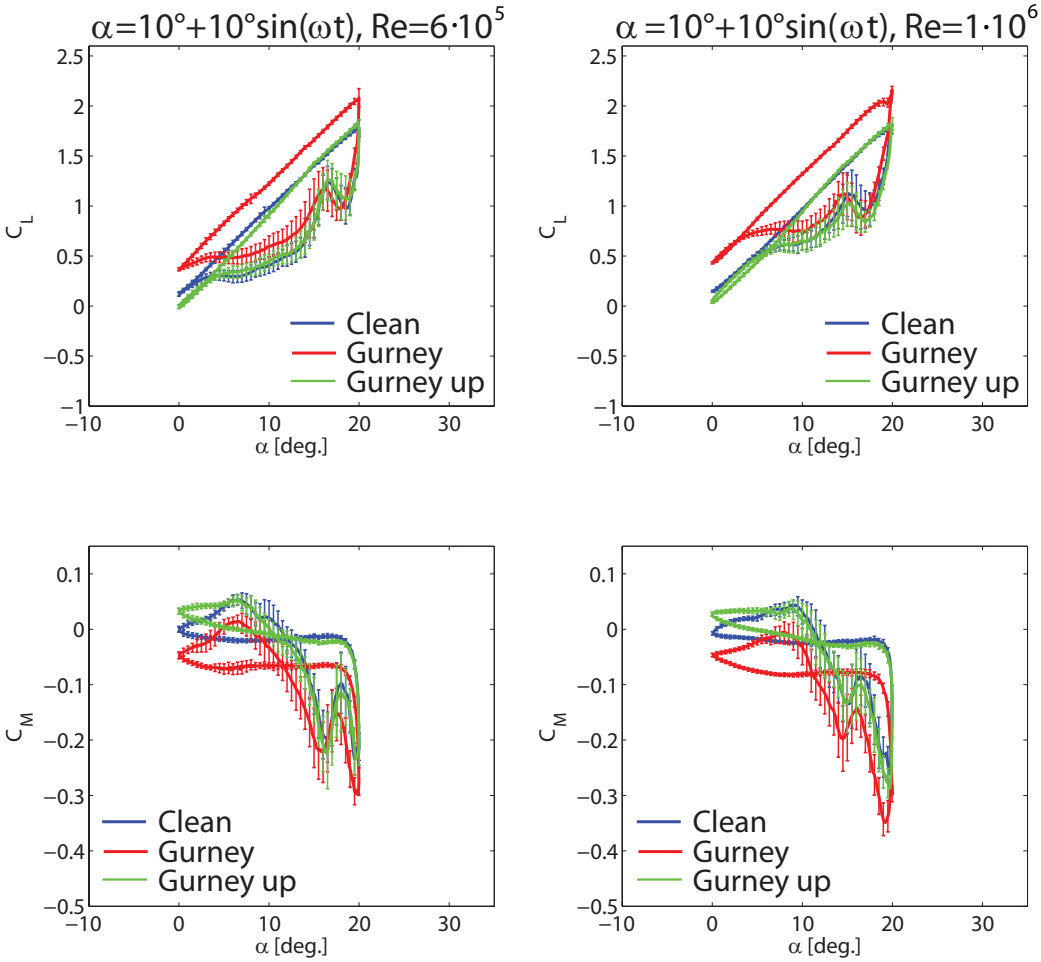

Figure 4.7: Comparison of airloads curves measured for NACA 23012 equipped with fixed Gurney flap at the trailing edge at $Re = 6 \cdot 10^5$ and $Re = 1 \cdot 10^6$.

As can be observed from the test results, the Gurney flap pointing down-

ward introduces a remarkable effect consisting in a shift of the lift and pitching moment curves respect to the clean airfoil condition, while the flap pointing upward does not produce any remarkable effects during the whole pitching cycle except from a small increase of the lift coefficient curve slope. In particular, the increase of the lift coefficient occurs during all the upstroke motion (about 15% lift enhancement near the maximum C_L) analogously to what happens in steady applications and in agreement with the results of Chandrasekhara et al. for a pitching VR-12 airfoil [69]. This can be considered an appreciable effect for the retreating blade performance, due to the associated higher level of available thrust. The increase in lift is due to an increase of camber effect resulting from the flap that directs the airfoil lower surface streamlines away from the trailing edge. Additional benefits in terms of lift increase result as the shear layers from the airfoil upper and lower surfaces meet in the wake beyond the physical trailing edge, where persists a pressure difference; this effect can be assumed equivalent to a longer airfoil chord.
The modified pressure distribution due to the Gurney flap presence is clearly visible from Fig. 4.8)(a) and (b) that presents the pressure distributions over the airfoil upper surface during the upstroke motion for the dynamic condition tested at $Re = 6 \cdot 10^5$.

The peak pressures over the airfoil upper surface are higher and spread over a larger angles of attack range ($\Delta\alpha$ in Fig. 4.8)(a) and (b)) for the configuration with Gurney flap, leading to the production of a consistent higher lift level, even at the higher angles of attack in upstroke.
In order to evaluate the benefits of the Gurney flap on blade performance, the analysis of the L/D ratio has been carried out for the clean and flapped configuration at $Re = 6 \cdot 10^5$ in upstroke motion (see 4.9). This analysis has been performed using the only form drag contribution evaluated by the integration of the surface pressure measurements.

The results in Fig. 4.9 demonstrates an increase of the efficiency at low angles of attack in upstroke, as the form drag increase produced in this angles of attack range by the Gurney flap is quite lower respect to the corresponding lift increase, while at higher angles of attack the stronger increase of drag produces a decrease of the efficiency respect to the clean configuration level. The efficiency analysis would require further investigation about the viscous contribution of the drag as well as a direct measurement of the pressure on the front and back surfaces of the flap.

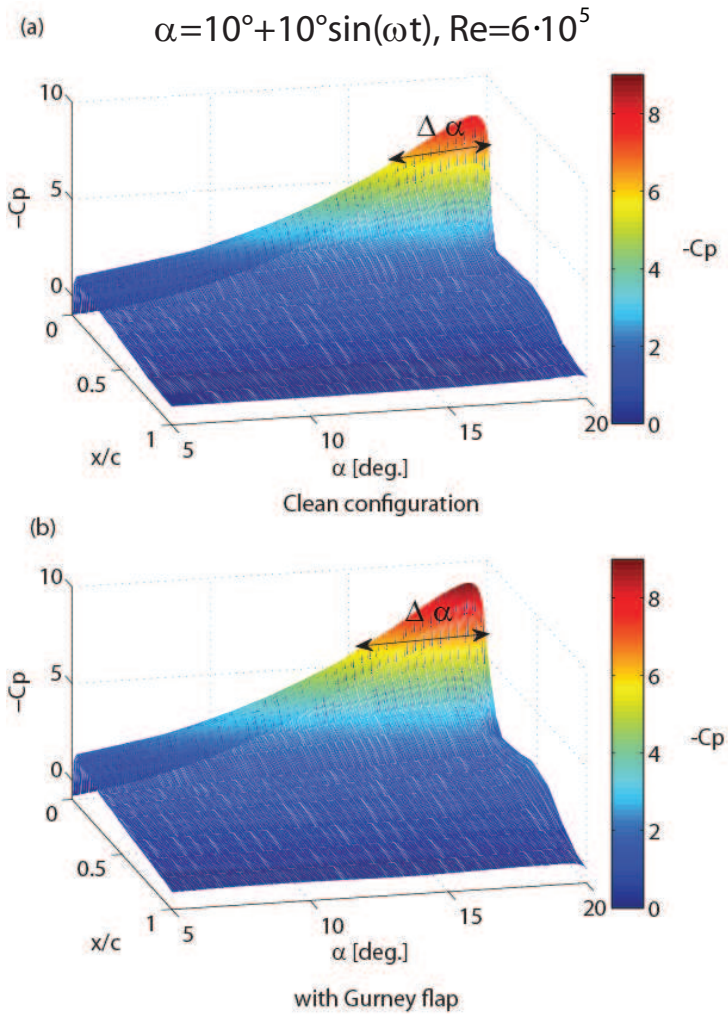

Figure 4.8: L/D distribution for NACA 23012 equipped with fixed Gurney flap at $Re = 6 \cdot 10^5$.

The observation of the moment coefficient curves in Fig. 4.7) confirms that advantages can be obtained by the use of an active Gurney flap, as proposed by several authors (see for example [70, 71]). In particular, the fact that the Gurney flap produces a negative offset either in upstroke and downstroke suggests that retreating the Gurney flap in downstroke could increase the counterclockwise loop area (positive aerodynamic damping) and reduce

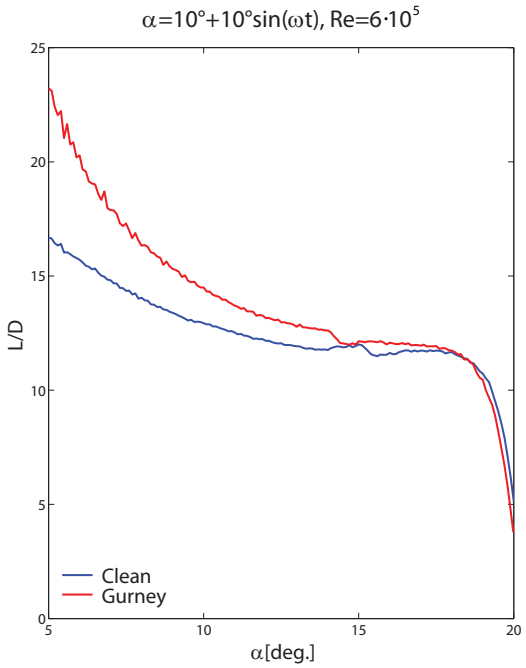

Figure 4.9: L/D distribution for NACA 23012 equipped with fixed Gurney flap at $Re = 6 \cdot 10^5$.

the clockwise loop area (negative dumping) reducing the risks of stall flutter occurrence. These experimental results encourages the research activity to get a more complete investigation on the use of an active Gurney flap.

Chapter 5

Conclusions and Future developments

The activity described in this work contributed successfully to the research in rotorcraft field about the dynamic stall phenomenon, suggesting different reliable tools, both experimental and numerical, to get a better comprehension of the rotor retreating blade aerodynamics.The new experimental rig designed for testing blade section models oscillating in pitch demonstrated great reliability and allowed to achieve a complete and a better insight of the dynamic stall phenomenon on helicopter rotor retreating blade, by means of the results analysis of a comprehensive wind tunnel tests campaign carried out on a NACA 23012 blade section model. In particular, the main success of the new experimental rig design has been the capability of reproducing the typical conditions of the flight envelope of a full-scale helicopter retreating rotor blade section at high forward flight speed. Moreover, the use of different experimental techniques, as high-response pressure measurements and PIV, enabled to describe the details of the typical aerodynamic features involved in the phenomenon and to evaluate the performance of the NACA 23012 airfoil under severe unsteadiness conditions.
The measure of both the amount of hysteresis and the peak values of the airloads during a pitching cycle for the different dynamic stall regimes described in literature represents one of the most important aspects to be assessed in the phase of development and sizing of new control devices for the mitigation of the dynamic stall.
The PIV flow field surveys, performed with a high spatial resolution, showed the detailed flow physics that characterise the different stages of the blade

stall process. The PIV technique has been involved in particular to get a complete overview of the deep dynamic stall regime that represents the most severe condition for the retreating blade in terms of detrimental effects for rotorcraft performance.
The comprehensive data set produced by the experimental activity on the NACA 23012 airfoil could be considered as a reference data base for the validation of numerical models. In fact, the present work showed the comparison of the experimental results for deep dynamic stall conditions with the numerical results obtained from simulations with two-dimensional numerical models built using the compressible Navier-Stokes solver EDGE developed at FOI. Numerical simulations have been found to be in good agreement with the experimental ones. The first results presented in this work showed a preliminary assessment of the dynamic stall phenomenon modeling capabilities as, currently, the focus of the research activity in this field is the test of more advanced numerical techniques, such as the Detached Eddy Simulation or the Large Eddy Simulation, to verify the capabilities of a more accurate numerical model. Moreover, another focus point of this activity will be the study of the possible three-dimensional effects on the dynamic stall process by means of the comparison of the experimental results with the results of numerical simulations carried out on three-dimensional models reproducing exactly the experiments in the wind tunnel.
After the characterisation of the airfoil performance obtained by the wind tunnel test campaign on the clean model, the experimental rig has been employed to test the effectiveness of passive control devices for dynamic stall phenomenon mitigation. The measurements of the airloads on the NACA 23012 blade section equipped with self-activated movable flaps at the airfoil trailing edge region do not present appreciable variations of the airfoil performance during a pitching cycle. The motivation of the very low effects on the airloads produced by such devices could be explained by the small deflections reached during the oscillating cycle and by the fact that the employed NACA 23012 airfoil presents a leading edge stall process that is very scarcely influenced by the deflection of a trailing edge spoiler. Consequently, a blade section model with NACA 23015 airfoil has been manufactured and tested for evaluating the performance of the self-activated flaps on a thicker airfoil characterised by a trailing edge stall process. The results of the tests on the NACA 23015 airfoil shows, as an appreciable effect in term of control, a delay of the stall at a higher angle of attack.
The tests campaign carried out on the NACA 23012 airfoil equipped with a

fixed Gurney flap at the trailing edge demonstrated another appreciable effect on the airfoil performance. In fact, the large increase of the measured lift coefficient during all the upstroke motion and the increase of efficiency evaluated from the pressure measurements illustrate the potential benefits that a Gurney flap pointing downward could introduce for dynamic stall control. One of the main goal of this activity could be considered the analysis of the capabilities of such devices in the different phases of the pitching cycle to be taken in account in the design of an active control law for a Gurney flap at the blade airfoil trailing edge; in particular, looking at the measured pitching moment curves with and without the Gurney flap, the results suggest that the way to get an appreciable contribution for dynamic stall alleviation is the downward protrusion during the upstroke motion of the blade pitching cycle and the retraction during the downstroke. This way of active control would introduce the augment of lift (with higher available thrust) and the reduction of risks of stall flitter occurrence due to an increase of the net aerodynamic damping. The results gained from the experiments with the fixed Gurney flap encourage the research activity to get a more complete investigation on the use of an active Gurney flap for dynamic stall control purposes. In fact, one of the more ambitious goal of the future activity could be the design and manufacture of a new blade section model with an interchangeable trailing edge equipped with an active Gurney flap or spoiler that could be deployed dynamically only through the critical dynamic stall phase of the pitching cycle motion, highlighted by the tests with the passive devices.
Another challenging goal of the present research is the measurement of the total drag contribution acting on the pitching blade section in dynamic stall conditions; this research activity would be very interesting to quantify, for instance, the effects in terms of drag increase produced by the control devices, as well as to validate completely the performance of a new airfoil to be used for rotor blades. The severe unsteadiness that characterises the dynamic stall phenomenon illustrates the difficulty to get a reliable measurement of the drag component using a mechanical balance embedded into the model. Consequently, pressure and velocity surveys could be used as an alternative. In this aim, the current activity of our research group is the evaluation of the drag component acting on the pitching airfoil from the measurement of the velocity field in the wake of the model at the midspan section. The method is based on the constitutive two-dimensional flow equations using the control volume approach and the concept of phase average [64]. In particular, a preliminary wind tunnel campaign has been carried out using hot wire

X-probes to measure the velocity components in the wake of the oscillating airfoil in clean configuration. At the moment, this activity arrived at the post-processing phase of the wind tunnel tests results, that highlighted the necessity to carry out further tests to verify the pressure boundary conditions.

Bibliography

[1] W.J. McCroskey. The Phenomenon of Dynamic Stall, NASA TM 81264, 1981.

[2] L.W. Carr, K.W. McAlister and W.J. McCroskey. Anaysis of the Development of Dynamic Stall Based on Oscillating Airfoil Measurements, NASA TN D 8382, 1977.

[3] L.W. Carr, K.W. McAlister and W.J. McCroskey. Dynamic stall Experiments on the NACA 0012 Airfoil, NASA TP-1100, 1978.

[4] J.G. Leishman. Principles of helicopter aerodynamics, Cambridge Aerospace Series, 2000.

[5] L.E. Ericsson. Comments on Unsteady Airfoil Stall, *Journal of Aircraft*, **5**, pp.478-480, 1967.

[6] F.O. Carta. An Analysis of the Stall Flutter instability of Helicopter Rotor Blades, *Journal of American Helicopter Society*,**12**, pp.1-8, 1967.

[7] F.O. Carta. Effect of Unsteady Pressure Gradient Reduction on Dynamic Stall Delay, *Journal of Aircraft*, **8**(10), pp.839-840, 1971.

[8] T.S. Beddoes. A Synthesis of Unsteady Aerodynamic Effects Including Stall Hysteresis, *Vertica*, **1**, pp.113-123, 1976.

[9] R.A.McD. Galbraith, A.J. Niven and L.Y.Seto. On th Duration of Low Speed Dynamic Stall, Paper ICAS-86-2.4.3. Inernational Committee of the Aeronautical Sciences, London, England, 1986.

[10] R.B. Green and R.A.McD. Galbraith. Dynamic Recovery to Fully Attached Aerofoil Flow from Deep Stall, *AIAA Journal*, **33**, pp.1433-1440, 1995.

[11] R.W. Prouty. Helicopter Aerodynamics, Rotor and Wing International, PJS Publications Inc., 1985.

[12] N.C.G. Isaacs and R.J. Harrison. Identification of Retreating Blade Stall Mechanism Using Fligth Test Pressure Measuements, 45th Annual Forum of the American Helicopter Society, Boston, MA, May 22-24, 1989.

[13] W.G. Bousman. A Qualitative Examination of Dynamic Stall From Flight Test Data, *Journal of the American Helicopter Society*, **18**, pp.36-46, 1998.

[14] W.Z. Stepneiwski and C.H. Keys. Rotar Wings Aerodynamics, Dover Pubblications, New York, NY, pp.103-116, 1984.

[15] P.F. Lorber, A.F. Covino and F.O. Carta. Dynamic Stall experiments on a Swept Three-Dimensional Wing in Compressible Flow, AIAA Paper 91-1795, 22nd Fluid Dynamics, Plasma Dynamics and Laser Conference, Honolulu, HI, June 24-26, 1991.

[16] R.A. Pizialli. "2-D and 3-D Oscillating Wing Aerodynamics for a Range of Angles of Attack Including Stall, *Journal of Solar Energy Enginnering*, **117**, pp.200-204, 1994.

[17] E. Berton, C. Allain, D. Favier and C. Maresca. Experimenal Methods for Subsonic Flow Measurements, *Progress in Computational Flow-Structure Interaction*, W. Haase, V. Selmin and B. Winzell (eds.), Notes on Numerical Fluid Mechanics & Multidisciplinary Design, **81**, Springer, Berlin, pp.97-14, 2003.

[18] P. Wernert, G. Koerber and F. Wietrich. A New Experimental Apparatus for the Study of the Unsteady Flowfield over an Airfoil in Pitching and Heaving Motions using Laser Doppler Anemometry, European Forum on Wind Tunnels and Wint-Tunnel Test Techniques (Dover Edition ed.), Southampton, UK, Rapport ISL CO 229/92 (1992) Article 45, Sept., 1992.

[19] M. Raffel, H. Richard, P. Bosbach and W. Geissler. Pitching Airfoil Boundary Layer Investigations, 12th International Symposium on Flow Visualization, German Aerospace Center (DLR), Göttingen, Germany, Sep. 10-14, 2006.

[20] T. Theodorsen. General Theory of Aerodynamic Instability and the Mechanism of Flutter, NACA Report 496, 1935.

[21] Labview version 9.0, User Manual, National Instruments, www.ni.com.

[22] MATLAB version 2011, User Manual, The Mathworks, www.mathworks.com.

[23] PIVview 3C version 3.0, User Manual, PIVTEC, www.pivtec.com.

[24] C. Tropea et al. Handbook of Experimental Fluid Mechanics, Springer, 2007.

[25] J.G. Leishman. Dynamic stall experiments on the NACA 23012 aerofoil, *Experiments in Fluids*, **9**, pp.49-58, 1990.

[26] P. Eliasson. EDGE, a Navier-Stokes solver for unstructured grids, *Proc. to Finite Volumes for Complex Applications III*, **1**, pp.527-534, 2002.

[27] F. Menter, M. Kuntz and R. Langtry. Ten years of industrial experience with the SST turbulence model, *Turbulence, heat and mass transfer*, **4**, pp.625-632, 2003.

[28] S. Wallin. Engineering turbulence modeling for CFD with a focus on explicit algebraic Reynolds stress models, *Doctoral Thesis Norsteds Tryckeri AB*, Stockholm, Sweden, 2003.

[29] A. Hellsten. New advanced $k-\omega$ turbulence model for high-lift aerodynamics, *AIAA Journal*, **43**, pp.1857-1869, 2005.

[30] W. Geissler, G. Dietz and H. Mai. Dynamic stall on a supercritical airfoil, *Aerospace Science and technology*, **9**, pp.390-399, 2005.

[31] L.K. Loftin Jr. and H.A. Smith. Aerodynamic characteristics of 15 naca airfoil sections at seven Reynolds numbers, NACA Technical Report, Langley Aeronautical Laboratory, 1949.

[32] W.J. Mccroskey, K.W. Mcalister, L.W. Carr and S.L. Pucci. An experimental study of dynamic stall on advanced airfoil sections. Volume 1: Summary of the experiment, NASA TM 84245, 1982.

[33] W.J. Mccroskey, K.W. Mcalister, L.W. Carr and S.L. Pucci. An experimental study of dynamic stall on advanced airfoil sections. Volume 2: Pressure and Force Data, NASA TM 84245, 1982.

[34] M. Raffel, J. Kompenhans, P. Wernert. Investigation of the unsteady flow velocity field above an airfoil pitching under deep dynamic stall conditions, *Experiments in Fluids*, **19**, pp.103-111, 1995.

[35] K. Mulleners and M. Raffel. The onset of dynamic stall: a time-resolved approach, 36th European Rotorcraft Forum, 7-9 September, Paris, France, 2010.

[36] XFoil, Subsonic Airfoil Development System, User Guide, http://web.mit.edu/drela/Public/web/xfoil/.

[37] M. Raffel, J. Kompenhans, B. Stasicki, B. Bretthauer and G.E.A. Meier. Velocity measurement of compressible air flows utilizing a high-speed video camera, *Experiments in Fluids*, **18**, pp.204-206, 1995.

[38] M. Raffel, C. Willert and J. Kompenhans, Particle Image Velocimetry, a practical guide, Springer, Heidelberg, 1998.

[39] M. Chandrasekhara, P. Martin and C. Tung. Compressible Dynamic Stall Control Using a Variable Droop Leading Edge Airfoil, *Journal of Aircraft*, **41**, pp.862-869, 2004.

[40] L.W. Carr, M.S. Chandrasekhara, M.C. Wilder and K.W. Noonan. Effect of Compressibility on Suppression of Dynamic Stall Using a Slotted Airfoil, *Journal of Aircraft*, **38**, 2001.

[41] D. Feszty, E. Gillies and M. Vezza. Alleviation of Airfoil Dynamic Stall Moments via Trailing-Edge Flap Flow Control, *AIAA Journal*, **42**, pp.17-25, 2001.

[42] C. Singh, D. Peake, A. Kokkalis, V. Khodagolian, F. Coton and R. Galbraith. Control of Rotorcraft Retreating Blade Stall Using Air-Jet Vortex Generators, *Journal of Aircraft*, **43**, pp.1169-1176, 2006.

[43] D. Weaver, K.W. McAlister and J. Tso. Control of VR-7 Dynamic Stall by Strong Steady Blowing, *Journal of Aircraft*, **41**, pp. 1404-1413, 2004.

[44] M. Post and T. Corke. Separation Control on High Angle of Attack Airfoil Using Plasma Actuators, *AIAA Journal*, **42**, pp.2177-2184, 2004.

[45] T. Corke, C. He and M. Patel. Plasma Flaps and Slats: An Application of weakly-Ionized Plasma Actuators , 2nd AIAA Flow Control Conference, Portland, Oregon, June 28-July 1 , 2004.

[46] A.Vorobiev, R. Rennie, E. Jumper and T. McLaughlin. Experimental Investigation of Lift Enhancement and Roll Control Using Plasma Actuators, *Journal of Aircraft*, **45**, 2008.

[47] M. Post and T. Corke. Separation Control Using Plasma Actuators: Dynamic Stall Vortex Control on Oscillating Airfoil, *AIAA Journal*, **44**, pp.3125-3135, 2006.

[48] P.B. Martin, J.S. Wilson, J.D. Berry, T.C. Wong, M. Moulton and M. McVeigh. Passive Control of Compressible Dynamic Stall, 26th AIAA Applied Aerodynamics Conference, Honolulu, Hawaii, 18-21 August, 2008.

[49] D.W. Bechert, M. Bruse, W. Hage and R. Meyer, R. Fluid Mechanics of Biological Surfaces And Their Technological Application, *Naturwissenschaften*, Springer, New York, **87**, pp.157–171, 2000.

[50] R. Meyer, W. Hage, D.W. Bechert, M. Schatz, T. Knacke and F. Thiele. Separation control by self-activated movable flaps. *AIAA Journal*, **45**, pp.191–199, 2007.

[51] K.H. Kernstine, C.J. Moore, A. Cutler, et al. Initial characterization of self-activated movable flaps, "pop-up feathers", 46th AIAA Aerospace Sciences Meeting, Reno, Nevada, AIAA 2008-369, 2008.

[52] J.U. Schluter. Lift enhancement at low reynolds numbers using self-activated movable flaps. *Journal of Aircraft*, **47**, pp.348–351, 2010.

[53] A.R.S. Bramwell, G. Done and D. Balmford. Bramwell's Helicoper Dynamics, Second Edition, Butterworth-Heinemann, 2001.

[54] W.J. McCroskey and R.K. Fisher jnr. Detailed aerodynamic measurements on a model rotor in the blade stall regime, *Journal of American Heicopter Society*, **17**, 1972.

[55] N.D. Ham and M.S. Garelick. Detailed stall oscillations in helicopter rotors, *Journal of American Heicopter Society*, **13**, 1968.

[56] MD Nastran version 2010.1, User Manual, MSC Software, www.mscsoftware.com.

[57] J.B. Barlow, W.H. Rae and A. Pope, Low-Speed Wind Tunnel Testing, John Wiley & Sons Inc.,1999.

[58] E.C. Maskell, A theory of blockage effects on bluff bodies and stalled wings in a closed wind tunnel, ARC R & M 3400, 1965.

[59] A. Betz, A Method for the Direct Determination of Wing Section Drag, NACA TM 337, 1925.

[60] B.M. Jones, Measurement on Profile Drag by the Pitot-Traverse Method, British ARC R&M 1688, 1936.

[61] C.P. van Dam, Recent Experience with Different Methods of Drag Prediction, *Progress in Aerospace Sciences*, **35**, pp.751-798, 1999.

[62] B. Lu and M.B. Bragg, Experimental Investigation of the Wake-Survey Method for a Bluff Body With a Highly Turbulent Wake, AIAA 20th Applied Aerodynamics Conference, St.Louis, Missouri, 24-26 June, 2002.

[63] B.W. van Oudhensen, F. Scarano, E.W.M. Roosenboom, E.W.F. Casimiri and L.J. Souverein, Evaluation of integral forces and pressure fields from planar velocimetry data for incompressible and compressible flows, *Experiments in Fluids*, **43**, pp.153-162, 2007.

[64] E. Berton, C. Maresca and D. Favier, A new experimental method for determining local airloads on rotor blades in forward flight, *Experiments in Fluids*, **37**, pp.455-457, 2004.

[65] J.D. Anderson jr., Fundamentals of aerodynamics, 2nd edn., McGraw Hill, New York, 1991.

[66] P. Wernert and D. Favier, Considerations about the phase averaging method with application to ELDV and PIV measurements over pitching airfoils, *Experiments in Fluids*, **27**, pp.473-483, 1999.

[67] G. Joubert et al., Investigation of Dynamic Stall Control by Deployable Vortex Generator using URANS Computations and Time-Resolved PIV Analysis, 37th European Rotorcraft Forum, 13-15 September, Gallarate (VA), Italy, 2011.

[68] A.D. Gardner, K. Richter, H. Mai, A.R.M. Altmikus, A. Klein and C.H. Rohardt, Experimental Investigation of Dynamic Stall Performance for the EDI-M109 and EDI-M112 Airfoils, 37th European Rotorcraft Forum, 13-15 September, Gallarate (VA), Italy, 2011.

[69] M. Chandrasekhara, P. Martin and C. Tung., Compressible Dynamic Stall Performance of a Variable Droop Leading Edge Airfoil with a Gurney Flap, *Journal of American Helicopter Society*, **53**, pp.18-25, 2008.

[70] B. Min, L.N. Sankar, N. Rajmohan and J.V.R. Prasad, Computational Investigation of Gurney Flap Effects on Rotors in Forward Flight, *Journal of Aircraft*, **46**, pp.1957-1964, 2009.

[71] H. Yeo, Assessment of Active Controls for Rotor Performance Enhancement, *Journal of the American Helicopter Society*, **53**, pp.152–163, 2008.